On disorder effects in topological insulators and semimetals

Im Fachbereich Physik
der Freien Universität Berlin
eingereichte

Dissertation

zur Erlangung des Grades eines Doktors der Naturwissenschaften

von

Björn Sbierski

Berlin, im März 2016

Gutachter

Prof. Dr. Piet Brouwer (Freie Universität Berlin)

Prof. Dr. Matthias Vojta (Technische Universität Dresden)

Datum der Disputation: 11. Mai 2016

Selbstständigkeitserklärung

Hiermit versichere ich, dass ich in meiner Dissertation alle Hilfsmittel und Hilfen angegeben habe, und auf dieser Grundlage die Arbeit selbstständig verfasst habe. Diese Arbeit habe ich nicht schon einmal in einem früheren Promotionsverfahren eingereicht.

Berlin, 17. März 2016

Meinen Eltern gewidmet, die mich zur Neugier ermutigt haben.

Contents

List of publications

This cumulative dissertation is based on the following first-author publications with the author's contribution indicated.

- [1] B. Sbierski and P.W. Brouwer: *Z2 phase diagram of three-dimensional disordered topological insulators via a scattering matrix approach*, Phys. Rev. B **89**, 155311 (2014) [ArXiv1401.7461]

  The author is the main contributor of this publication, in particular he conceptualized the study, performed the numerical and analytical calculations and had a pivotal role in the writing of the text.

- [2] B. Sbierski, M. Schneider and P.W. Brouwer: *The weak side of strong topological insulators*, Phys. Rev. B **93**, 161105(R) (2016) [ArXiv1602.03443]

  The author is the main contributor of this publication, in particular he performed all numerical calculations, interpreted the data and was responsible for preparing the manuscript.

- [3] B. Sbierski, G. Pohl, E. J. Bergholtz, P. W. Brouwer: *Quantum transport of disordered Weyl semimetals at the nodal point*, Phys. Rev. Lett. **113**, 026602 (2014) [ArXiv:1402.6653]

  The author is the main contributor of this publication, he provided important input to the design of the study, was responsible for the implementation of the numerical method, contributed to the interpretation of the data, performed the analytical calculations in the appendix and had a leading role in the writing of the manuscript.

- [4] B. Sbierski, E. J. Bergholtz, P. W. Brouwer, *Quantum critical exponents for a disordered three-dimensional Weyl node*, Phys. Rev. B **92**, 115145 (2015) [ArXiv:1505.07374]

  The author was the main contributor of this publication, he identified the main question, devised the scaling scheme, performed the numerical calculations, was responsible for the data analysis and manuscript preparation.

Publications, that have been completed in parallel to this thesis:

- [5] M. Trescher, B. Sbierski, P. W. Brouwer, E. J. Bergholtz, *Quantum transport in Dirac materials: Signatures of tilted and anisotropic Dirac and Weyl cones*, Phys. Rev. B **91**, 115135 (2015) [ArXiv:1501.04034]

Abstract

Topological materials are in the focus of contemporary condensed matter physics, both in experiment and theory. They are of interest in fundamental research and for prospective technological applications which range from novel electronic devices to platforms for quantum computation. While the material class of time-reversal invariant topological insulators is by now an established research topic, topological gapless materials like Weyl semimetals have attracted interest only recently. In this thesis we theoretically study certain aspects of disorder physics in both material classes. By employing the framework of scattering theory in exact numerical calculations, we are able to circumvent numerous problems of other frequently used approaches and provide a complementary viewpoint.

In particular, we focused on quantum phase transitions of host materials in disordered environments. In the case of three dimensional topological insulators we were able to solidify the generic phase diagram in the presence of disorder by directly calculating the topological invariants for large tight-binding models. We interpret our results in terms of a disorder scattering induced renormalization of clean model parameters. In this way, topological phase transitions established in the clean case can also be driven by disorder..

A different type of imperfection in crystal lattices are dislocation lines. They appear, for example if a lattice plane of atoms is suddenly terminated within the crystal. The resulting one dimensional lattice defect that terminates only at other defects or surfaces is ubiquitous in real materials. In topological insulators, however, under certain conditions such dislocation lines harbor topological zero modes that electronically connect topological surface states on opposing surfaces. We study the consequences for the overall electronic structure of these materials.

Weyl nodes are elementary building blocks of Weyl semimetal bandstructures that have been confirmed first in the $TaAs$ material class. In this type of topological bandstructures, disorder scattering causes a novel type of phase transition between a semimetal and a diffusive phase. This phase transition has no counterpart in clean systems, unlike in the case of disordered topological insulators. We establish its properties in the framework of mesoscopic quantum transport and find robust signatures in conductance and shot noise. Moreover, we contributed to the ongoing efforts to characterize the universality class of this transition. Namely, a distinguished scaling approach based on our scattering matrix results allowed for the determination of the critical exponents with unprecedented precision.

Zusammenfassung

Topologische Materialien stehen im Fokus der aktuellen Forschung zur Physik der kondensierten Materie, im Experiment wie auch in der Theorie. Dies gilt sowohl für grundlegende Fragen des Feldes als auch für Anwendungen in neuartigen elektronischen Bauteilen oder im Bezug auf Plattformen für zukünftige Quantencomputer. Während die Materialklasse der topologischen Isolatoren mit Zeitumkehrinvarianz ein etabliertes Forschungsfeld ist, haben neuartige topologische Materialien ohne Bandlücke erst kürzlich ein gesteigertes Interesse auf sich gezogen. In dieser Arbeit beschreiben wir bestimmte Aspekte von Unordnungsphysik in beiden Materialklassen. Durch Anwendung der Streutheorie in exakten numerischen Berechnungen können wir einige Probleme anderer etablierter Methoden umgehen und komplementäre Einsichten erzielen.

Ein Schwerpunkt dieser Arbeit besteht in dem Studium von Quantenphasenübergängen in ungeordneten topologischen Materialien. Für den Fall der dreidimensionalen topologischen Isolatoren konnte das generische Phasendiagramm mit einer neuen, auf der Streumatrix basierenden Methode, berechnet werden. Auf Grundlage großer tight-binding Modelle konnten frühere Resultate teilweise gestützt und andere, umstrittene Vorschläge verworfen werden. Die Ergebnisse konnten analytisch als unordnungsinduzierte Renormierung der sauberen Modellparameter verstanden werden.

Eine besondere Art von Unordnung in Kristallgittern sind Versetzungslinien. Diese entstehen zum Beispiel, wenn Gitterebenen im Kristall plötzlich terminieren. Das Resultat ist ein eindimensionaler Gitterdefekt, der bis zur Kristalloberfläche oder anderen Gitterdefekten propagiert und häufig in realen Materialien vorkommt. Die besondere Eigenschaft solcher Defekte in topologischen Isolatoren ist jedoch das mögliche Auftreten von topologisch beschützten elektronischen Zuständen, die entlang von Versetzungslinien propagieren. Diese Zustände können die topologischen Zustände auf den Kristalloberflächen durch das Kristallvolumen hindurch miteinander verbinden. Wir beschreiben die daraus resultierenden Konsequenzen für die elektronische Struktur dieser Materialien.

Weyl-Knoten sind elementare Bausteine in der Bandstruktur von Weyl-Semimetallen, die kürzlich experimentell in der TaAs Materialklasse bestätigt wurden. In dieser Art topologischer Bandstrukturen erzwingt die Streuung an einem Unordnungspotential einen neuartigen Phasenübergang zwischen einer semimetallischen und einer diffusiven Phase. Im Gegensatz zu den ungeordneten topologischen Isolatoren korrespondiert dieser Phasenübergang mit keinem bekannten Phasenübergang in sauberen Materialien. Wir etablieren die Eigenschaften dieses neuartigen Phasenübergangs im Rahmen der mesoskopischen Quantentransporttheorie, indem wir zeigen, wie sich die verschiedenen Phasen in Leitwert und Schrotrauschen manifestieren. Des Weiteren liefern wir einen Beitrag zur Bestimmung der Universalitätsklasse des Phasenübergangs, insbesondere konnten die kritischen Exponenten durch Anwendung eines spezialisierten Skalierungsansatzes auf Basis von Transporteigenschaften mit beispielloser Präzision bestimmt werden.

1 Introduction

1.1 Topological insulators and semimetals

The discovery of the quantum Hall effect in 1980 by von Klitzing and co-workers [6] marked the beginning of a new era in condensed matter physics. The groundbreaking observation was that a two-dimensional electron gas subject to a strong magnetic field in perpendicular direction has a precisely quantized Hall conductivity $\sigma_{xy} = ne^2/h$ where n is an integer. From the physical constants in this value, the quantum nature of the phenomenon was obvious, but its robustness to, say, sample imperfections could only be understood after the seminal work by Thouless, Kohmoto, Nightingale and den Nijs [7] who linked σ_{xy} to the first Chern number, a topological quantity of the electron wavefunctions in the quantum Hall state. Halperin showed that the quantum Hall state is accompanied with chiral edge modes at the sample boundaries [8]. Those can be understood in terms of skipping orbits of quasi-classical electrons moving in a magnetic field as they bounce off the sample edges. Although the quantum Hall effect and its intricately correlated fractionalized version [9] remained an active research topic for several decades, its necessity of a strong external magnetic field to break time-reversal symmetry placed this quantum state apart as a peculiarity: Most other materials are either time-reversal symmetric or three dimensional, in both situations the Chern number vanishes exactly. The requirement of a net magnetic flux for the quantum Hall state could however be overcome at least in theory by Haldane [10]. In 1988 he showed how a non-zero Chern number can arise even without Landau levels.

Only in 2005, Kane and Mele realized that the presence of time-reversal symmetry does not necessarily preclude the possibility of topological states of matter [11, 12]. They studied graphene in the presence of a spin-orbit coupling term and found a Kramers pair of eigenstates crossing the bulk band gap, see Figure 1.1. Like Halperin's chiral edge state in the quantum Hall effect, these states are localized at the edge and are robust to perturbations of the Hamiltonian that do not close the bulk gap and respect time-reversal symmetry. These edge states are incarnations of the 'bulk-boundary correspondence' already discovered in the quantum Hall state: The topological invariant cannot change unless the bulk gap in the quasiparticle spectrum is closed, so a topological material cannot neighbor a non-topological

one without the presence of gapless states at the interface. Kane and Mele also identified the nature of the topological invariant ν for their novel time-reversal invariant topological insulator, in contrast to the Chern number it can only take two different values $\nu = 0, 1$ and is thus called a Z_2 invariant. The formulation of the invariant in terms of the bulk wavefunctions will be detailed below. In terms of edge states, the topological distinction and stability is evident from Figure 1.1 where ν counts the parity of the number of Fermi level crossings of an edge state as k_x traverses from 0 to π/a (the remainder of the edge Brillouin zone is related by time-reversal symmetry). Since the degeneracy of the edge states at $k_x = \pi/a$ is protected by Kramers degeneracy (a direct consequence of time-reversal invariance for spinful electrons) an edge state corresponding to a topologically nontrivial bulk with $\nu = 1$ can never be completely pushed out of the gap.

A definition for ν inspired from charge pumping concepts in the framework of quantum Hall physics is proposed in reference [13]. Using the antiunitary time-reversal operator $T = -i\sigma_y K$ with σ_y the second Pauli matrix acting in spin space and K complex conjugation, one can show that the matrix $w_{mn}(k) = \langle u_m(k)|T|u_n(-k)\rangle$ build from the Bloch wavefunctions for the $n-$th band $|u_n(k)\rangle$ is unitary. With T being antiunitary, we find that $w_{nm}(k) = -w_{mn}(-k)$ which we apply at the four special points in the two dimensional Brillouin zone that are time-reversal invariant, i.e. $k = \Gamma_i$ with $\Gamma_i = -\Gamma_i + G$ where G is a reciprocal lattice vector. Thus, the four matrices $w_{nm}(\Gamma_i)$ are antisymmetric. For antisymmetric matrices, we can define the Pfaffian ($Pf(A)^2 = det(A)$) which gives rise to the key quantities

$$\delta_i = \frac{Pf\left[w\left(\Gamma_i\right)\right]}{\sqrt{\det\left[w\left(\Gamma_i\right)\right]}} = \pm 1. \tag{1.1}$$

Choosing a continuous gauge for $|u_n(k)\rangle$ throughout the Brillouin zone, the branch-cut of the square-root function can be avoided and the Z_2 invariant can be computed from the δ_i at all four time-reversal invariant momenta, $(-1)^\nu = \Pi_i \delta_i$.

Unfortunately, the proposal about the novel topological state in graphene remained purely theoretical. The spin orbit coupling considered turned out to be negligible under experimental conditions. However, soon after Kane and Mele laid out the concept of a Z_2 time-reversal invariant insulator, Bernevig, Hughes and Zhang published a proposal based on a $HgTe$ heterostructure [14]. This proposal was immedeatly picked up by the Molenkamp group, the quantum well was fabricated and the conductance was measured [15], see Figure 1.2. It was found that, for a quantum well thickness larger than the predicted $d_c = 6.3$nm, the longitudinal conductance was measured to be close to $G = 2e^2/h$ and independent of sample width, indicating edge state transport. Indeed, each of the two edges of the quantum well sample is expected to harbor an edge dispersion as in Figure 1.1 with a single ballistic transport channel propagating in each direction. Further, it was

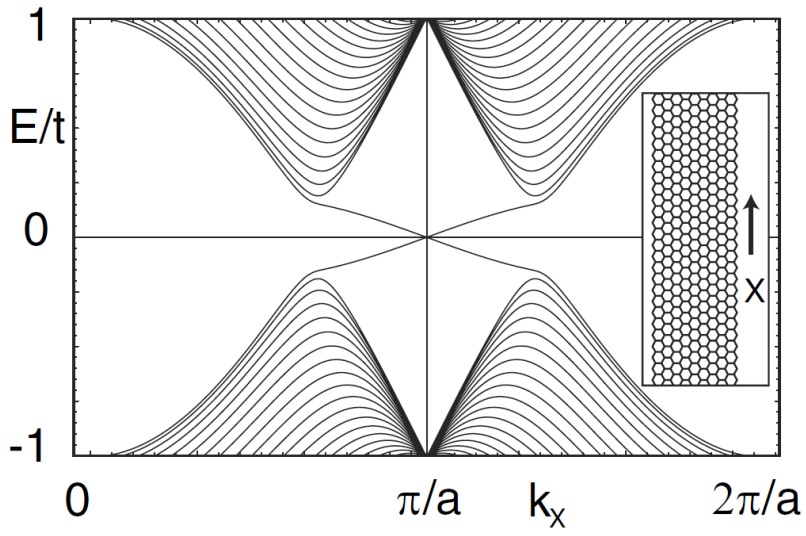

Figure 1.1: Theoretical prediction of edge states (crossing the bulk energy gap) for graphene equipped with spin orbit interaction. (Figure taken from reference [11].)

shown that this conductance could be destroyed by a small magnetic field. Only much later, the real space structure of the corresponding edge currents has been mapped out using their magnetic fields or an interference experiment based on the Josephson effect [16, 17].

Unlike quantum Hall systems, time-reversal invariant topological insulators have a counterpart in three spatial dimensions. The topological invariants characterizing the band structure are essentially generalizations of the two dimensional ones and were established in references [18, 19]. They will be further discussed in the context of dislocation line zero modes in section 2.2. Since in three dimensions, there are eight instead of four time-reversal invariant momenta, multiple gauge invariant combinations of the δ_i are possible: A complete set consists of four independent Z_2 invariants, organized as $(\nu_0; \nu_1, \nu_2, \nu_3)$. If the invariant ν_0 is non-trivial, the bandstructure is a 'strong' topological insulator with Dirac cone dispersions at an odd number of time-reversal invariant momenta of any surface Brillouin zone. If ν_0 is trivial (but $\boldsymbol{\nu} = (\nu_1, \nu_2, \nu_3)$ is non-trivial) the material is termed a 'weak' topological insulator which can be understood as a stack of two dimensional topological insulators. In this case, the one dimensional edge states give rise to an even number of Dirac cones as they hybridize across the two dimensional vertical boundaries. In contrast, the electronic structure of the surface perpendicular to the stacking direction is trivially gapped.

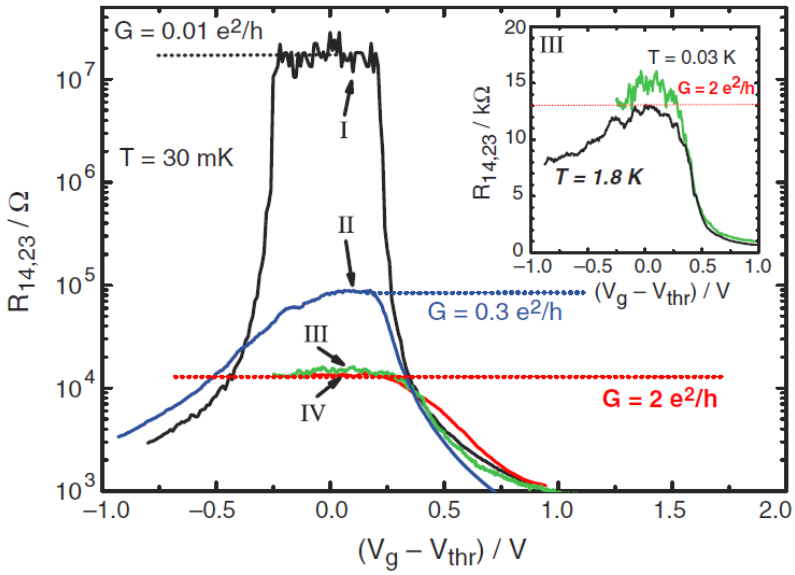

Figure 1.2: Longitudinal conductance for $CdTe/HgTe/CdTe$ quantum well structures of different geometries below (I) and above the critical thickness (II, III, IV), plotted versus gate voltage at cryogenic temperature of $T = 30mK$. The residual (edge-state) conductance in the topological regime was confirmed to be $G = 2e^2/h$ for short samples (III, IV) and is decreased when the sample length in transport direction exceeds the inelastic mean free path (sample II). (Figure taken from reference [15].)

Following theoretical predictions by Fu and Kane [20], Hsieh and coworkers studied the putative strong topological insulator alloy $BiSb$ using angle resolved photo electron spectroscopy (ARPES) to find compelling evidence for two dimensional Dirac surface states. After that breakthrough, a long list of three dimensional materials have been confirmed as strong and - more rarely - weak topological insulators, for a review with emphasis on material science aspects see [21].

We now proceed to topological band touching points in three dimensions. The simplest model is a two band Bloch Hamiltonian

$$H(\mathbf{k}) = f_0(\mathbf{k}) + f_x(\mathbf{k})\,\sigma_x + f_y(\mathbf{k})\,\sigma_y + f_z(\mathbf{k})\,\sigma_z \tag{1.2}$$

with f_i functions of crystal momentum $\mathbf{k}$. A band touching point, i.e. a degeneracy in Equation 1.2 requires that $f_x(\mathbf{k})$, $f_y(\mathbf{k})$ and $f_z(\mathbf{k})$ vanish simultaneously. Although it is not guaranteed that there exists such a degeneracy point (at $\mathbf{k}_0$) in the Brillouin zone, if it exists, it cannot be gapped by small perturbations to Equation 1.2 but merely moves around in the Brillouin zone.

A particular simple and elementary model of such a band touching point is a Weyl node, in the isotropic case described by

$$H_W(\mathbf{k}) = \hbar v\left(k_x\sigma_x + k_y\sigma_y + k_z\sigma_z\right) + \mu \tag{1.3}$$

with dispersion

$$E_\pm(\mathbf{k}) = \hbar v\sqrt{k_x^2 + k_y^2 + k_z^2} + \mu \tag{1.4}$$

where v is the Fermi velocity and μ the chemical potential. The dispersion in Equation 1.4 is depicted in Figure 1.3. If $\mu = 0$, the Fermi surface is a point at $\mathbf{k}_0 = 0$ and materials whose low energy quasiparticles could be described by Equation 1.3 are accordingly called Weyl semimetals. In the case $\mu \neq 0$, the Fermi surface is extended and spherical, the corresponding material is termed a Weyl metal.[1] As we show next, the topological properties of Equation 1.3 do not depend on the position of the Fermi energy.

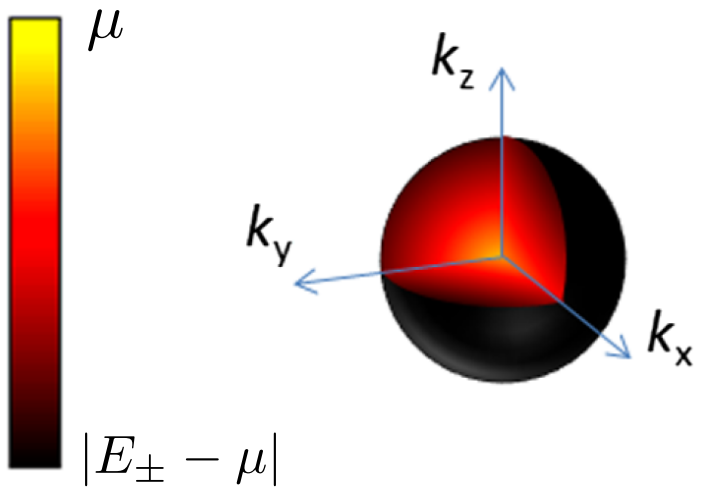

Figure 1.3: Graphical representation of Weyl node dispersion in k-space. (Adapted from [22].)

The stability argument pertaining to the Weyl point mentioned above can be put in terms where the similarity to topological insulators is more apparent. The topological invariants of topological insulators are all based on the notion of a gap in the band structure which is partially filled. The bandstructure in Equation 1.4 is gapped locally everywhere except at $\mathbf{k}_0$. If we define a closed surface in k-space around $\mathbf{k}_0$, the band structure on this surface resembles a two dimensional fully

[1] In literature, however, the term Weyl semimetal is used also for the case $\mu \simeq 0$.

gapped bandstructure (on a sphere, not on a torus, though). We can now calculate Berry curvature for one of the two bands (say, the low lying band) $\mathbf{A}_n(\mathbf{k}) = -i \langle u_n(\mathbf{k}) | \nabla_k | u_n(\mathbf{k}) \rangle$ and calculate the Chern flux $\mathbf{B}_n(\mathbf{k}) = \nabla_\mathbf{k} \times \mathbf{A}_n(\mathbf{k})$ as in the quantum Hall case. It turns out that the Weyl node in Equation 1.3 is a source of Chern flux

$$\rho(\mathbf{k}) = \frac{1}{2\pi} \nabla_\mathbf{k} \cdot \mathbf{B}_n(\mathbf{k}) = \delta(\mathbf{k} - \mathbf{k}_0). \tag{1.5}$$

Based on the similarity between magnetic flux and Chern flux, a Weyl node is often also called a monopole in the Brillouin zone.

A Weyl node radiates Chern flux in all directions, however in any realistic band structure, k-space is periodic and a single Weyl node configuration is thus not possible. This is the essence of the Fermion doubling theorem [23] which says that in any lattice regularization, Weyl nodes have to come in pairs, sources of Chern flux have to come with their respective sinks. Indeed, it turns out [24] that the more general Weyl node Hamiltonian

$$\tilde{H}_W(\mathbf{k}) = \sum_i \hbar v_i (\mathbf{n}_i \cdot \mathbf{k}) \sigma_i + \hbar v_0 (\mathbf{n}_0 \cdot \mathbf{k}) \tag{1.6}$$

with $\mathbf{n}_i$ linearly independent unit vectors has monopole strength sign $[\mathbf{n}_1 \cdot (\mathbf{n}_2 \times \mathbf{n}_3)]$.

Now, it is obvious how Weyl nodes can be gapped eventually: Merging two Weyl nodes with opposite charges will lead to a cancellation of chiral charge and a gapping of the spectrum. Merging two Weyl nodes with *equal* charges, however, will lead to a doubly charged Weyl node that is in general to be stabilized by point group symmetries of the crystal lattice.

Although not further addressed in the remainder of the thesis, a discussion of Weyl semimetals without mentioning their characteristic topological surface states would be incomplete. Consider some ideal Weyl material as in Figure 1.4(a) with a monopole and anti-monopole Weyl point separated by some finite distance along k_x in the bulk Brillouin zone. Imagine cutting the crystal to expose a surface perpendicular to the z-direction. Then there exists a Fermi arc separating occupied and empty surface states in the surface Brillouin zone. The Fermi arcs connect projections of Weyl points to the surface and are highly unusual since any generic two dimensional material will have closed lines as Fermi surfaces. In contrast, the closing of the Weyl metal's Fermi surface takes place on the opposite crystal surface by virtue of the other Fermi arc.

Let us explore how the appearance of these surface states can be explained. Since translational symmetry in the slab geometry in Figure 1.4(a) is preserved along x- and y-direction, all states in system can be labeled by $k_{x,y}$. Let us fix k_x, so that $\psi(x, y, z) = e^{ik_x x} f_{k_x}(y, z)$. Then the Hamiltonian reduces to a two dimensional one

with parameter k_x,

$$H_{k_x} f_{k_x}(y,z) = \varepsilon f_{k_x}(y,z) \tag{1.7}$$

which describes a two dimensional system with a boundary at, say $z = 0$. If two slices labeled by k_{x1}, k_{x2} have a Weyl point in between, $k_{x1} < k_{x,Weyl} < k_{x2}$, then their Chern number differs by one. If the Chern number was trivial for k_{x1}, it will be nontrivial for k_{x2}. This means that in this case, there is a gapless quantum Hall edge state at one edge momentum, k_y. The union of these one dimensional edge states at the points (k_x, k_y) in the surface Brillouin zone over all k_x in between the Weyl points constitutes the Fermi arc.

Not surprisingly, these peculiar surface Fermi arcs were among the first signatures looked for in Weyl material candidates. Weyl nodes have been first proposed as effective low energy theory for the dispersion in magnetically ordered pyrochlore iridate materials by Wan et al. [25]. Experimental realization was achieved in different (non-magnetic) materials, however. In short succession, Weyl nodes and Fermi arcs have been found using the ARPES technique in various material systems, the most prominent being $TaAs$, $NbAs$, TaP and NbP [26, 27, 28, 29, 30, 31]. It should be mentioned that bulk Weyl nodes have also been realized in inversion breaking photonic crystal bandstructures [32].

All standard Weyl node materials break inversion symmetry in their crystalline structure. Along with the time-reversal symmetry in non-magnetic materials, the presence of inversion symmetry enforces a fourfold degeneracy of band touching points and thus prevents the occurrence of doubly degenerate Weyl nodes. Such four fold degenerate Dirac nodes have been shown to exist for example in Cd_3As_2 and Na_3Bi [33, 34].

1.2 Elements of scattering theory

The notions of band topology or topological band touching points assume translational invariant and thus infinite systems. Such systems can be described using Fourier transformation and their topological properties are usually discussed in terms of the Eigenstates and Eigenenergies of Bloch Hamiltonians $H(\mathbf{k}) = e^{-i\mathbf{k}\cdot\mathbf{r}} H e^{i\mathbf{k}\cdot\mathbf{r}}$ where H is a Hamiltonian with a spatially periodic potential. We have already described the consequences of a transition to finite systems where a topological nontrivial bulk gives rise to topologically protected states that exist only at the boundary of the system. Both, in the cases of (three-dimensional) topological insulators and semimetals, these boundary states have been observed in experiment using photo-emission spectroscopy.

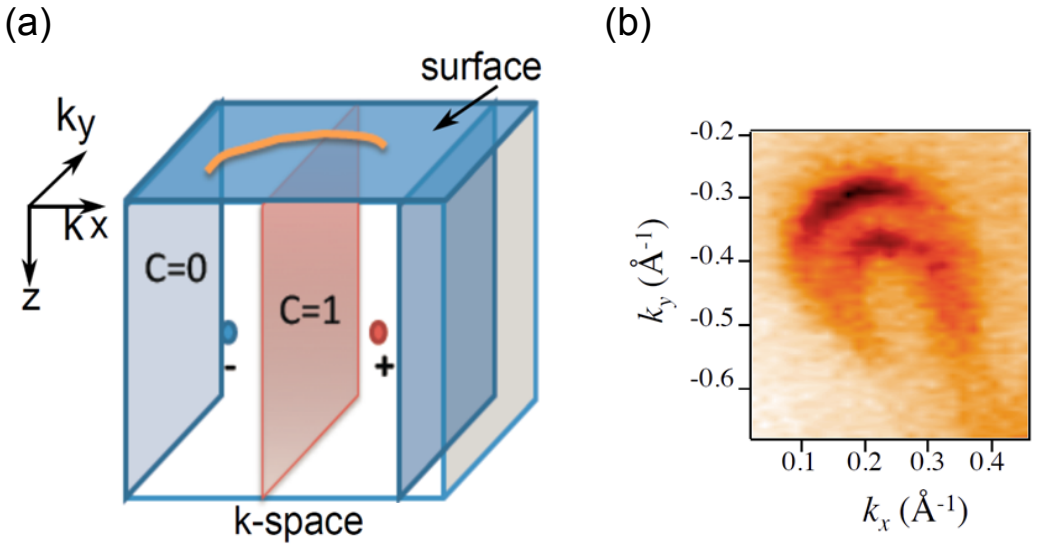

Figure 1.4: Fermi arcs as topological surface states of Weyl metals, explained in terms of chiral edge states of two dimensional slices through the Brillouin zone (a) and a pair of them in horseshoe like form as observed in ARPES data from $TaAs$ (b). (Figures taken from [24] and [27], respectively.)

Many powerful experimental techniques however rely on coupling to the finite system using physical contacts instead of using the radiation field as in ARPES. Moreover, in theoretical studies as well, the opening of the system by attaching leads as in Figure 1.5 is a valuable starting point. Under a few realistic assumptions to be detailed below, the scattering matrix S can be defined. It contains a plethora of information (and in some sense replaces the wavefunction ψ) that can be directly connected to experimental observables or used to study fundamental theoretical aspects of the underlying system.

In the following we briefly introduce the scattering matrix in some generality, show how it can be computed for a given system with leads in scenarios relevant in the later sections of this thesis and finally explain how to extract useful information from it. Parts of the following exposition are based on references [35, 36].

Definition of scattering matrix Let us consider a finite sample of interest connected to a left and right lead. The system is assumed to be quantum coherent, described by the Schrödinger equation with Hamiltonian H. In practice this requirement can be met by the use of small and cold samples. Let the left and right lead be described by Hamiltonian $H_{\mathrm{L,R}}$, respectively. Beyond coherence, we assume they are connected in a reflection-less manner to reservoirs that serve to

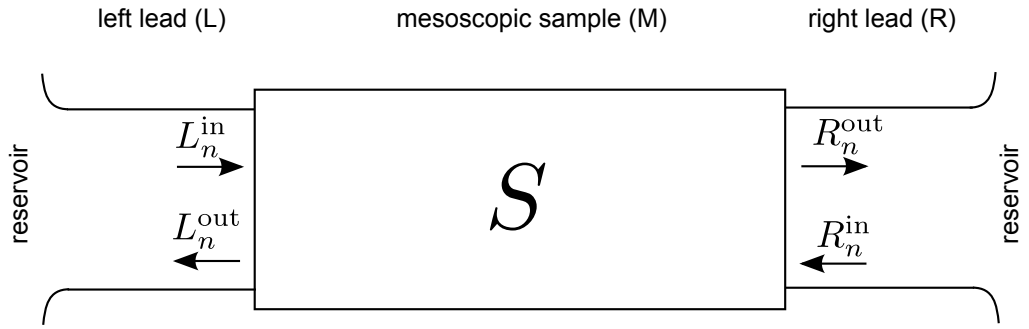

Figure 1.5: Definition of the scattering matrix S using propagating lead eigenstates at energy E. The leads are strongly coupled to reservoirs which control the electron distribution.

thermalize electrons in the leads. We emphasize that scattering theory in the form used in this thesis requires a non-interacting single particle setting. In experiment, such a description if often justified by Landau's Fermi liquid theory.

We are looking for eigenstates of the system in Figure 1.5 at energy E using the ansatz

$$\psi(\mathbf{r}) = \begin{cases} \sum_n L_n^{\text{in}} \psi_{\text{L},n}^{\text{in}}(\mathbf{r}) + L_n^{\text{out}} \psi_{\text{L,n}}^{\text{out}}(\mathbf{r}), & (\mathbf{r} \in L), \\ \psi_M(\mathbf{r}), & (\mathbf{r} \in M), \\ \sum_n R_n^{\text{in}} \psi_{R,n}^{\text{in}}(\mathbf{r}) + R_n^{\text{out}} \psi_{\text{R},n}^{\text{out}}(\mathbf{r}), & (\mathbf{r} \in R), \end{cases} \tag{1.8}$$

where we suppressed energy subscripts, used $\psi_{\text{L},n}^{\text{in,out}}$ and $\psi_{\text{R},n}^{\text{in,out}}$ as eigenstates of $H_{\text{L,R}}$, respectively, at energy E normalized to unit probability current pointing towards (in) or away from (out) the sample region. The complex numbers $L_n^{\text{in,out}}$ and $R_n^{\text{in,out}}$ are expansion coefficients in the chosen set of lead basis states and the function $\psi_M(\mathbf{r})$ solves the Schrödinger equation for Hamiltonian H and energy E. The solution (Equation 1.8) has to obey the usual continuity conditions at the L/M and M/R interfaces, so ψ_M will depend on $L_n^{\text{in,out}}$ and $R_n^{\text{in,out}}$ in a complicated fashion. Before we show how we can determine ψ_M and the expansion coefficients in the next section, we define the scattering matrix S as the linear transformation that relates a particular configuration of incoming lead modes to outgoing ones,

$$\begin{pmatrix} R_n^{\text{out}} \\ L_n^{\text{out}} \end{pmatrix} = \underbrace{\begin{pmatrix} t & r' \\ r & t' \end{pmatrix}}_{\equiv S} \begin{pmatrix} L_n^{\text{in}} \\ R_n^{\text{in}} \end{pmatrix}. \tag{1.9}$$

Current conservation implies the relation $|R_n^{\text{out}}|^2 + |L_n^{\text{out}}|^2 = |R_n^{\text{in}}|^2 + |L_n^{\text{in}}|^2$ which means that S is a unitary matrix, $S^\dagger = S^{-1}$.

A practical way to calculate scattering matrices for complex systems is to concatenate known scattering matrices of subsystems. In the case of two subsystems with scattering matrices S_1 and S_2, the scattering matrix of the composite system $S_{21} = S_2 \otimes S_1$ reads

$$S_{21} = \begin{pmatrix} t_2 R t_1 & r_2' + t_2 R r_1' t_2' \\ r_1 + t_1' r_2 R t_1 & t_1' \left[1 + r_2 R r_1'\right] t_2' \end{pmatrix} \tag{1.10}$$

where $R = \frac{1}{1 - r_1' r_2}$. Further subsystem scattering matrices could be concatenated iteratively. We will make use of Equation 1.10 in chapter 3.

Quantum transport properties from scattering matrix We now assume the presence of a particular incoming state, say in channel $\tilde{n}$ from the left. The scattering matrix can be used to find the resulting *scattering state* by using Equation 1.8 and Equation 1.9,

$$\psi_{L\tilde{n}}(\mathbf{r}) = \begin{cases} \psi_{\text{L},\tilde{n}}^{\text{in}}(\mathbf{r}) + \sum_n r_{n,\tilde{n}} \psi_{\text{L,n}}^{\text{out}}(\mathbf{r}), & (\mathbf{r} \in L), \\ \psi_M(\mathbf{r}), & (\mathbf{r} \in M), \\ \sum_n t_{n,\tilde{n}} \psi_{\text{R},n}^{\text{out}}(\mathbf{r}), & (\mathbf{r} \in R). \end{cases} \tag{1.11}$$

We can now ask how much of the (unit) probability current impinging from the left in mode $\tilde{n}$ will be transmitted to the right lead (third line), the result, as read off from the third line is $\sum_n |t_{n,\tilde{n}}|^2$.

More generally, we are interested in a formula that relates the electronic conductance $G = I/V$ (with I electrical current and V voltage bias between leads) to the scattering matrix. Following our initial assumptions about the role of the leads as reservoirs, all electrons coming from lead $\alpha = L, R$ have a Fermi-Dirac energy distribution characterized by chemical potential μ_α, $f_\alpha(E)$ until they thermalize in the same or opposite reservoir. The electric current in the right lead due to the states impinging from the left lead (like $\psi_{L\tilde{n}}$) in an energy interval dE can be obtained by multiplying their transmission probabilities $[t^\dagger t]_{\tilde{n}\tilde{n}}$ with their density of states $\frac{1}{2\pi}\frac{dk}{dE}$, the occupation probability $f_L(E)$, their group velocity $v = \frac{1}{\hbar}\frac{dE}{dk}$ and electron charge $-e$. An energy integral leads to

$$\begin{aligned} I_L &= -\int dE \, \frac{e}{h} \sum_{n,m} f_L(E) \, t_{n,m} t_{n,m}^* \\ &= -\int dE \, \frac{e}{h} f_L(E) \, Tr\left[tt^\dagger\right]. \end{aligned} \tag{1.12}$$

A similar equation holds for the current contribution of scattering states impinging from the right lead. Their contribution to the total current in the right lead however depends on the backscattering probability $[r'^{\dagger}r']_{\tilde{n}\tilde{n}}$ of the impinging wavepackets and is proportional to $-1 + [r'^{\dagger}r']_{\tilde{n}\tilde{n}}$ which by unitarity of S is equal to $-[t'^{\dagger}t']_{\tilde{n}\tilde{n}}$. The total current in the right lead (and - due to current conservation - in every crosssection) then is

$$I = -\int dE \, \frac{e}{h} \left(f_L(E) \, Tr\left[tt^{\dagger}\right] - f_R(E) \, Tr\left[t't'^{\dagger}\right] \right) \tag{1.13}$$

and the unitarity of S ensures $Tr\left[tt^{\dagger}\right] = Tr\left[t't'^{\dagger}\right]$. A finite voltage bias V across the sample is build in by demanding $\mu_R = -eV + \mu_L$. We finally have, with the assumption that the energy dependence of t can be omitted over a small range eV and a Taylor expansion $n_F(E - \mu_L) - n_F(E - \mu_L - eV) \simeq -(-eV) \frac{\partial n_F}{\partial E}$,

$$\begin{aligned} I &\simeq -Tr\left[tt^{\dagger}\right] \int dE \, \frac{e}{h} \left(f_L(E) - f_R(E) \right) \\ &= -Tr\left[tt^{\dagger}\right] \int dE \, \frac{e}{h} \left(n_F(E - \mu_L) - n_F(E - \mu_L - eV) \right) \\ &= V \frac{e^2}{h} Tr\left[tt^{\dagger}\right] \end{aligned} \tag{1.14}$$

from which we obtain the Landauer formula,

$$G = \frac{e^2}{h} Tr\left[tt^{\dagger}\right]. \tag{1.15}$$

Since the electron wavepackets are transmitted with finite transmission probability, the time dependent current $I(t)$ fluctuates around the mean value $I = GV$ as given by Equation 1.15. The ratio of the shot noise power S to $2eI$, also known as the Fano factor, can be shown [37] to be conveniently expressed from the scattering matrix as

$$F = \frac{S}{2eI} = Tr\left[tt^{\dagger}(1 - tt^{\dagger})\right] / Tr\left[tt^{\dagger}\right]. \tag{1.16}$$

Calculation of scattering matrices There exist various methods to calculate scattering matrices for concrete system and lead combinations. In general, the task to determine the linear dependencies between the coefficients $L_n^{\text{in,out}}$ and $R_n^{\text{in,out}}$ from Equation 1.8 respecting boundary conditions can be either performed numerically, or, in simple cases, analytically. Often, a recursive scheme employing the concatenation formula (Equation 1.10) can be used. In the following we present the principles behind a numerical scheme used in chapter 2 and show the analytic

approach exemplified for the case of a Weyl node Hamiltonian as further studied in chapter 3.

Often, one is interested in scattering matrices for systems and leads defined as tight-binding models described in the basis of localized orbitals created by $c_i^\dagger$,

$$H = \sum_{i,j} H_{ij} c_i^\dagger c_j \tag{1.17}$$

which can be further divided in an arbitrary hermitian sample Hamiltonian matrix H_S and one (or several) translational invariant lead parts, made of unit cell Hamiltonian H_L and lead hopping V_L. The sample is coupled to the lead using the hopping V_{LS}, in summary

$$H = \begin{pmatrix} \ddots & V_L & & \\ V_L^\dagger & H_L & V_L & \\ & V_L^\dagger & H_L & V_{LS} \\ & & V_{LS}^\dagger & H_S \end{pmatrix}, \qquad \psi = \begin{pmatrix} \vdots \\ \psi^L(3) \\ \psi^L(2) \\ \psi^L(1) \\ \psi^S \end{pmatrix}, \tag{1.18}$$

where we combined multiple leads to a single lead with disjoint sections. The software package KWANT [38] is dedicated to the creation and solution of scattering problems defined as in Equation 1.18. Due to Bloch's theorem for periodic systems, the eigenstates in the lead have the form $\phi_n(j) = (\lambda_n)^j \chi_n$ where $\left(H_L + V_L\lambda_n^{-1} + V_L^\dagger \lambda_n\right)\chi_n = E\chi_n$. From the normalization requirement, only $|\lambda_n| \leq 1$ is permissible: For $|\lambda_n| < 1$ the states are evanescent (decaying away from the sample), for $|\lambda_n| = 1$, the states are propagating with wavevector k_n defined as $\lambda_n = e^{ik_n}$. As mentioned above, the propagating modes are normalized to carry unit particle current: With $v = \dot{x} = -i[H, x]$ in units with $\hbar = 1$ and $x = \sum_j c_j^\dagger c_j \cdot j$ in the tight-binding basis, this yields

$$2\mathrm{Im}\left\langle \phi_n(j-1)|V_L|\phi_n\left(j-1\right)\right\rangle = \pm 1 \tag{1.19}$$

for incoming (+) and outgoing (-) modes. With these preparations, the scattering state for incoming channel n reads

$$\psi_n(i) = \phi_n^{in}(i) + \sum_m S_{mn}\phi_m^{out}(i) + \sum_p \tilde{S}_{pn}\phi_p^{ev}(i) \tag{1.20}$$

and for system $\psi_n(0) = \phi_n^S$. The latter is obtained numerically along with the scattering matrix S_{mn} by inserting Equation 1.20 in the Schrödinger Equation $H\psi_n = E\psi_n$ with H from Equation 1.18.

The continuum Hamiltonian of a single Weyl node,

$$H_0 = \hbar v \boldsymbol{\sigma} \cdot \mathbf{k}, \tag{1.21}$$

lacks a lattice regularization in terms of a tight-binding model due to the Fermion doubling theorem [23]. Therefore, the above numerical scheme to calculate the scattering matrix does not apply. Fortunately, it is possible to analytically calculate the scattering matrix [39, 3] by generalizing a procedure previously devised for two dimensional Dirac cones in reference [40]. We consider a setup as depicted in Figure 1.6 where the leads at $x < 0$ and $x > L$ are realized as highly doped Weyl nodes with large chemical potential eV^∞. We assume the width of the structure to be W in y- and z-direction and apply periodic boundary conditions.

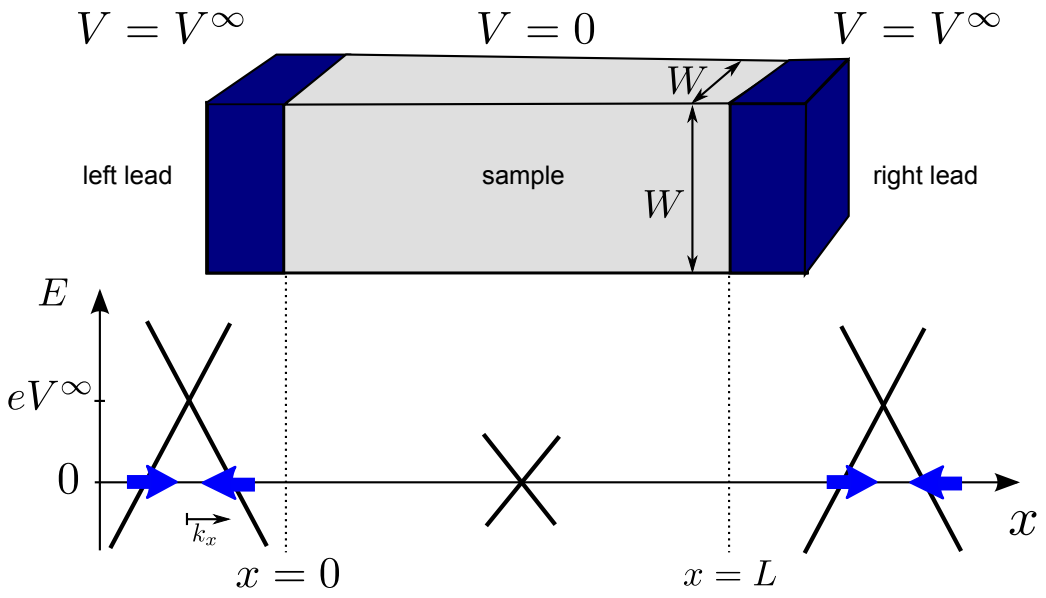

Figure 1.6: Quantum transport setup for a clean Weyl node H_0. The leads are realized as highly doped Weyl nodes. The scattering matrix can be calculated from the matching conditions of the piecewise eigenstates at the boundaries $x = 0$ and $x = L$. The dispersion relations in the lower section of the figure are shown for $k_{y,z} = 0$.

To solve the scattering problem for

$$H = H_0 + eV(x) \tag{1.22}$$

we make a plane wave Ansatz for the wavefunctions in the three regions $x < 0$,

$0 < x < L$, $L < x$ in which we find

$$E_\pm = \pm\hbar v\sqrt{k_x^2 + k_y^2 + k_z^2} + eV, \tag{1.23}$$

$$\psi_\pm \propto e^{i\mathbf{k}\cdot\mathbf{r}} \begin{pmatrix} k_z + (E_\pm - eV)/\hbar v \\ k_x + ik_y \end{pmatrix}, \tag{1.24}$$

where the signs denote conduction and valence band, respectively and $V = V^\infty$ in the leads while $V = 0$ in the sample region. We consider transport at the Fermi energy $E = 0$. In the leads, only propagating modes are possible with valence band wavevectors $\pm k_x \in \mathbb{R}$ where $k_x = \sqrt{(eV^\infty/\hbar v)^2 - k_y^2 - k_z^2}$, while in the sample region with energy at the nodal point, evanescent modes are allowed, thus k_x can be as well imaginary and will be labeled by $\pm\tilde{k}_x$ where $\tilde{k}_x = i\sqrt{k_y^2 + k_z^2}$. The remaining task is to match the piecewise solution at the interfaces. Since the (time-independent) Schrödinger equation for the Weyl node Hamiltonian is of first order only, it is sufficient to demand continuity of the wavefunction. Moreover, since the entire problem is translationally invariant in the transverse direction, the transversal wavenumbers $k_{y,z}$ are good quantum numbers that will not be mixed by the scattering matrix.

We fix $k_{y,z}$ to arbitrary values allowed by the boundary conditions ($k_{y,z} = 2\pi n_{y,z}/W$, $n_{y,z} \in \mathbb{Z}$) and start with assuming an incoming state (with wavevector $-k_x$) from the left. The scattering wavefunction reads

$$\Psi = \begin{cases} \frac{1}{\sqrt{v'\mathcal{N}}} \begin{pmatrix} k_z - eV^\infty/\hbar v \\ -k_x + ik_y \end{pmatrix} e^{-ik_x x} + \frac{r}{\sqrt{v'\mathcal{N}}} \begin{pmatrix} k_z - eV^\infty/\hbar v \\ k_x + ik_y \end{pmatrix} e^{ik_x x} & : x < 0 \\ \alpha \begin{pmatrix} k_z \\ -\tilde{k}_x + ik_y \end{pmatrix} e^{-i\tilde{k}_x x} + \beta \begin{pmatrix} k_z \\ \tilde{k}_x + ik_y \end{pmatrix} e^{i\tilde{k}_x x} & : 0 < x < L \\ \frac{t}{\sqrt{v'\mathcal{N}}} \begin{pmatrix} k_z - eV^\infty/\hbar v \\ -k_x + ik_y \end{pmatrix} e^{-ik_x(x-L)} & : x > L \end{cases} \tag{1.25}$$

where the transversal plane wave part has been suppressed, $\mathcal{N} = (k_z - eV^\infty)^2 + |-k_x + ik_y|^2$ is a normalization factor and $v' = 1/\hbar \cdot \partial E/\partial k_x$. Continuity of the wavefunction at $x = 0$ and $x = L$ yields four equations for the unknowns α, β, r and t. Their solution for the transmission amplitude t reads

$$t = \frac{1}{\cosh\left[\sqrt{k_y^2 + k_z^2}L\right] + i\frac{\sqrt{k_y^2+k_z^2}\mathrm{Sinh}\left[\sqrt{k_y^2+k_z^2}L\right]}{\sqrt{(eV^\infty/\hbar v)^2+k_y^2+k_z^2}}} \tag{1.26}$$

which in the highly doped lead limit $V^{\infty} \to \infty$ yields

$$t = \cosh\left[\sqrt{k_y^2 + k_z^2}L\right]^{-1}, \tag{1.27}$$

Similarly, solving for r in the highly doped lead limit, we obtain

$$r = -\frac{(k_y + ik_z)\tanh\left[\sqrt{k_y^2 + k_z^2}L\right]}{\sqrt{k_y^2 + k_z^2}}. \tag{1.28}$$

The scattering matrix elements t' and r' for backward transmission can be calculated from a scattering wavefunction with a lead state impinging on the sample from the right.

Finally, we calculate the conductance from Equation 1.15 where we apply $\sum_{m_y} \to \frac{W}{2\pi}\int dq_y$ valid for $W/L \gg 1$,

$$\begin{aligned} G &= \frac{e^2}{h}\sum_{m_y,m_z} \cosh^{-2}\left[\frac{2\pi L}{W}\sqrt{m_y^2 + m_z^2}\right], \\ &= \frac{e^2}{h}\left(\frac{W}{2\pi}\right)^2 \int_0^{\infty} 2\pi q dq \, \cosh^{-2}\left[Lq\right], \\ &= \frac{e^2}{h}\frac{W^2}{L^2}\frac{\ln 2}{2\pi} \\ &\simeq 0.11 \times \frac{e^2}{h}\frac{W^2}{L^2}. \end{aligned} \tag{1.29}$$

The inverse proportionality to L^2 can be seen as one of the characteristic and peculiar signatures of Weyl nodes in quantum transport. For the Fano factor, we obtain from Equation 1.16 in a similar fashion a size-independent value

$$F = 1/3 + (6\,ln2)^{-1} = 0.574. \tag{1.30}$$

1.3 Analytical and numerical methods for disordered systems

It is evident that the model Hamiltonians for topological insulators and semimetals as described above can only be a crude approximation to a realistic description of a material. Besides the inclusion of electron-electron interactions, realistic models should account for disorder due to the fact that experimental materials are never perfectly clean and periodic, but contain foreign atoms, vacancies, dislocations etc. In this thesis, we are particularly concerned with disorder effects in topologi-

cal insulators and semimetals and disregard electron-electron interactions. While disorder effects in normal metals are both well understood (scattering Bloch waves into each other, leading to a finite conductivity and, eventually Anderson localization), the effects of disorder in topological insulators and semimetals promise an even richer phenomenology.

In the case of topological insulators, it is evident that strong on-site disorder must render the system topologically trivial. This can be seen from the similarity between an atomic insulator and the tendency of disorder to create localized, independent states. Thus, one can expect disorder to drive topological phase transitions at some intermediate disorder strengths. In contrast, certain dislocation lines in topological insulators with nontrivial weak indices can be shown to host topological zero energy states propagating along the defect. The discussion of the precise conditions for and the underlying physics of dislocation line modes is relegated to section 2.2.

For semimetals, the density of states can vanish at the nodal energy. Disorder can be naively expected to flatten the density of states and in particular also to create states at the nodal energy. Thus, it is a nontrivial question if characteristic properties of clean semimetals hinging of the vanishing density of states survive in the presence of disorder. Moreover, one can expect that topological semimetal bandstructures have a peculiar behavior for strong disorder where their intrinsic Berry phase should ensure protection from localization.

Before dwelling on the above questions in chapter 2 and chapter 3 we will introduce disorder models widely used in this thesis and present methods to analyze disordered systems theoretically. We follow reference [41].

Disorder models In this thesis, besides the dislocations mentioned earlier, we are mainly concerned with quenched, static disorder that can be described by a three dimensional potential profile $V(\mathbf{r})$. In chapter 2 we will generalize this assumption by allowing also disorder types that cause spin- and orbital dependent scattering. The microscopic details and origin of the disorder potential are not discussed in this thesis since they are poorly understood for the materials in question. We further disregard any more complicated disorder types, for example magnetic impurities that are dynamic in the sense that their internal state can change and interact with degrees of freedom in the host material. We emphasize that static disorder leads to elastic (i.e. energy conserving) scattering only.

The actual potential profile in a sample is beyond the experimentalists control or knowledge. Likewise, it is as hope- as meaningless for analytical calculations to obtain results for a specific disorder profile $V(\mathbf{r})$. In contrast, regarding the disorder profile as a random variable with a given probability weight

function $P[V(\mathbf{r})]$ allows for analytical progress: Disorder averaged observables $\langle O \rangle_{dis} = \int P[V(\mathbf{r})] O_{V(\mathbf{r})}$ [with $O_{V(\mathbf{r})}$ the observable for a specific 'realization' $V(\mathbf{r})$] and fluctuations can often be calculated. This seems sound for comparisons to experimental conditions in which either a large number of disordered samples is measured or $V(\mathbf{r})$ can be repeatedly changed (i.e. by heating cycles). Even more fortunate, many physical observables are self-averaging, meaning that taking the thermodynamic limit in using large samples is equivalent to disorder averaging. In numerical simulations, which are of course capable of calculating results for specific realizations $V(\mathbf{r})$, the disorder average is implemented explicitly by averaging results for randomly generated $V(\mathbf{r})$ with the weight function.

A probability distribution $P[V(\mathbf{r})]$ can be described by its cumulants. It turns out that the Gaussian model is both realistic and simple to analyze,

$$P[V(\mathbf{r})] \propto \exp\left(-\int d\mathbf{r} d\mathbf{r}' V(\mathbf{r}) K^{-1}(\mathbf{r}-\mathbf{r}') V(\mathbf{r}')\right). \tag{1.31}$$

Only the second cumulant is non-zero,

$$\langle V(\mathbf{r}) V(\mathbf{r}') \rangle_{dis} = K(\mathbf{r}-\mathbf{r}') \tag{1.32}$$

and $K(\mathbf{r})$ is the disorder correlation function, in analytical treatments often approximated by a Dirac-delta function. A convenient choice for the disorder correlator in the numerical approach to the Weyl node Hamiltonian $H_0 = \hbar v \boldsymbol{\sigma} \cdot \mathbf{k}$ which we use throughout chapter 3 is

$$\langle V(\mathbf{r}) V(\mathbf{r}') \rangle_{dis} = \frac{K(\hbar v)^2}{\sqrt{2\pi}^3 \xi^2} e^{-\frac{|r-r'|^2}{2\xi^2}}. \tag{1.33}$$

The disorder correlation length ξ sets a lengthscale for the disordered Hamiltonian (note that H_0 alone has no intrinsic scale) and the dimensionless parameter K is a measure for the disorder strength as we can see from $K = \frac{1}{(\hbar v)^2 \xi} \int d\mathbf{r} \langle V(\mathbf{r}) V(\mathbf{r}') \rangle_{dis}$. A disorder potential obeying Equation 1.33 in a finite volume Ω can be conveniently created in reciprocal space where we assign for each of the discrete $\mathbf{k}$-vectors

$$V(\mathbf{k}) \;=\; \sqrt{K \xi \Omega} \hbar v \, (A_{\mathbf{k}} + i \cdot B_{\mathbf{k}}) / \sqrt{2\sigma^2} \, e^{-k^2 \xi^2 / 4} \tag{1.34}$$

with $A_{\mathbf{k}}$ and $B_{\mathbf{k}}$ random numbers drawn from a Gaussian distribution with variance σ^2 and mean $\mu = 0$.

In chapter 2, where we consider tight-binding models, it is convenient to specify

disorder in the local basis by

$$V = \sum_i V_i c_i^\dagger c_i \tag{1.35}$$

where V_i are uncorrelated from site to site and are randomly drawn from the interval $[-W/2, W/2]$, thus $\langle V_i \rangle_{dis} = 0$ and $\langle V_i V_j \rangle_{dis} = \delta_{ij} W^2/12$.

Disorder in the scattering matrix method We now discuss how transport properties of disordered systems can be analyzed using scattering theory. In a tight-binding model, disorder as in Equation 1.35 can be straight forwardly incorporated in the scheme around Equation 1.18. The situation for continuum models like the Weyl node Hamiltonian with smoothly defined disorder as in Equation 1.33 calls for a more refined treatment as summarized in Figure 1.7. In a first step, the smooth disorder potential $V(x, y, z)$ is approximated by equidistant slices stacked in transport direction (x-direction),

$$V(x, y, z) = \sum_n V_n(y, z) \Delta x \delta(x - x_n), \tag{1.36}$$

where $V_n(y, z) = \frac{1}{\Delta x} \int_{x_{n-1}}^{x_n} dx\, V(x, y, z)$ which is a good approximation if $\Delta x \ll \xi$. In a next step, we compute the scattering matrix $S_{dis}^{(n)}$ of the n-th slice potential $V_n(y, z)\Delta x \delta(x - x_n)$ between two leads. This can be done in Born approximation where the transmission block is $t \simeq 1 + iT$ with $T_{nm} = \frac{1}{\hbar} \left\langle \psi_{\mathrm{R},m}^{\mathrm{out}} | V_n(y, z) \Delta x | \psi_{\mathrm{L},n}^{\mathrm{in}} \right\rangle$ and $r \simeq iR$ where $R_{nm} = \frac{1}{\hbar} \left\langle \psi_{\mathrm{L},m}^{\mathrm{out}} | V_n(y, z) \Delta x | \psi_{\mathrm{L},n}^{\mathrm{in}} \right\rangle$, valid if T and R have only entries with magnitude much smaller than unity. This can be assured for every disorder potential by choosing Δx small enough. In the Weyl node example, where lead modes are plane waves in transversal direction labeled by k_y, k_z and σ_x eigenstates (with eigenvalues depending on their propagation direction, see Equation 1.24), T is essentially given by a two dimensional Fourier transform in transverse directions and $R = 0$ due to vanishing spinor overlap between right- and left-moving lead modes. The remaining task is to restore unitarity of the scattering matrices $S_{dis}^{(n)}$ by replacing $t \simeq 1 + iT \to (1 - iT/2)^{-1} (1 + iT/2)$ where the latter expression agrees to the first one up to linear order in T but is evidently unitary. Finally, using the concatenation formula for scattering matrices, Equation 1.10, we find the scattering matrix of the disordered sample as

$$S = S_0(\Delta x) \otimes S_{dis}^{(1)} \otimes S_0(\Delta x) \otimes S_{dis}^{(2)} \otimes \cdots \otimes S_{dis}^{(n)} \tag{1.37}$$

where $S_0(\Delta x)$ is the scattering matrix for a clean slice of the material in question.

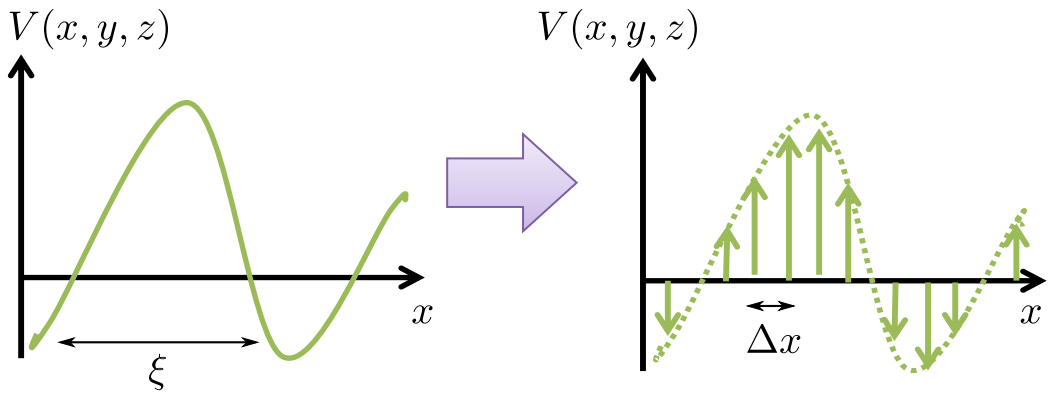

Figure 1.7: Iterative method to calculate a scattering matrix for disordered systems with smooth disorder potential that can be approximated by slices. The slice scattering matrices can be computed perturbatively and are concatenated sandwiched with free propagation in between to yield the full sample scattering matrix.

Self-consistent Born approximation One of the most useful and basic quantities for the models studied in this thesis is the (imaginary time) Green function in the presence of the disorder potential $V(\mathbf{r})$,

$$G(i\omega_n) = \frac{1}{i\omega_n - H(\mathbf{k}) - V(\mathbf{r})}. \tag{1.38}$$

As the Green function contains information about quasiparticle propagation, its disorder average could provide us with valuable insights for quasiparticle scattering, density of states or enters as building blocks into various correlation functions. We will now calculate the disorder average, following reference [42]. Due to the appearance of $V(\mathbf{r})$ in the denominator in Equation 1.38, before the disorder average can be computed, a perturbative expansion in powers of V is performed as schematically shown in Figure 1.8(a). In (b), the disorder average is taken, making use of the the Gaussian disorder correlations assumed: Any disorder average over a diagram with an odd number of disorder scattering events vanishes, while for even numbers, we apply Wick's theorem

$$\left\langle V_{\mathbf{k}_1} V_{\mathbf{k}_2} ... V_{\mathbf{k}_{2n-1}} V_{\mathbf{k}_{2n}} \right\rangle_{dis} = \sum_P \left\langle V_{\mathbf{k}_{P(1)}} V_{\mathbf{k}_{P(2)}} \right\rangle_{dis} ... \left\langle V_{\mathbf{k}_{P(2n-1)}} V_{\mathbf{k}_{P(2n)}} \right\rangle_{dis} \tag{1.39}$$

where the sum is over all permutations P. The individual disorder correlators (depicted by dashed lines) need to be specified for the particular disorder model in

use, see Equation 1.33. Due to translational invariance $\langle V(\mathbf{r})V(\mathbf{r}')\rangle_{dis} = K(\mathbf{r}-\mathbf{r}')$ we have $\langle V_{\mathbf{k}}V_{\mathbf{q}}\rangle_{dis} \propto \delta_{\mathbf{k},-\mathbf{q}}$ and the disorder averaged Green function $\langle G(i\omega_n)\rangle_{dis}$ is diagonal in momentum $\mathbf{k}$. The resulting terms in (b) can be divided into 'reducible' and 'irreducible' diagrams, a diagram is 'reducible' if it can be cut in two pieces by cutting a single internal fermion line. All irreducible diagrams, with external legs amputated constitute the self-energy Σ, shown in (c). It is easy to see that the disorder averaged Green function can be obtained iteratively using the self-energy as in (d) where the summation of the series yields the Dyson equation with solution

$$\langle G(i\omega_n)\rangle_{dis} = \frac{1}{i\omega_n - H(\mathbf{k}) - \sum_{\mathbf{k},\omega_n}}. \tag{1.40}$$

The interpretation of the self-energy is straightforward when divided in a real (hermitian) and imaginary (anti-hermitian) part. The real part accounts for the disorder induced renormalization of the clean Hamiltonian H. While in ordinary metals this effect is quantitatively and qualitatively negligible, for the topological insulator model studied in chapter 2 it will be shown that this effect is responsible for a variety of disorder induced topological phase transitions [43]. The imaginary part can be rewritten by $\mathrm{Im}\sum = -i\,\mathrm{sgn}(\omega)/2\tau$ which, by transforming to a real space Green function can be interpreted as a finite lifetime τ of the quasiparticles which propagate through the disordered environment.

Having arrived at Equation 1.40 we are left to calculate the self-energy according to Figure 1.8(c) where the first few terms are labeled as (i), (ii) and (iii). Unfortunately, it is impossible to sum up the series of diagrams exactly so we have to discuss approximations in Figure 1.9. The simplest approximation is the Born approximation (lowest order in V) which takes into account only diagram (i). By replacing the bare propagator in the Born approximation expression for Σ by $\langle G(i\omega_n)\rangle_{dis}$ (which already contains Σ), also the rainbow like diagrams of type (iii) are captured in the self-energy. Due to the self-consistency condition on Σ (appearing on both sides of the equation), this is called the self-consistent Born approximation (SCBA). The remaining type of diagram in the exact expression of the self energy is said to be of 'crossing'-type, (ii). It can be shown to be parametrically suppressed relative to diagram (iii) by a factor $1/k_F l$ where $l = \tau v_F$ is the mean free path. It is obvious that for Dirac materials like Weyl nodes with Fermi energy at the nodal point, i.e. $k_F = 0$, the suppression of diagram (ii) is not operational and we will have to resort to exact numerical calculations.

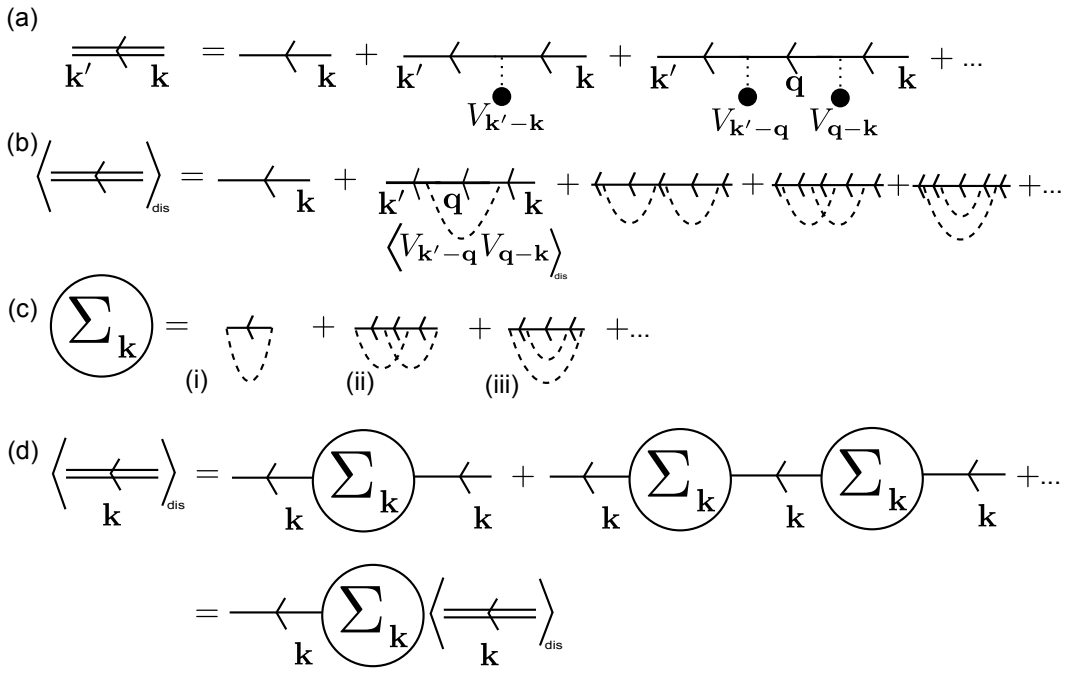

Figure 1.8: Diagrammatic treatment of disorder in perturbation theory. After a perturbative expansion of the Green function is performed in (a), the disorder average in taken in (b), assuming Gaussian disorder. The resulting diagrams can be reorganized in (d) using the self-energy (c). Green functions of the clean Hamiltonian are denoted by single lines.

1.4 Outline of the thesis

We now give an outline of the structure of this thesis. After having introduced the materials and some of their model Hamiltonians followed by a brief introduction of theoretical tools to study disorder effects in chapter 1 we now proceed to present the results of this thesis. Next, chapter 2 is concerned with selected disorder effects in three dimensional topological insulators and chapter 3 with topological Weyl semimetals. Each chapter starts with an introductory paragraph giving further details on the methods and models before the reprinted journal papers are presented. Conclusions reflecting about the wider picture are presented in chapter 4. There we also provide an outlook to possible future research.

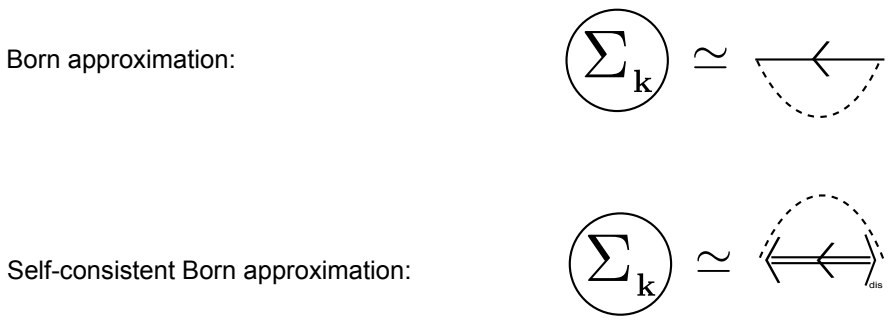

Figure 1.9: Approximate calculation of the self-energy in Born- and self-consistent Born approximation (SCBA).

2 Disorder effects in topological insulators

2.1 Topological phase diagram in the presence of on-site disorder

After having introduced topological insulators and argued for the importance of disorder in chapter 1, we will now discuss the main conceptual idea behind the first paper presented in this chapter, reference [1] titled *"Z2 Phase diagram of three-dimensional disordered topological insulators via a scattering matrix approach"*, DOI: 10.1103/PhysRevB.89.155311. The question is if and how topological insulators reveal their non-trivial topological nature in terms of their scattering matrix if they are opened up by attaching leads. On an intuitive level, the answer is clearly affirmative: A topological insulator as a gapped state of matter should not support any transmission from one side to the other if the system is large enough, thus the transmission amplitudes in the scattering matrix vanish, $t \equiv 0$. On the other hand, the properties of the unitary reflection block r should be sensitive to the electronic structure at the surface of the topological insulator and thus to the presence of surface states.

Time-reversal symmetry and scattering matrices In the following, we will put this intuition on a solid analytical footing following earlier works of Meidan, Micklitz and Brouwer [44, 45] as well as Fulga, Hassler and Akhmerov [46]. In a scattering setup with a time-reversal invariant Hamiltonian H, let $\{\psi_n^{in}\}_n$ be a basis in the space of incoming lead modes, and accordingly $\{\psi_n^{out}\}_n$ a basis in the space of outgoing modes. By definition, the scattering matrix at energy E satisfies

$$(H - E)\left(\psi_n^{in} + \sum_m S_{mn}\psi_m^{out} + \psi_{loc}\right) = 0 \tag{2.1}$$

where the right parentheses represent the scattering wavefunction for incoming mode ψ_n^{in}. We will now investigate what time-reversal symmetry, defined for H as $TH = HT$, means at the level of the scattering matrix S.

We prepare Equation 2.1 for acting with the antiunitary time-reversal operator T. By definition, $TH = HT$ and thus the incoming lead state at momentum $\mathbf{k}$ is transformed to a state at momentum $-\mathbf{k}$ and the same energy E,

$$T\psi_n^{in}(\mathbf{r}) = Te^{i\mathbf{kr}}\psi_n^{in}(0) = e^{-i\mathbf{kr}}T\psi_n^{in}(0).$$

Using the expression for the group velocity, $\mathbf{v} \propto dE/d\mathbf{k}$, we find that $T\psi_n^{in}$ is an outgoing state and as such is related to the basis $\{\psi_n^{out}\}_n$ by some unitary transformation V. Repeating the argument for the time reversed partner of ψ_m^{out}, we arrive at

$$T\psi_n^{in} = \sum_k V_{nk}\psi_k^{out}, \tag{2.2}$$

$$T\psi_m^{out} = \sum_i Q_{mi}\psi_i^{in}. \tag{2.3}$$

We now apply T from the left to Equation 2.1, which just acts as complex conjugation on the complex scalar S_{mn},

$$T(H-E)\left(\psi_n^{in} + \sum_m S_{mn}\psi_m^{out} + \psi_{loc}\right) = 0 \tag{2.4}$$

$$(H-E)\left(T\psi_n^{in} + \sum_m S_{mn}^* T\psi_m^{out} + T\psi_{loc}\right) = 0 \tag{2.5}$$

$$(H-E)\left(\sum_k V_{nk}\psi_k^{out} + \sum_{m,i}(S^*)_{mn}Q_{mi}\psi_i^{in} + \psi'_{loc}\right) = 0 \tag{2.6}$$

where the time-reversed wavefunction in the sample region is $\psi'_{loc} \equiv T\psi^{loc}$. We multiply with $\sum_n \left(\left[S^\dagger Q\right]^{-1}\right)_{jn}$ and compare to Equation 2.1 to read off

$$S = V^T S^T Q^* \tag{2.7}$$

Finally, acting with T on Equation 2.2 and using Equation 2.3, we obtain $T^2\psi_n^{in} = \sum_k TV_{nk}\psi_k^{out} = \sum_{k,i} V_{nk}^* Q_{ki}\psi_i^{in}$ and employing $T^2 = -1$ for spinful electrons, we find $-1 = V^*Q$ which can be inserted in Equation 2.7 to simplify the time-reversal invariance constraint on S,

$$SV = -V^T S^T. \tag{2.8}$$

Topological classification of time-reversal invariant scattering matrix So far, Equation 2.8 applies in all dimensions. We now aim to specialize to two dimen-

sional systems, where we argued for a Z_2 classification in chapter 1 based on the phase winding of Bloch wavefunctions as the crystal momentum $\mathbf{k} = (k_x, k_y)$ swept certain trajectories in the Brillouin zone. In the scattering approach, the system is necessarily finite (and not periodic) in the transport direction taken to be the the x-direction. We control k_y in y-direction by wrapping one unit cell of the system on a cylinder and applying a flux $\phi = ak_y$, see Figure 2.1(a). For disordered systems, the Bloch momentum k_y is meaningless but the flux construction (that is equivalent to periodic boundary conditions twisted by a phase $e^{i\phi}$) still can be applied [47]. Note that the flux changes its sign under the action of time-reversal symmetry, $\phi \to -\phi$. Repeating the above derivation for this 'adiabatic quantum pump' setting with the flux ϕ as a parameter, we find as a condition

$$S(\phi)V = -V^T S^T(-\phi). \tag{2.9}$$

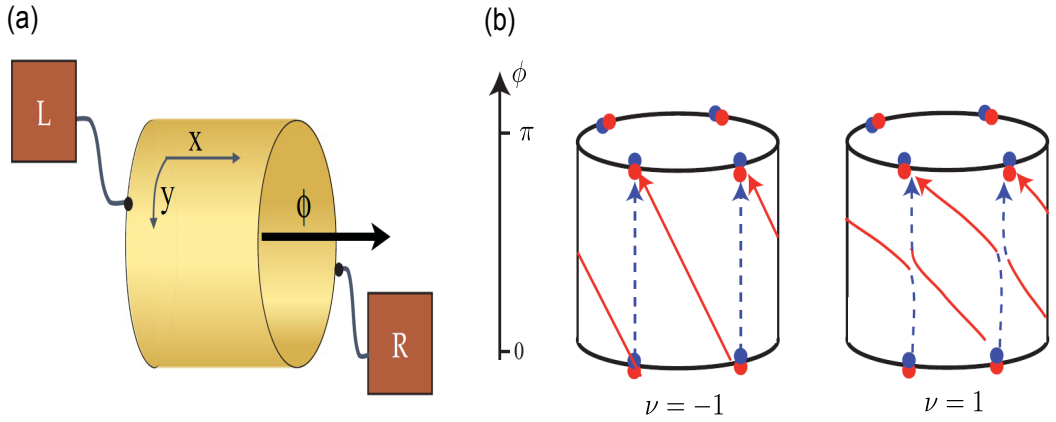

Figure 2.1: Schematic drawing of a two dimensional adiabatic quantum pump with left and right lead attached (a) and topological classification of associated eigenvalue phase winding of the scattering matrix S as the pump parameter is varied from $\phi = 0$ to π (b). (Figure adapted from reference [45].)

Like for the Brillouin zone topological classification, the topological invariant is encoded in the evolution of $S(\phi)$ as ϕ varies on a trajectory. To see how the invariant is constructed in an intuitive way, let us fix the basis $\{\psi_n^{out}\}_n$ such that $V^T = -V$. Writing the unitary $S(\phi)$ as a matrix exponential with a Hermitian matrix $h(\phi)$, $S(\phi) = e^{ih(\phi)}$, Equation 2.9 yields

$$S(\phi) = e^{ih(\phi)} = -V^T e^{ih^T(-\phi)} V^\dagger = -V^T e^{ih^*(-\phi)} V^\dagger = V e^{ih^*(-\phi)} V^\dagger = e^{iVh^*(-\phi)V^\dagger}$$

where we read off that at the time-reversal invariant points of the pump cycle,

$\phi = 0, \pi$ (where $\phi = -\phi \bmod 2\pi$) the Hermitian matrix fulfills $h = Vh^*V^\dagger$, i.e. Hamiltonian time-reversal symmetry. Then, by Kramer's theorem, h has degenerate (real) Eigenvalue pairs and thus the Eigenvalues $e^{i\phi_j}$ of S come in pairs at $\phi = 0, \pi$. The topological classification rests on the Eigenvalue evolution as $\phi : 0 \to \pi$. In the nontrivial case, the eigenvalues switch partners, see Figure 2.1(b). Any crossing of eigenvalues at $0 < \phi < \pi$ is non-generic and will be avoided by perturbations.

The classification scheme outlined above can be conveniently implemented numerically. As discussed in the paper below, the adaption for three dimensional time-reversal insulators is straightforward. It turns out that the actual calculation of the scattering matrix for a large tight-binding system as detailed in chapter 1 is by far more efficient numerically than an exact diagonalization of the same system. As an application, this enables us to determine the topological phase diagram for large disordered tight-binding systems where other approaches based on diagonalization would be vastly inefficient. In this way, we are able to shed light on some aspects of these phase diagrams that have been speculative before.

PHYSICAL REVIEW B **89**, 155311 (2014)

$\mathbb{Z}_2$ phase diagram of three-dimensional disordered topological insulators via a scattering matrix approach

Björn Sbierski and Piet W. Brouwer
Dahlem Center for Complex Quantum Systems and Institut für Theoretische Physik, Freie Universität Berlin, D-14195, Berlin, Germany
(Received 29 January 2014; published 15 April 2014)

The role of disorder in the field of three-dimensional time-reversal-invariant topological insulators has become an active field of research recently. However, the computation of $\mathbb{Z}_2$ invariants for large, disordered systems still poses a considerable challenge. In this paper, we apply and extend a recently proposed method based on the scattering matrix approach, which allows the study of large systems at reasonable computational effort with few-channel leads. By computing the $\mathbb{Z}_2$ invariant directly for the disordered topological Anderson insulator, we unambiguously identify the topological nature of this phase without resorting to its connection with the clean case. We are able to efficiently compute the $\mathbb{Z}_2$ phase diagram in the mass-disorder plane. The topological phase boundaries are found to be well described by the self-consistent Born approximation, both for vanishing and finite chemical potentials.

DOI: 10.1103/PhysRevB.89.155311 PACS number(s): 72.10.Bg, 72.20.Dp, 73.22.−f

I. INTRODUCTION

Time-reversal-invariant (TRI) topological insulators, a class of insulating materials with strong spin-orbit coupling, have attracted a great amount of attention in recent years. While clean systems are fairly well understood [1,2], an important theme in current topological insulator research is the study of disorder. Aside from being crucial for the interpretation of experimental data, disorder is of fundamental interest: Generically, disorder localizes electron wave functions and thus is expected to counteract nontrivial topology, which, as a global property, requires the existence of extended wave functions in the valence and conduction bands. One of the defining properties of strong topological insulator (STI) phases is their unusual stability: extended bulk states and gapless edge states persist for weak to moderately strong disorder. With increasing disorder strength, the bulk gap gets filled with localized electronic states, the mobility gap decreases, and, finally, at the topological phase transition, the mobility gap closes and the surface states at opposite surfaces gap out via an extended bulk wave function [3].

However, disorder physics in topological insulators is much richer than suggested by the simple scheme above. A drastic example is provided by the topological Anderson insulator transition, where increasing disorder drives an ordinary insulator (OI) into a topologically nontrivial phase [4–8]. Moreover, the role of different disorder types [9] or spatially correlated disorder [10] has been addressed in the literature. Further, weak topological insulator (WTI) phases known to be protected by translational symmetry were shown to be surprisingly stable against almost all disorder types allowed by discrete symmetries [11–13].

One of the challenges in the field of disordered topological insulators is the computation of the $\mathbb{Z}_2$ invariants that characterize strong and weak topological insulator phases. (Without disorder, the $\mathbb{Z}_2$ invariants can be computed directly from the band structure [1,2,14].) While methods based on exact diagonalization are applicable for two-dimensional systems, their performance for three-dimensional systems is rather poor [8,15,16]. For example, a recent study [16] was only able to map the $\mathbb{Z}_2$ invariant for a few lines in the disorder strength–Fermi energy plane for a system of $8 \times 8 \times 8$ lattice sites, leaving uncertainties about the possibility to infer qualitative and quantitative behavior in the experimentally relevant thermodynamic limit. As an example of an indirect method for calculating the $\mathbb{Z}_2$ invariant, the three-dimensional topological Anderson insulator was argued to be topologically nontrivial by employing the Witten effect [7]. The transfer-matrix method can be used to obtain Lyapunov exponents in a finite-size scaling analysis [17,18], which is then used to infer information on topological phase boundaries. Drawbacks of this method include difficulties in the determination of the phase boundary between two insulating phases since size dependence of the decay length is intrinsically small on both sides of the transition. In the case of a transition between an insulating topologically trivial and nontrivial phase, application of open boundary conditions allows for a facilitated detection of the resulting insulator- (surface-)metal transition. However, this causes a much stronger finite-size effect and renders the interpretation of the results for finite system sizes rather difficult. For example, a recent transfer-matrix study [19] speculates about a novel "defeated WTI" region in the phase diagram, whose precise nature and properties have not been finally resolved.

As a numerically inexpensive alternative, Fulga *et al.* proposed to obtain the topological invariants from a topological classification of the scattering matrix of a topological insulator [20]. As a Fermi surface quantity, the computational requirements for the calculation of the scattering matrix scale favorably, so that it is accessible with modest effort. The method requires the application of periodic boundary conditions and considers the dependence of the scattering matrix on the corresponding Aharonov-Bohm fluxes. In two dimensions, there is only one flux, and the method effectively classifies a "topological quantum pump" [21–23], via a mapping similar to that devised by Laughlin to classify the integer quantized Hall effect [24].

In this paper, we report on the application of a scattering-matrix-based approach to a disordered three-dimensional topological insulator model [25–27] that features both strong and weak topological insulator phases. In Sec. II, we review the

theory and discuss the practical implementation of the method, which more closely follows the ideas of Ref. [22], and differs from that of Ref. [20] at some minor points. The relation to the band-structure-based approach is discussed in Sec. III. In Sec. IV, we present the phase diagram in the mass-disorder strength plane. In contrast to Ref. [19], we see no evidence of a "defeated WTI" phase. We conclude in Sec. V. Two appendices contain details on analytic modeling of the scattering matrix for the clean limit and an assessment of finite-size effects.

II. SCATTERING THEORY OF THREE-DIMENSIONAL TOPOLOGICAL INSULATORS

The tight-binding model we consider is a variant of the widely used low-energy effective Hamiltonian of the Bi_2Se_3 material family [25–27]. In the absence of disorder, the momentum-representation Hamiltonian reads as

$$H_0(\mathbf{k}) = \tau_z \left[m_0 + 2m_2 \sum_{i=x,y,z} (1-\cos k_i) \right] + A\tau_x \sum_{i=x,y,z} \sigma_i \sin k_i + \mu, \tag{1}$$

where Pauli matrices σ_i and τ_i refer to spin and orbital degrees of freedom, respectively. For definiteness, we set $A = 2m_2$ and choose energy units such that $m_2 = 1$. The system has time-reversal symmetry $T H_0(\mathbf{k}) T^{-1} = H_0(-\mathbf{k})$, inversion symmetry $I H_0(\mathbf{k}) I^{-1} = H_0(-\mathbf{k})$, and, if $\mu = 0$, particle-hole symmetry $P H_0(\mathbf{k}) P^{-1} = -H_0(-\mathbf{k})$. Here, $T = i\sigma_y K$ is the time-reversal operator (K complex conjugation, $T^2 = -1$), $I = \tau_z$ the inversion operator, and $P = \tau_y\sigma_y K$ the particle-hole conjugation operator ($P^2 = 1$).

The full Hamiltonian

$$H = H_0 + V \tag{2}$$

includes an onsite disorder potential V that respects time-reversal symmetry. The most general form of the disorder potential V is

$$V(\vec{r}) = \sum_{\mathbf{r}} \sum_{d=1}^{6} w_{d,\mathbf{r}} (\sigma\tau)_d \,, \tag{3}$$

where the summation is over all lattice sites $\vec{r}$, and $\{\sigma\tau\} = \{1, \tau_x, \tau_y\sigma_x, \tau_y\sigma_y, \tau_y\sigma_z, \tau_z\}$. The amplitudes $w_{d,\mathbf{r}}$ are drawn from a uniform distribution in the interval $-W_d/2 < w_{d,\vec{r}} < W_d/2$. The disorder potential breaks inversion symmetry; the terms w_1, w_3, w_4, and w_5 also break particle-hole symmetry. We consider a lattice of size $L_x \times L_y \times L_z$ and apply periodic boundary conditions in the x and z directions, but open boundary conditions at the surfaces at $y = 0$ and $L_y - 1$. Following, we first discuss the case of potential disorder only ($W_1 \equiv W$, $W_d = 0$ for $d > 1$), and return to the other disorder types at the end of our discussion.

Our main focus will be on the case $\mu = 0$ where, without disorder, three different topological phases appear inside the parameter range $m_0 \in [-5,4]$, which is the parameter range we consider here. For $m_0 < -4$, the model is in the WTI phase, with topological indices $(\nu_0, \nu_x\nu_y\nu_z) = (0,111)$; for $-4 < m_0 < 0$, it is in the STI phase with indices (1,000); for $m_0 > 0$, the system is in the OI phase with indices (0,000). The inversion symmetry of the clean model with $\mu = 0$ ensures that bulk gap closings exist at the topological phase transitions at $m_0 = 0$ and -4 only [28].

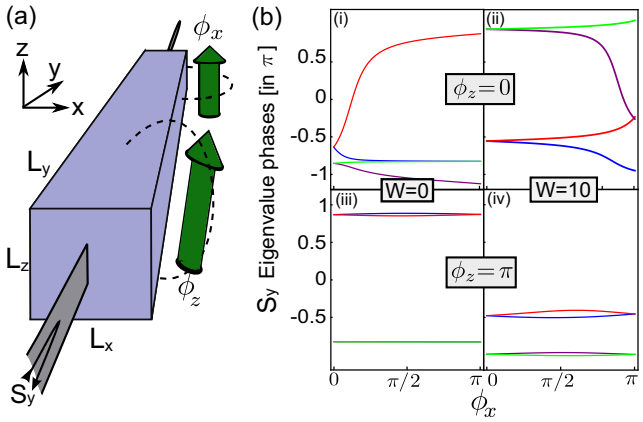

FIG. 1. (Color online) (a) Setup of the scattering problem with leads in the y direction and twisted periodic boundary conditions in the x and z directions. (b) Typical eigenphase evolution of $S_y(\phi_x,\phi_z)$ under continuous variation $\phi_x : 0 \to \pi$ for $m_0 = -1$ (red) and $\mu = 0$ in the clean case $W = 0$ [panels (i), (iii)] and with potential disorder $W = 10$ [panels (ii), (iv)]. For $\phi_z = 0$ [panels (i), (ii)], a nontrivial winding is obtained, while $\phi_z = \pi$ [panels (iii), (iv)] shows a trivial winding.

In order to obtain a scattering matrix, we open up the system by attaching two semi-infinite, translation-, and time-reversal invariant leads to both surfaces orthogonal to, say, the y direction, as shown in Fig. 1(a). The leads are described by a tight-binding model, defined on the same lattice grid as the bulk insulator. In principle, for the scattering matrix method, the leads can be generic and are to be chosen as simple as possible for fast computation. However, for reasons related to numerical robustness, we choose a lead that is one site wide in the x direction, but two sites wide in the z direction. (We refer to Appendix A for a detailed discussion why in this case a strictly one-dimensional chain is less well suited for the purpose of topological classification.) The y coordinates of the lead sites $\vec{r}$ are $y < 0$ and $y \geqslant L_y$. Without loss of generality, the x and z coordinates of the lead sites are fixed at $x = 0$ and $z = 0, 1$. Using $\vec{e}_x$ and $\vec{e}_z$ to denote unit vectors in the x and z directions, respectively, the Hamiltonian for the left lead reads as (see also Appendix A)

$$\begin{aligned} H_{\rm L} = \sum_{y<0} \sum_{z=0,1} & [t_0 |\vec{r}\rangle(\tau_y\sigma_y + \tau_y\sigma_z + \mu)\langle\vec{r}| \\ & + i t_y (|\vec{r}\rangle\tau_x\sigma_x\langle\vec{r} - \vec{e}_y| - |\vec{r} - \vec{e}_y\rangle\tau_x\sigma_x\langle\vec{r}|) \\ & + \delta_{z,0} t_z (|\vec{r}\rangle\langle\vec{r} + \vec{e}_z| + |\vec{r} + \vec{e}_z\rangle\langle\vec{r}|)] \end{aligned} \tag{4}$$

with lattice vector $\vec{r} = (0,y,z)$. In our calculations, we have set $t_0 = t_z = 1$ and $t_y = \frac{2}{5}$. For this choice of parameters, the lead supports four right-propagating modes and their left-propagating time-reversed partners. The coupling between the leads and the bulk sample is described by the coupling

term

$$W_{\rm L} = i\gamma t_y \sum_{z=0,1} (|\vec{r}\rangle \tau_x \sigma_x \langle \vec{r} - \vec{e}_y| - |\vec{r} - \vec{e}_y\rangle \tau_x \sigma_x \langle \vec{r}|), \quad (5)$$

with $\vec{r} = (0,0,z)$. Similar expressions apply to the Hamiltonian $H_{\rm R}$ of the right lead and the coupling $W_{\rm R}$ between the right lead and the sample. In our calculations we have chosen the value $\gamma = 5$, optimized empirically for the numerical detection of the scattering resonances.

To find the topological invariants for a disordered sample, we employ the twisted boundary conditions method [16,29]. This amounts to inserting additional phase factors $e^{i\phi_x}$ and $e^{i\phi_z}$ in the hopping matrix elements connecting sites at $x = 0$ and $L_x - 1$, and $z = 0$ and $L_z - 1$, respectively. The resulting system can be thought of as a large unit cell defined on a torus with two independent Aharonov-Bohm fluxes threading the two holes around the x and z axes. For the purpose of classifying insulating phases, it is sufficient to focus on the reflection matrix $S_y(\phi_x,\phi_z)$ of the left ($y < 0$) lead, which is a unitary matrix for an insulating sample. For our choice of parameters, the leads have four propagating modes at the Fermi energy ($\varepsilon = 0$), so that S_y is a 4×4 matrix.

To obtain topological invariants from the scattering matrix, we note that, because of time-reversal invariance, S_y satisfies the condition

$$S_y(\phi_x,\phi_z)V = -V^{\rm T} S_y^{\rm T}(-\phi_x,-\phi_z), \quad (6)$$

where T denotes the matrix transpose and the unitary matrix V describes the action of the time-reversal operator T in the space of scattering states [20]. Since T flips the sign of the velocity $v = dE/dk$, it connects incoming and outgoing modes $T\psi_n^{\rm in} = \sum_k V_{nk}\psi_k^{\rm out}$. Reference [20] chooses a convention wherein, after redefinition of the incoming scattering states, $S_y V \to S'_y$ the scattering matrix becomes antisymmetric at the "time-reversal-invariant fluxes" $\phi_{x,z} = 0,\pi$, and, thus, acquires the same symmetry properties as the matrix $w(\mathbf{k})$ used by Fu and Kane to classify time-reversal-invariant topological insulators without disorder in terms of their band structure [14]. Here, we follow the formulation of scattering theory as it is most commonly used in the theory of quantum transport [30,31], in which one makes the choice $VV^* = -1$. At the time-reversal-invariant fluxes $\phi_{x,z} = 0,\pi$ this gives the condition that S_y is "self-dual" $S_y^{\rm T} = V^{-1} S_y V$. Then Kramers degeneracy ensures that the eigenphases $\{e^{i\theta_j}\}_{j=1,\ldots,4}$ of S_y are twofold degenerate at $\phi_{x,z} = 0,\pi$. The topological classification rests on the eigenvalue evolution as one of the fluxes ϕ_x or ϕ_z changes from 0 to π, so that the system evolves from one time-reversal-invariant flux configuration into another one [23]: In the topologically trivial case, labeled by $\mathcal{Q}[S_y] = 0$, degenerate eigenvalue pairs, which generically split upon departing from a time-reversal-invariant flux, are reunited upon reaching the other time-reversal-invariant fluxes. In the nontrivial case, which we label by $\mathcal{Q}[S_y] = 1$, the eigenphases from a degenerate pair are united with eigenphases from different pairs. (If S_y is a 2×2 matrix, so that there is only a single eigenvalue pair, the question of topological triviality is connected to the winding of the eigenphase pair around the unit circle [23].) One easily verifies that this definition is independent of the choice which eigenphase pair is being "tracked": if one eigenphase pair "switches partners," then all eigenphase pairs must do so. Similar considerations have been applied to Kramers degenerate energy level pairs in order to argue for topological nontriviality of time-reversal-invariant topological insulators [14,21,32]. The strong and weak topological invariants of the sample are then defined as [20]

$$\begin{aligned}\nu_0 &= \{\mathcal{Q}[S_y(\phi_z = 0,\phi_x : 0 \to \pi)] \\ &\quad + \mathcal{Q}[S_y(\phi_z = \pi,\phi_x : 0 \to \pi)]\} \bmod 2 \\ &= \{\mathcal{Q}[S_y(\phi_x = 0,\phi_z : 0 \to \pi)] \\ &\quad + \mathcal{Q}[S_y(\phi_x = \pi,\phi_z : 0 \to \pi)]\} \bmod 2, \end{aligned} \quad (7)$$

$$\nu_x = \mathcal{Q}[S_y(\phi_x = \pi,\phi_z : 0 \to \pi)], \quad (8)$$

$$\nu_z = \mathcal{Q}[S_y(\phi_z = \pi,\phi_x : 0 \to \pi)]. \quad (9)$$

The two expressions for ν_0 are equivalent because the evolution of an eigenphase pair for a contractable loop in the ϕ_x, ϕ_z plane is always trivial. The relations (7)–(9) remain valid under circular permutation of spatial indices, so that, e.g., the weak topological index ν_y can be calculated by attaching a lead in the x or z directions.

Using the KWANT software package [33], we performed numerical calculations of ν_0 and ν_z on a system with dimensions $L_{x,z} \simeq 9$ and variable $L_y = 9 \ldots 160$. Here, the length L_y was increased until an (almost) unitary reflection matrix $S_y(\phi_x,\phi_z)$ was found, where we used the condition $||\det S_y| - 1| < 10^{-4}$ as an empirical cutoff where unitarity is reached. The possibility of large system sizes L_y is needed to accommodate cases with a long localization length, as it occurs close to a topological phase transition. If the condition $||\det S_y| - 1| < 10^{-4}$ could not be met for $L_y \leqslant 160$, the system is empirically labeled as metallic. (Note that a full assessment of the metal/insulator transition requires an analysis of the scaling behavior of conductivity, which is beyond the scope of this work.) The approach to a unitary scattering matrix is illustrated in Fig. 2, which shows the evolution of $|\det[S_y(\phi_{x,z} = 0)]|$

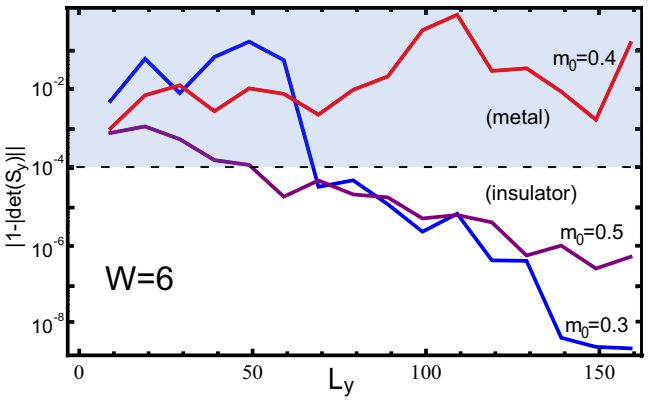

FIG. 2. (Color online) Evolution of $|\det[S_y(\phi_{x,z} = 0)]|$ as a function of L_y for $L_{x,z} = 11$ and a specific disorder realization with disorder strength $W = 6$ and $\mu = 0$. The three curves are for m_0 are 0.3, 0.4, and 0.5, corresponding to the STI phase, the immediate vicinity of the topological phase transition, and the OI phase, respectively. The dashed line indicates the empirical cutoff used in the calculations.

as a function of L_y at disorder strength $W = 6$ across the OI-STI transition for three different values of m_0. During the sweep of the flux ϕ_x and ϕ_z, the eigenphases have been tracked using a dynamical step-width control, allowing us to resolve sharp features in the eigenphase trajectory. Note that the use of twisted boundary conditions in the x and z directions allows us to chose moderate $L_{x,z}$ since we are not required to separate any surface states. We found the system size L_x, $L_z = 9$ sufficient to suppress finite-size issues: Beyond a parity effect for $L_{x,z}$ (see the discussion in the next section), there is no dependence of the results on increased $L_{x,z}$ (see Appendix B).

As an example, Fig. 1(b) shows a typical eigenphase evolution for $m_0 = -1$ and $\mu = 0$ in the clean and a disordered case ($W = 0$ and 10). For $\phi_z = 0$, a topologically nontrivial winding is obtained, while $\phi_z = \pi$ shows a trivial winding for both the clean and the disordered case. With Eqs. (7) and (9) we obtain $\nu_0 = 1$ and $\nu_z = 0$, respectively. Similarly, we confirmed $\nu_x = \nu_y = 0$ which, in summary, leads to $(\nu_0, \nu_x \nu_y \nu_z) = (1000)$ for the particular points in parameter space.

III. COMPARISON WITH BAND-STRUCTURE-BASED APPROACH

In this section, we focus on $\mu = 0$. For a clean bulk system, the topological indices ν_0 and $\nu_{x,y,z}$ can also be calculated from the band structure. The weak indices one obtains from the scattering approach agree with those for the bulk system if and only if the sample dimensions L_x, L_y, and L_z are odd. (For even sample dimension, the scattering method yields trivial weak indices.) The advantage of the scattering approach is that the weak indices can be calculated for a disordered system as well.

In order to show that the scattering-matrix-based topological indices of Eqs. (7)–(9) are the same as the band-structure-based indices if the sample dimensions are odd, we make use of the relation between scattering phases and bound (surface) states: A surface state exists at energy ε if and only if S_y for energy ε has an eigenphase π. This relation follows from the observation that capping the lead by a "hard wall," which has scattering matrix -1, restores the original surface-state spectrum without coupling to an external lead. A nontrivial winding requires that an *odd* number of eigenphases passes the reference phase π upon sweeping the fluxes ϕ_x and ϕ_z as specified in Eqs. (7)–(9), whereas an even number of eigenphases passes the reference phase π if the winding is trivial [23]. Note that depending on the definition of the lead modes, the numerical value of the reference phase might differ from π. (In Appendix A, we show that for the clean and weak coupling limit, all phase-winding signatures can be reproduced quantitatively from an analytical calculation of the scattering matrix in terms of the surface states at the $y = 0$ surface.)

In a clean system, translation invariance in the x and z directions implies that the surface states are labeled by a wave vector $\bar{\bar{q}} = (q_x, q_z)$ in the surface Brillouin zone. Possible Dirac cones in the (q_x, q_z) plane are centered around the four time-reversal-invariant momenta $(q_x, q_z) = (0,0)$, $(0,\pi)$, $(\pi,0)$, and (π,π) (see Fig. 3). For a finite-size sample with twisted boundary conditions, only discrete values $q_x = (2\pi n - \phi_x)/L_x$, $q_z = (2\pi n - \phi_z)/L_z$ are allowed. A resonance (i.e., scattering phase π) is found if one of the allowed $\bar{\bar{q}}$ vectors crosses one of the surface Dirac cones.

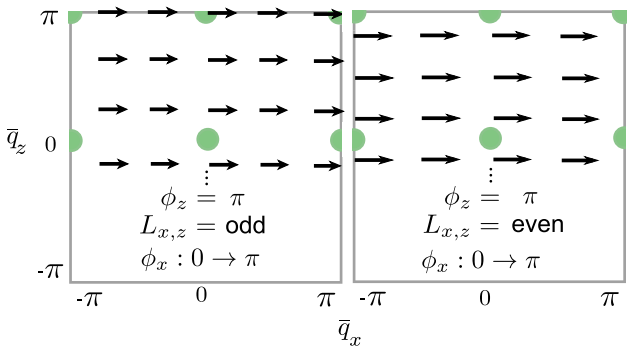

FIG. 3. (Color online) Brillouin zone for a surface orthogonal to the y direction. Black arrows indicate the trajectories of surface wave vectors $\bar{\mathbf{q}} = (q_x, q_z)$ corresponding to L_x and L_z both odd (left) or even (right) for fixed $\phi_z = \pi$ and a sweep of ϕ_x from 0 to π. Dots indicate time-reversal-invariant momenta which are possible positions for surface Dirac cones at $\mu = 0$.

For definiteness, we now consider the weak index ν_z, which is determined by the phase winding $\mathcal{Q}$ along the path $\phi_x : 0 \to \pi$ at fixed $\phi_z = \pi$. While sweeping ϕ_x, the allowed $\bar{\bar{q}}$ values build a set of trajectories in the (q_x, q_z) plane, which are shown in Fig. 3 for the cases of L_x and L_z even or odd. From inspection of Fig. 3 one immediately concludes that a Dirac cone gives rise to an odd number of scattering resonances if and only if its center is at one of the "allowed" $\bar{\bar{q}}$ vectors for $\phi_x = 0$ or for $\phi_x = \pi$, which requires odd L_z for Dirac points with $q_z = \pi$. Hence, we conclude that if and only if L_z is odd, the index ν_z of Eq. (9) measures the parity of the number of Dirac points with $q_z = \pi$. Similarly, the index ν_x of (8) measures the parity of the number of Dirac points with $q_x = \pi$ if and only if L_x is odd, whereas the index ν_0 of Eq. (7) measures the parity of the total number of Dirac points for both even and odd sample dimensions. In all three cases, the parities of number of Dirac points correspond to the very same quantities as those that are computed from the band structure [1,2,34].

There is a simple argument that shows that the scattering-matrix-based weak indices are always trivial if the sample dimensions are even, irrespective of the value of the bulk index: Any three-dimensional weak topological insulator is adiabatically connected to a stack of two-dimensional topological insulators. The stacking direction can be taken to be $G_\nu = (\nu_x, \nu_y, \nu_z)$. A "mass term" that couples these layers in pairs connects the system adiabatically to a trivial insulator [11,12,35]. If L_x, L_y, L_z are all even, such a mass term can be applied for any G_ν. Since the indices of Eqs. (8) and (9) are true topological invariants, they can not change upon inclusion of such a mass term, i.e., they can only acquire a value compatible with the topologically trivial phase.

For odd sample dimensions, this argument does not apply and, as is shown above, for the clean case, the topological indices derived from the scattering matrix agree with the indices obtained from the band structure.

IV. PHASE DIAGRAM IN THE PRESENCE OF DISORDER

We now discuss the $\mathbb{Z}_2$ phase diagram of the three-dimensional Hamiltonian H in the (m_0, W) parameter plane

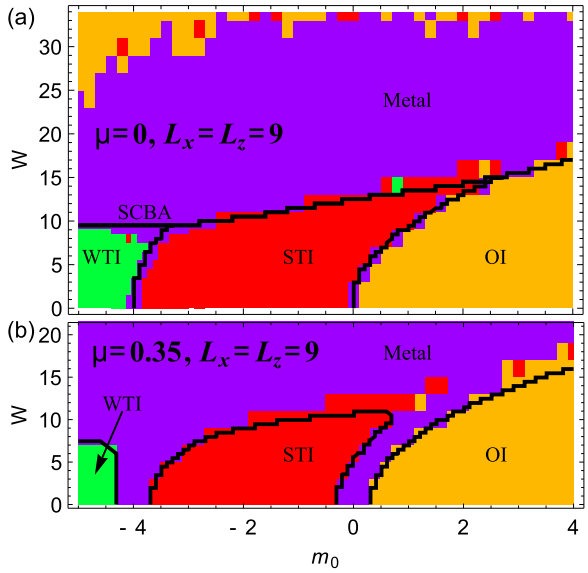

FIG. 4. (Color online) Topological phase diagram of model H as calculated with the scattering matrix method with potential disorder in the mass (m_0), disorder strength (W) plane for $\mu = 0$ (a) and $\mu = 0.35$ (b). The sample dimensions are $L_{x,z} = 9$, $L_y \leqslant 160$. Solid lines denote the SCBA phase boundaries of insulating phases with $\mathrm{Im}\Sigma = 0$.

with potential disorder. We study the cases $\mu = 0$ and $\mu = 0.35$. Topological indices ν_0 and ν_z are computed as described in Sec. II for a dense grid of parameter values. The result is shown in Fig. 4. For $\mu = 0$, it confirms similar topological phase diagrams computed on the basis of conductance and scaling methods as in Refs. [17,19]. Due to the large maximum system size of $9 \times 160 \times 9$ we relied on self-averaging and worked with only a single disorder realization per point in parameter space. The results indicate that this is indeed justified for the range of weak and moderate disorder strengths; only for the strong disorder region $W > 25$, where Anderson localization and a trivial insulator is expected, a minority of data points yields diverging results.

Studies of disorder effects of the three-dimensional quantum critical point between STI and OI at $\mu = 0$ employing the self-consistent Born approximation [3], renormalization group [36], or a numerical approach [37] show the existence of a critical disorder strength below which a direct phase transition without extended metallic phase is realized. This conclusion, however, is valid only for systems with chemical potential at the clean band-touching energy (here $\mu = 0$) which also preserve inversion symmetry (after disorder average). Indeed, our numerical results for $\mu = 0$ show that the width of the metal region at the m_0-induced transition between WTI, STI, and OI for weak disorder is considerably smaller than in other studies of the $\mathbb{Z}_2$ invariant for disordered systems [16,20], indicating that finite-size effects are much less severe for the large system sizes we can reach. Further indication for the successful suppression of finite-size effects is that the phase diagram in Fig. 4(a) remains unchanged if we increase the system volume by 50% to $11 \times 160 \times 11$ (see Appendix B).

An analytical approach to disordered topological insulators is the calculation of the disorder-averaged self-energy Σ using the self-consistent Born approximation (SCBA) [3,7]. Due to symmetry arguments, Σ can be expanded as $\Sigma_z\tau_z + \Sigma_0\tau_0$, where τ_0 is the 2×2 unit matrix, and the SCBA equation reads as [3,7]

$$\Sigma = \sum_{d=1}^{6} \frac{W_d^2}{12} \sum_{\mathbf{k}\in BZ} (\sigma\tau)_d \frac{1}{i\delta - H_0(\mathbf{k}) - \Sigma} (\sigma\tau)_d, \qquad (10)$$

where the notation $(\sigma\tau)_d$ was introduced below Eq. (3). Consequently, the disorder averaged propagator features renormalized mass and chemical potential values $\bar{m} = m_0 + \mathrm{Re}\Sigma_z$ and $\bar{\mu} = \mu - \mathrm{Re}\Sigma_0$, respectively. If $\mathrm{Im}\Sigma = 0$ and $\bar{\mu}$ in the bands above and below energies $\pm\min(|\bar{m}|, |\bar{m} + 4|)$ the system is metallic; otherwise, if $\bar{\mu}$ is in the band gap, the value of $\bar{m}$ determines the nature of the resulting insulator: For $0 < \bar{m}$ we expect an OI, $-4 < \bar{m}$ yields a WTI, and $-4 < \bar{m} < 0$ indicates a STI. Nonzero imaginary parts $\mathrm{Im}\Sigma_z$ and $\mathrm{Im}\Sigma_0$ translate into a finite lifetime $\tau < \infty$ and a finite density of states at the Fermi level, indicating either a compressible diffusive metal phase [36] or, if these states are localized, an insulator. SCBA can not distinguish between both possibilities.

The coupled set of SCBA equations (10) is numerically solved self-consistently. For potential disorder ($W_d = 0$ for $d > 1$), the resulting phase boundaries of insulating phases with $\mathrm{Im}\Sigma = 0$ are shown in Fig. 4 as solid lines. For $\mu = 0$, we find excellent agreement of the SCBA phase boundaries with the results from the scattering matrix method. Since SCBA as a disorder-averaged theory is free of finite-size effects, this further supports the applicability of the scattering matrix results in the thermodynamic limit. The situation is different for $\mu = 0.35$, where for strong disorder ($W \gtrsim 10$) the insulating states slightly but numerically significantly exceed the regions where $\mathrm{Im}\Sigma = 0$ as obtained from SCBA, indicating localized states at the Fermi energy. A similar observation was reported in Ref. [16].

In closing, we comment on the effect of the five remaining disorder types. By inspection of Eq. (10) we find that mass-type disorder $(\sigma\tau)_6 = \tau_z$ has the same effect as pure potential disorder, i.e., bending the phase boundaries between insulating phases to increased values of m_0. All other disorder types have the opposite effect on $\bar{m}$, as was noticed for the two-dimensional case in Ref. [9]. We have confirmed the agreement between scattering matrix results and the trends predicted by SCBA in these cases (results not shown). We conclude that qualitative features of the phase diagram, as, for example, the occurrence of a disorder-induced topological Anderson insulator transition, crucially rely on the microscopic details of the disorder potential.

V. CONCLUSION

We have demonstrated the potential of the scattering matrix method for the computation of $\mathbb{Z}_2$ topological indices for a three-dimensional disordered tight-binding model featuring strong and weak topological phases. We studied the $\mathbb{Z}_2$ phase diagram in the mass-disorder plane for system sizes up to $11 \times 160 \times 11$ and found excellent agreement with SCBA predictions. The latter have been studied in the literature before [3,17,36] (only for the OI/STI case and for $\mu = 0$) but have never been compared quantitatively to a real-space

disordered three-dimensional TI tight-binding model. We conclude that SCBA should have predictive value also for similar scenarios. In particular, we showed that SCBA is quantitatively correct also for finite chemical potential and weak disorder, where extended metal regions occur even for weak disorder, whenever the (renormalized) chemical potential lies within a bulk band. This possibility has been overlooked in Ref. [18]. For the insulator-metal transition at larger disorder strength, SCBA's precision suffers from its inherent inability to take into account localization effects [18] which occur at the edges of topological nontrivial bands.

The scattering matrix method can be regarded as complementary to a finite-size scaling analysis. While the latter is ideally suited to detect a phase boundary, the scattering matrix method can unambiguously identify the topological phase at each parameter point where the system is insulating. This proves the nontrivial $\mathbb{Z}_2$ nature of the topological Anderson insulator phase without referring to adiabatic connection to the clean STI phase or involving other indirect arguments. For the disordered WTI, we find no evidence for a "defeated WTI" region in the phase diagram, as suggested recently in Ref. [19]. We point out that the scattering matrix method should be an ideal tool to identify the topological invariants for (so far hypothetical) disordered topological phases that are not adiabatically connected to the clean case.

The scattering matrix method is able to find weak indices even if the strong index is nonzero, as has been checked using a modified Hamiltonian H (as in Ref. [27]) with anisotropic mass parameters which realize many more topological phases, e.g., $(\nu_0;\nu_x\nu_y\nu_z) = (1;001)$. Moreover, our results explicitly demonstrate the intricate interplay between system size and topological phase in the parameter region supporting a WTI phase. Adding a single layer to the system can change the topological phase from OI to WTI or vice versa, a behavior not reflected in conductance simulations. The case of a disordered WTI phase has been previously discussed in Refs. [38,39], where it is argued that average translational symmetry in stacking direction is sufficient to protect the weak topological insulator phase. This is in agreement with our findings since an odd number of stacked layers prohibit any average translational symmetry breaking, while such a dimerization can be adiabatically applied to an even number of layers.

ACKNOWLEDGMENTS

We thank A. Akhmerov, C. Groth, X. Waintal, and M. Wimmer for making the KWANT software package available before publication. We thank a thoughtful referee for pointing out the problem with SCBA in Ref. [18]. Financial support was granted by the Helmholtz Virtual Institute "New states of matter and their excitations" and by the Alexander von Humboldt Foundation in the framework of the Alexander von Humboldt Professorship, endowed by the Federal Ministry of Education and Research.

APPENDIX A: ANALYTIC MODELING OF THE PHASE WINDING IN THE CLEAN LIMIT

In the clean case, it is possible to understand the scattering matrix eigenvalue phase-winding signatures (and thus the topological classification) from a microscopic point of view. We employ the Fisher-Lee relation [40] to calculate the elements of the scattering matrix from the retarded Green's function G^R:

$$S_{nm} = -\frac{\sqrt{v_n}}{\sqrt{v_m}} 1_{nm} + i\sqrt{v_m}\sqrt{v_n} G^R_{nm}, \tag{A1}$$

where the right-hand side represents the current in outgoing lead mode n after a normalized local excitation of incoming mode m. The mode velocities v_n and v_m link this quantity to the usual amplitude propagation described by G^R and any direct transition into outgoing modes ($\propto 1_{nm}$, not contributing to the system's scattering matrix) is subtracted. The Green's function depends on the scattering region (i.e., the topological insulator surface), the lead, and their mutual coupling. We first discuss the effective description of the topological insulator surface and specify a simplified lead $H'_{\rm L}$. We then compare the analytical prediction with the full-scale numerical calculation. Finally we motivate the lead choice in the main text $H_{\rm L}$.

1. Surface states and surface Hamiltonian

Following the convention of the main text, we consider a clean topological insulator described by Eq. (1), occupying the half space $y \geqslant 0$. We make the same parameter choice as described in Sec. II. For energies in the bulk gap, a description in terms of the effective surface theory is sufficient. The Bloch wave functions for the surface states at surface momentum $\bar{\mathbf{q}} = (q_x, q_z)$ close to a Dirac point at momentum $\bar{\mathbf{Q}} = (Q_x, Q_y)$ can be found using the method applied in Ref. [35]. For the STI ($-4 < m_0 < 0$), the two surface states around the single Dirac point at $\bar{\mathbf{Q}} = (0,0)$ read as

$$\psi^{(1)}_{\bar{\mathbf{q}}}(x,y,z) = \frac{1}{\sqrt{L_x L_z}} e^{i\bar{\bar{q}}\cdot\bar{\bar{r}}} \begin{pmatrix} 1/\sqrt{2} \\ 0 \\ 0 \\ 1/\sqrt{2} \end{pmatrix} \varphi(y), \tag{A2}$$

$$\psi^{(2)}_{\bar{\mathbf{q}}}(x,y,z) = \frac{1}{\sqrt{L_x L_z}} e^{i\bar{\bar{q}}\cdot\bar{\bar{r}}} \begin{pmatrix} 0 \\ -1/\sqrt{2} \\ 1/\sqrt{2} \\ 0 \end{pmatrix} \varphi(y), \tag{A3}$$

in the same basis as Eq. (1) and with $\varphi(y)$ a normalized, decaying function for $y \to \infty$ [35]. In the basis of these two Bloch states, the effective surface Hamiltonian becomes a 2×2 matrix which reads as

$$\bar{H}^{\rm STI}_y(\bar{\bar{q}}) = A \begin{pmatrix} q_x & -q_z \\ -q_z & -q_x \end{pmatrix}. \tag{A4}$$

The constant A was defined in Eq. (1).

For the WTI ($m_0 < -4$) there are four surface bands, which form two Dirac cones centered around $\bar{\mathbf{Q}}_1 = (\pi,0)$ and $\bar{\mathbf{Q}}_2 = (0,\pi)$. The basis states are the same as in Eqs. (A2) and (A3), but with surface momenta $\bar{\mathbf{q}}_j = (q_{j,x}, q_{j,z})$ defined around $\bar{\mathbf{Q}}_j$

for $j = 1,2$, respectively. We find

$$\bar{H}_y^{\mathrm{WTI}}(\bar{\bar{q}}_1,\bar{\bar{q}}_2) = A \begin{pmatrix} -q_{1,x} & -q_{1,z} & & 0 \\ -q_{1,z} & q_{1,x} & & \\ & & q_{2,x} & q_{2,z} \\ 0 & & q_{2,z} & -q_{2,x} \end{pmatrix}. \tag{A5}$$

In a system with finite $L_{x,z}$ and given fluxes $\phi_{x,z}$, a finite subset of surface wave vectors are compatible with the twisted boundary conditions (see the discussion in Sec. III). During the sweep of the "flux" ϕ_x or ϕ_z, the allowed $\bar{\bar{q}}$ values form a set of trajectories in the surface Brillouin zone (see Fig. 3). For an approximate description of the scattering process, it is sufficient to further restrict the effective surface Hamiltonian to the few allowed wave vectors on trajectories which are closest to the Dirac points. As we will show momentarily, the arrangement of the trajectories in the surface Brillouin zone relative to the locations of the gapless points then determines the phase-winding structure.

2. Lead and its self-energy

The leads are modeled as semi-infinite, translational- and time-reversal-invariant tight-binding systems. To motivate the special choice of lead H_{L} described by Eq. (4), we first consider a simpler (thinner) lead as in Fig. 5(a), realized as a tight-binding chain of lattice sites at coordinates $|\vec{r}\rangle = (0,y,0)$, with $y < 0$ and Hamiltonian

$$H'_{\mathrm{L}} = \sum_{y<0} |\vec{r}\rangle H_{\mathrm{hop}}^{\dagger} \langle \vec{r} - \vec{e}_y| + |\vec{r} - \vec{e}_y\rangle H_{\mathrm{hop}} \langle \vec{r}|, \tag{A6}$$

where $H_{\mathrm{hop}} = t_y[\tau_y\sigma_x - i\tau_x\sigma_y]$. The wave functions of the four scattering channels at the four Fermi points $q_y = \pm\pi/4$ and $q_y = \pm 3\pi/4$ are denoted $|\phi_n^{\mathrm{in/out}}\rangle$, with $n = 1,2,3,4$. They are chosen such that the matrix V, defined below Eq. (6), fulfills the condition $V \cdot V^* = -1$. Finally, the lead H'_{L} is coupled to the system H_{S} (i.e., the topological insulator) by H_{hop} times a real constant γ,

$$W'_{\mathrm{L}} = \gamma\, [|\vec{r}\rangle H_{\mathrm{hop}}^{\dagger} \langle \vec{r} - \vec{e}_y| + |\vec{r} - \vec{e}_y\rangle H_{\mathrm{hop}} \langle \vec{r}|] \tag{A7}$$

for $\vec{r} = (0,0,0)$.

For a semi-infinite lead, the retarded Green's function G^R is an infinite-dimensional matrix. However, employing the concept of lead self-energy [41], the degrees of freedom corresponding to the lead can be eliminated. The calculation of the Green's function G^R_{nm} in Eq. (A1) is most efficient if we retain the lead site $y = -1$. Thus, the lead self-energy should take into account only lead sites $y < -1$. It reads as [41] $\Sigma'_{\mathrm{L}} = H_{\mathrm{hop}}^{\dagger} G'_{\mathrm{L}} H_{\mathrm{hop}} = -it\sqrt{2}$ where G'_{L} is the Green's function of the lead without the coupling W'_{L}. Finally, at zero energy we have $G^R = (-H_{\mathrm{S}} - W'_{\mathrm{L}} - \Sigma'_{\mathrm{L}})^{-1}$ and

$$G^R_{nm} = \left\langle \phi_n^{\mathrm{out}}(y=-1) \right| G^R \left| \phi_m^{\mathrm{in}}(y=-1) \right\rangle, \tag{A8}$$

where $|\phi_m^{\mathrm{in}}\rangle$ and $|\phi_m^{\mathrm{out}}\rangle$ are incoming and outgoing scattering states for the lead terminated at $y = -1$, i.e., without the coupling W'_{L}.

3. STI phase

As a first specific example, we consider the case of a strong topological insulator, for which the surface Hamiltonian has a single Dirac cone centered at $\bar{\bar{Q}} = (0,0)$. We chose $m_0 = -2$ since then $\varphi(y) = \delta_{y,0}$ (see Ref. [35]). Employing the boundary conditions for, say, $\phi_z = 0$ and $L_{x,z}$ odd, the resulting trajectories for the surface momenta are shown in Fig. 6 (inset). For the effective low-energy theory (encircled region in the surface Brillouin zone) we find from Eq. (A4)

$$\bar{H}_y^{\mathrm{STI}}(\phi_x) = A \begin{pmatrix} \phi_x/L_x & 0 \\ 0 & -\phi_x/L_x \end{pmatrix}. \tag{A9}$$

In order to calculate the Green's function G^R, we assume weak system-lead coupling γ. Then, H_{S} can be approximated by the ideal effective surface theory without lead [Eq. (A9)], and we

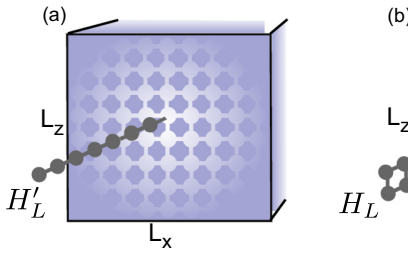

FIG. 5. (Color online) Tight-binding realization of system with Hamiltonian H with attached lead realized as a translation-invariant chain. In (a), the height of the lead, described by Hamiltonian H'_{L}, is a single lattice site while the lead H_{L} in (b) has a height of two lattice sites.

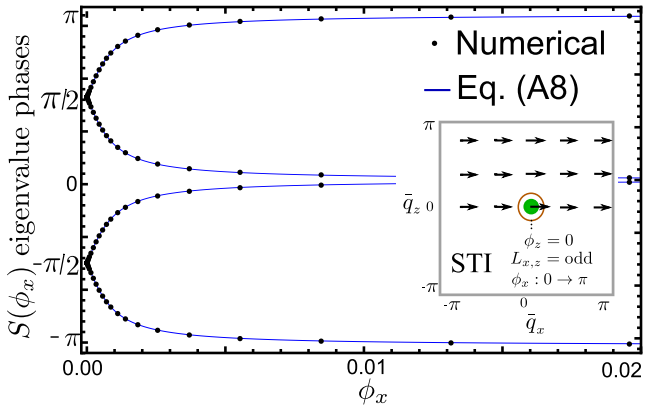

FIG. 6. (Color online) Scattering matrix eigenvalue phase windings in the case $m_0 = -2$ (STI), $\phi_z = 0$ with lead as in Eq. (A6), and $L_{x,y,z} = 9$ in the weak coupling regime ($\gamma = 0.1$, $t_y = 1$). The remaining parameters are as in the main text. Dots indicate numerical results based on the full-scale three-dimensional model, while solid lines denote analytical results based on Eq. (A10). The inset shows the surface Brillouin zone with the position of the Dirac cone for a STI and trajectories of allowed surface momenta for the boundary conditions indicated. The encircled region of the surface Brillouin zone gives rise to the effective model in Eq. (A9).

find in the basis of Eqs. (A9) and (A6)

$$(G^R)^{-1} = \begin{pmatrix} \frac{A}{L_x}\phi_x & 0 & \frac{(i-1)\gamma}{\sqrt{2}L_xL_z} & 0 & 0 & \frac{(1-i)\gamma}{\sqrt{2}L_xL_z} \\ 0 & \frac{-A}{L_x}\phi_x & 0 & \frac{-(1+i)\gamma}{\sqrt{2}L_xL_z} & \frac{-(1+i)\gamma}{\sqrt{2}L_xL_z} & 0 \\ \frac{-(1+i)\gamma}{\sqrt{2}L_xL_z} & 0 & -i\sqrt{2}t_y & 0 & 0 & 0 \\ 0 & \frac{(i-1)\gamma}{\sqrt{2}L_xL_z} & 0 & -i\sqrt{2}t_y & 0 & 0 \\ 0 & \frac{(i-1)\gamma}{\sqrt{2}L_xL_z} & 0 & 0 & -i\sqrt{2}t_y & 0 \\ \frac{(1+i)\gamma}{\sqrt{2}L_xL_z} & 0 & 0 & 0 & 0 & -i\sqrt{2}t_y \end{pmatrix}.$$

Finally, Eq. (A1) yields

$$S = \begin{pmatrix} \frac{1}{i+\Phi} & 0 & \frac{\Phi}{i+\Phi} & 0 \\ 0 & \frac{1}{i-\Phi} & 0 & \frac{\Phi}{-i+\Phi} \\ \frac{\Phi}{i+\Phi} & 0 & -\frac{1}{i+\Phi} & 0 \\ 0 & \frac{\Phi}{-i+\Phi} & 0 & \frac{1}{-i+\Phi} \end{pmatrix}, \qquad \text{(A10)}$$

where $\Phi = \frac{t_y A L_z \phi_x}{\sqrt{2}|\gamma|^2}$. The resulting eigenvalue phase winding is compared to the full-scale numerical calculation in Fig. 6, the excellent agreement between both curves quantitatively confirms the model leading to Eq. (A10). For larger coupling strength γ [i.e., $\gamma = 5$ as used in the numerics for Figs. 1(b) and 4], the assumption $H_S \simeq \bar{H}_y^{\rm STI}$ becomes invalid as surface states strongly hybridize with the lead and can no longer be labeled with surface momenta. Accordingly, Eq. (A10) then deviates from the full numerical solution.

The phase winding shown in Fig. 6 (STI, $\phi_x : 0 \to \pi$ and $\phi_z = 0$) is nontrivial. In a similar fashion, all other phase windings in the absence of disorder can be modeled using the effective low-energy and agree with the KWANT results. In general, a surface momentum trajectory that leaves or enters an odd number of surface Dirac points corresponds to a nontrivial phase winding. In the following, as we discuss the only case where two Dirac points are reached for the same flux configuration, we show why we prefer using the extended lead H_L [Eq. (4)] instead of the strictly one-dimensional lead H_L' [Eq. (A6)].

4. Motivation for an extended lead

Consider the situation $m_0 < -4$ and even system dimensions. For $\phi_z = 0$ and $\phi_x : 0 \to \pi$ the trajectories of surface momenta simultaneously leave the two Dirac cones at $\bar{\mathbf{Q}}_{1,2} = (0,\pi)$ and $(\pi,0)$, respectively. The effective surface Hamiltonian is

$$\bar{H}_y^{\rm WTI}(\phi_x) = 2\begin{pmatrix} -\phi_x & 0 & & \\ 0 & \phi_x & & \\ & & \phi_x & 0 \\ & & 0 & -\phi_x \end{pmatrix} \qquad \text{(A11)}$$

with basis states in Eqs. (A2) and (A3) for $\bar{\bar{q}}_j \simeq \bar{\bar{Q}}_j$, $j = 1,2$. Now consider a lead which is weakly coupled to just a single site at the surface of the system, say at $\bar{\bar{r}} = (0,0)$, and calculate the Green's function $G^R = (-\bar{H}_y^{\rm WTI} - W_L' - \Sigma_L')^{-1}$. Crucially, the coupling matrix elements (denoted by Γ' in the following) for the two different surface Dirac cones $j = 1,2$ are identical in such a situation since they fail to resolve the different in-plane momenta of the surface states. Representing the 2×2 blocks of Eq. (A11) by $\pm h$, we obtain generically

$$G^R = \begin{pmatrix} -h & 0 & -\Gamma' \\ 0 & h & -\Gamma' \\ -\Gamma'^\dagger & -\Gamma'^\dagger & -\Sigma_L' \end{pmatrix}^{-1}, \qquad \text{(A12)}$$

where (after matrix inversion) the relevant onsite part at $y = -1$ is just $-1/\Sigma_L$, leading to a scattering matrix independent of ϕ_x. This trivial phase winding is consistent with the discussion in Sec. III. However, any small perturbation that acts differently on the two Dirac cones invalidates the exact cancellations and causes a steep but still trivial phase winding that is increasingly harder to track for a decreasing perturbation strength. In numerical practice, finite precision of the arithmetics plays the role of a tiny perturbation which prevents proper eigenvalue phase tracking. Although even a

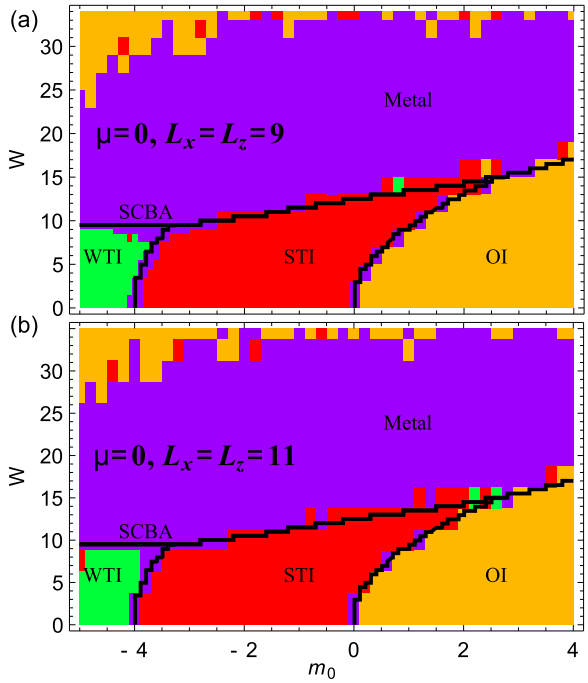

FIG. 7. (Color online) Comparison of topological phase diagrams for (a) $L_{x,z} = 9$ and (b) $L_{x,z} = 11$ which show excellent agreement. For the larger system, the resolution in parameter space is reduced. SCBA phase boundaries are included to facilitate comparison.

small amount of disorder ($W = 0.1$) is a sufficiently strong perturbation to overcome the problem, an improved lead and lead-system coupling than can distinguish between the two surface Dirac cone basis states are desirable.

A lead which is extended in, say, the z direction [see Fig. 5(b)] can carry modes that probe the different in-plane momenta of surface states. Such a lead is realized by our default choice H_L in Eq. (4). The modes are proportional to e^{i0z} or $e^{i\pi z}$ and are thus mutually orthogonal to the the surface modes if these belong to Dirac cones with $Q_z = 0$ or π. Thus, the scattering scenario described in this section becomes an effective double copy of the scenario in Sec. A 3. Now, the steepness of the (double) phase winding is conveniently controlled by γ, which justifies the increased numerical cost due to the doubling of scattering channels.

APPENDIX B: FINITE-SIZE EFFECTS

Figure 7 proves the successful suppression of finite-size effects for the system dimensions reached in this work. The phase diagram of Sec. IV remains unchanged if we increase $L_{x,z}$ from 9 to 11 (and thus the volume by 50%).

[1] M. Z. Hasan and C. L. Kane, Rev. Mod. Phys. **82**, 3045 (2010).
[2] B. A. Bernevig, *Topological Insulators and Topological Superconductors* (Princeton University Press, Princeton, NJ, 2013).
[3] R. Shindou and S. Murakami, Phys. Rev. B **79**, 045321 (2009).
[4] J. Li, R.-L. Chu, J. K. Jain, and S.-Q. Shen, Phys. Rev. Lett. **102**, 136806 (2009).
[5] H. Jiang, L. Wang, Q. F. Sun, and X. C. Xie, Phys. Rev. B **80**, 165316 (2009).
[6] C. W. Groth, M. Wimmer, A. R. Akhmerov, J. Tworzydlo, and C. W. J. Beenakker, Phys. Rev. Lett. **103**, 196805 (2009).
[7] H.-M. Guo, G. Rosenberg, G. Refael, and M. Franz, Phys. Rev. Lett. **105**, 216601 (2010).
[8] H.-M. Guo, Phys. Rev. B **82**, 115122 (2010).
[9] J. Song, H. Liu, H. Jiang, Q.-F. Sun, and X. C. Xie, Phys. Rev. B **85**, 195125 (2012).
[10] A. Girschik, F. Libisch, and S. Rotter, Phys. Rev. B **88**, 014201 (2013).
[11] Z. Ringel, Y. E. Kraus, and A. Stern, Phys. Rev. B **86**, 045102 (2012).
[12] R. S. K. Mong, J. H. Bardarson, and J. E. Moore, Phys. Rev. Lett. **108**, 076804 (2012).
[13] H. Obuse, S. Ryu, A. Furusaki, and C. Mudry, arXiv:1310.1534.
[14] L. Fu and C. L. Kane, Phys. Rev. B **76**, 045302 (2007).
[15] M. B. Hastings and T. A. Loring, Ann. Phys. (NY) **326**, 1699 (2010).
[16] B. Leung and E. Prodan, Phys. Rev. B **85**, 205136 (2012).
[17] S. Ryu and K. Nomura, Phys. Rev. B **85**, 155138 (2012).
[18] A. Yamakage, K. Nomura, K.-I. Imura, and Y. Kuramoto, Phys. Rev. B **87**, 205141 (2013).
[19] K. Kobayashi, T. Ohtsuki, and K.-I. Imura, Phys. Rev. Lett. **110**, 236803 (2013).
[20] I. C. Fulga, F. Hassler, and A. R. Akhmerov, Phys. Rev. B **85**, 165409 (2012).
[21] L. Fu and C. L. Kane, Phys. Rev. B **74**, 195312 (2006).
[22] D. Meidan, T. Micklitz, and P. W. Brouwer, Phys. Rev. B **82**, 161303 (2010).
[23] D. Meidan, T. Micklitz, and P. W. Brouwer, Phys. Rev. B **84**, 195410 (2011).
[24] R. B. Laughlin, Phys. Rev. B **23**, 5632 (1981).
[25] H. Zhang *et al.*, Nat. Phys. **5**, 438 (2009).
[26] C. X. Liu, X. L. Qi, H. J. Zhang, X. Dai, Z. Fang, and S. C. Zhang, Phys. Rev. B **82**, 045122 (2010).
[27] K.-I. Imura, M. Okamoto, Y. Yoshimura, Y. Takane, and T. Ohtsuki, Phys. Rev. B **86**, 245436 (2012).
[28] S. Murakami, New J. Phys. **9**, 356 (2007).
[29] Q. Niu, D. J. Thouless, and Y. S. Wu, Phys. Rev. B **31**, 3372 (1985).
[30] C. Beenakker, Rev. Mod. Phys. **69**, 731 (1997).
[31] Y. Nazarov and Y. V. Blanter, *Theory of Quantum Transport* (Cambridge University Press, Cambridge, UK, 2009).
[32] K. Nomura, M. Koshino, and S. Ryu, Phys. Rev. Lett. **99**, 146806 (2007).
[33] C. W. Groth, M. Wimmer, A. R. Akhmerov, and X. Waintal, arXiv:1309.2926.
[34] L. Fu, C. L. Kane, and E. J. Mele, Phys. Rev. Lett. **98**, 106803 (2007).
[35] C.-X. Liu, X.-L. Qi, and S.-C. Zhang, Physica E (Amsterdam) **44**, 906 (2012).
[36] P. Goswami and S. Chakravarty, Phys. Rev. Lett. **107**, 196803 (2011).
[37] K. Kobayashi, T. Ohtsuki, K.-I. Imura, and I. F. Herbut, Phys. Rev. Lett. **112**, 016402 (2014).
[38] L. Fu and C. L. Kane, Phys. Rev. Lett. **109**, 246605 (2012).
[39] I. C. Fulga, B. van Heck, J. M. Edge, and A. R. Akhmerov, arXiv:1212.6191.
[40] D. S. Fisher and P. A. Lee, Phys. Rev. B **23**, 6851 (1981).
[41] S. Datta, *Electronic Transport in Mesoscopic Systems* (Cambridge University Press, Cambridge, UK, 1997).

2.2 The weak side of strong topological insulators

Dislocation lines are a special form of disorder in crystal lattices. Such imperfections play a crucial role in material science and have major technological implications as they can affect the yield strength of materials. In the case of topological insulators, it turned out that dislocations dramatically affect the local electronic properties. Ran and coworkers formulated a condition under which topologically protected helical zero modes propagate along dislocation lines [48]. The topological nature of such electronic states is an important distinction from impurity or dislocation line states in non-topological materials, which in principle can be gapped out and are not protected from localization.

In a strong topological insulator slab, the topological surface states are a direct consequence of non-trivial bulk topological invariants, their protection rests on the presence of a robust energy gap in the bulk material separating these surface states. These very same properties - topological invariants of bulk band structures - however ensure the presence of robust dislocation line modes that should consequently be able to couple distant surface states directly. Below we explore the rich implications of this dichotomy. Before we present a scattering matrix approach to this problem in the paper titled *"The weak side of strong topological insulators",* DOI: 10.1103/PhysRevB.93.161105, we turn to the understanding of the origin of these peculiar electronic states bound to dislocation lines. We follow the exposition in reference [48].

Dislocation line zero modes from weak topological indices A dislocation is a one dimensional extended object characterized by its Burgers vector $\mathbf{B}$ that accounts for the extra lattice vector required to close a loop of primitive lattice vectors that was opened by the insertion of a dislocation line, see Figure 2.2. For screw dislocations, $\mathbf{B}$ is parallel to the dislocation line, in edge dislocations, it is perpendicular.

We prove a condition for the presence of one dimensional helical zero modes bound to dislocation lines in a three-dimensional topological insulator with weak topological indices $\boldsymbol{\nu} = (\nu_1, \nu_2, \nu_3)$. It only depends on the Burgers vector's projection to the vector

$$\mathbf{M}_\nu = \frac{1}{2}(\nu_1 \mathbf{G}_1 + \nu_2 \mathbf{G}_2 + \nu_3 \mathbf{G}_3) \tag{2.10}$$

where $\mathbf{G}_{1,2,3}$ are the three reciprocal lattice vectors. The condition for the presence of topological zero modes reads

$$\mathbf{M}_\nu \cdot \mathbf{B} = \pi \,(\mathrm{mod}\, 2\pi) \tag{2.11}$$

and does notably *not* depend on the strong index ν_0. We next turn to a proof of this condition.

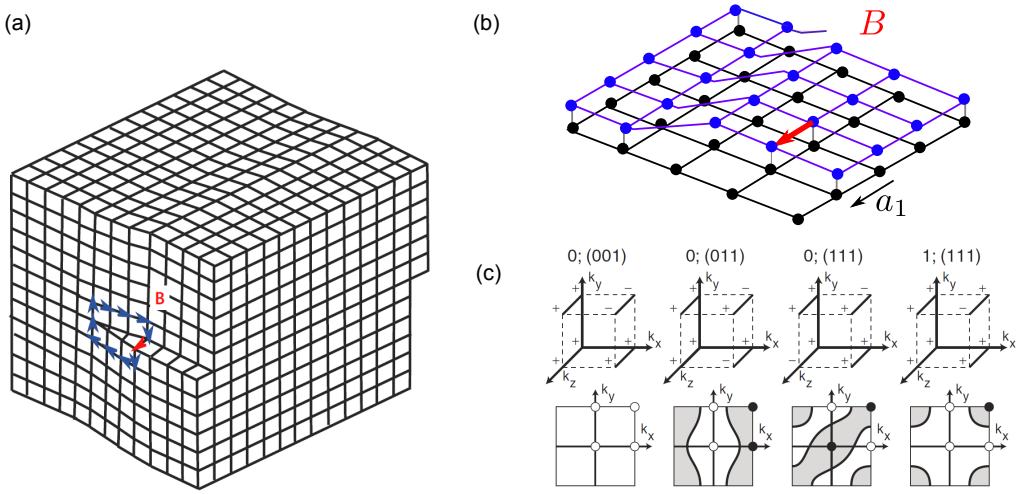

Figure 2.2: (a) Screw dislocation in a three-dimensional cubic lattice with Burgers vector $\mathbf{B}$, aligned in parallel with the dislocation line. (From reference [48].) (b) Schematic lattice configuration in the two crystal planes below and above the dislocation line. (c) Examples for the relation of the topological invariants $\nu_0, \boldsymbol{\nu}$ (top row) to the quantities $\delta_{\mathbf{m}}$ defined at time-reversal invariant momenta $\mathbf{m}$ in the bulk Brillouin zone (middle row) and to the surface state structure on the 001 - surface (bottom row). (From reference [18].)

Proof of the condition $\mathbf{M}_\nu \cdot \mathbf{B} = \pi \,(\mathrm{mod}\, 2\pi)$ We start the argument with a review of the definition of the vector $\boldsymbol{\nu}$ and its consequence for the form of surface states [18]. The quantities $\delta_{\mathbf{m}}$ introduced in chapter 1 are defined at eight time-reversal invariant momenta (TRIM) in the Brillouin zone,

$$\mathbf{m}_{n_1,n_2,n_3} = \frac{1}{2}(n_1\mathbf{G}_1 + n_2\mathbf{G}_2 + n_3\mathbf{G}_3) \tag{2.12}$$

with $n_i \in \{0,1\}$. For two neighboring TRIMs in the surface Brillouin zone of the, say, 001 - surface, $\bar{\mathbf{m}}_{a,b}$ (with $n_3 \equiv 0$), the parity of Fermi level crossings along their connection N_{cross} is given by

$$(-1)^{N_{cross}} = \delta_{\bar{\mathbf{m}}_a}\delta_{\bar{\mathbf{m}}_a+\mathbf{G}_3/2} \cdot \delta_{\bar{\mathbf{m}}_b}\delta_{\bar{\mathbf{m}}_b+\mathbf{G}_3/2}, \tag{2.13}$$

which is a gauge invariant quantity and various configurations are exemplified in Figure 2.2(c). Moreover, it can be shown that there exists a convenient gauge choice such that there is at most one nontrivial δ in the set of the seven δ with

nonzero TRIM $\mathbf{m}_{n_1,n_2,n_3}$. If such a δ exists, it must occur at momentum $\mathbf{m} = \mathbf{M}_\nu$. The value of δ_0 at the origin then controls the value of the strong index ν_0. In summary, a weak topological insulator has $\delta_{\mathbf{M}_\nu} = -1$ and $\delta_0 = -1$ and a strong topological insulator has $\delta_{\mathbf{M}_\nu} = -1$ as the only nontrivial δ.

We now specialize to a screw dislocation that is generated by sliding the top front part of the lattice plane stack in Figure 2.2(a) to the right by $|\mathbf{B}|$, where $\mathbf{B}$ is the Burgers vector, see also (b) for a detailed view of the two lattice planes closest to the dislocation line. Consider cutting the crystal bonds between the blue and the black planes before the sliding takes place. The exposed surfaces have an electronic structure that is either fully gapped or can be adiabatically deformed to harbor Dirac cone dispersions placed at zero, one or two surface TRIMS. In the case of a single Dirac cone at a time-reversal invariant surface momentum $\bar{\mathbf{m}}_D$ the Hamiltonian of top and bottom surface reads

$$H\left(\bar{\mathbf{k}}\right) = \left[\bar{\mathbf{k}}_x \sigma_x + \bar{\mathbf{k}}_y \sigma_y\right] \tau_z$$

where the Pauli matrix τ_z labels top and bottom surface and the surface momentum $\bar{\mathbf{k}}$ is measured relative to $\bar{\mathbf{m}}_D$. Sliding the top front part of the upper portion of the crystal and reconnecting the surface bonds, the coupling between the two layers depends on the overlap of local wavefunctions at surface position $\bar{\mathbf{r}}$, for the bottom surface and the top surface in the non-shifted area, the wavefunctions can written as $\psi\left(\bar{\mathbf{r}}\right) \propto e^{i\bar{\mathbf{m}}_D \cdot \bar{\mathbf{r}}} \phi\left(\bar{\mathbf{r}}\right)$ where ϕ is a slowly varying function of $\bar{\mathbf{r}}$. In contrast, for the top surface in the shifted area $\tilde{\psi}\left(\bar{\mathbf{r}}\right) \propto e^{i\bar{\mathbf{m}}_D \cdot (\bar{\mathbf{r}} - \mathbf{B})} \tilde{\phi}\left(\bar{\mathbf{r}}\right)$ where again $\tilde{\phi}$ is slowly varying. In summary, the total Hamiltonian of the reconnected, partially shifted surfaces can be written

$$H = \left[\bar{\mathbf{k}}_x \sigma_x + \left(-i\hbar\partial_y\right) \sigma_y\right] \tau_z + m\left(x_2\right) \tau_x \tag{2.14}$$

where we used that translational symmetry is preserved along x-direction. The coupling amplitude $m(x_2 < 0) = m$ and $m(x_2 > 0) = e^{i\bar{\mathbf{m}}_D \cdot \mathbf{B}} m$ takes into account a possible phase shift of the hopping matrix element as the coordinate x_2 traverses the dislocation line (placed at $x_2 = 0$). In the case $\bar{\mathbf{m}}_D \cdot \mathbf{B} = \pi \left(\mathrm{mod}\, 2\pi\right)$, Equation 2.14 gives rise to a Kramers pair of domain wall fermions [49] with linear dispersion inherited from the $\bar{\mathbf{k}}_x \sigma_x$ part.

This derivation can be repeated for more than one Dirac cone surface state, each of which possibly yields a domain wall fermion while only an odd number of the latter are protected from gapping out. Candidate positions of surface Dirac nodes $\bar{\mathbf{m}}_D$ that produce domain wall fermions for our (generic) choice of $\mathbf{B} = \mathbf{a}_1$ are $\bar{\mathbf{m}}_D = \mathbf{G}_1/2$ and $\bar{\mathbf{m}}_D = (\mathbf{G}_1 + \mathbf{G}_2)/2$. However, the parity of Dirac cones at these points in the surface Brillouin zone can be computed from the Fermi level crossings

in between, according to Equation 2.13

$$(-1)^{N_{cross}} = \delta_{\mathbf{G}_1/2}\delta_{(\mathbf{G}_1+\mathbf{G}_3)/2} \cdot \delta_{(\mathbf{G}_1+\mathbf{G}_2)/2}\delta_{(\mathbf{G}_1+\mathbf{G}_2+\mathbf{G}_3)/2}.$$

The condition for the four TRIM appearing as labels on the right-hand side of the above equation is $\mathbf{m} \cdot \mathbf{B} = \pi$. In the gauge choice with at most one non-trivial δ at non-zero TRIM $\mathbf{M}_\nu$, the above condition of $N_{cross} = 1$ is thus satisfied if $\mathbf{M}_\nu \cdot \mathbf{B} = \pi$.

Note that the above derivation can be generalized for Burgers vectors equal to a multiple of a primitive lattice vector. In the case of an odd multiple, the derivation holds as above, for an even multiple the phase shift $e^{i\tilde{\mathbf{m}}_D \cdot \mathbf{B}}$ is always trivial and no zero modes result. All these cases are captured by Equation 2.11.

The Burgers vector $\mathbf{B}$ is constant along the full extent of the dislocation line. The direction of the dislocation line may however change as it propagates through the lattice, giving rise to mixed dislocation of screw- and edge type. In the former, $\mathbf{B}$ is parallel to the local tangent to the dislocation line, in the latter it is perpendicular. Since a topological zero mode established along a screw dislocation by the above arguments and protected by a bulk band gap and time-reversal symmetry cannot simply terminate inside the crystal, it will also be present after the dislocation line changed direction and continues as an edge type dislocation. This generalizes the above proof also for edge type dislocations.

PHYSICAL REVIEW B **93**, 161105(R) (2016)

Weak side of strong topological insulators

Björn Sbierski, Martin Schneider, and Piet W. Brouwer
Dahlem Center for Complex Quantum Systems and Fachbereich Physik, Freie Universität Berlin, 14195 Berlin, Germany
(Received 10 February 2016; published 11 April 2016)

Strong topological insulators may have nonzero weak indices. The nonzero weak indices allow for the existence of topologically protected helical states along line defects of the lattice. If the lattice admits line defects that connect opposite surfaces of a slab of such a "weak-and-strong" topological insulator, these states effectively connect the surface states at opposite surfaces. Depending on the phases accumulated along the dislocation lines, this connection results in a suppression of in-plane transport and the opening of a spectral gap or in an enhanced density of states and an increased conductivity.

DOI: 10.1103/PhysRevB.93.161105

Introduction. Band insulators come in topologically distinct classes, where the topologically nontrivial classes have extended surface states, which are robust to small deformations of the Hamiltonian [1–6]. The topological classification of generic band insulators in three dimensions distinguishes "strong" and "weak" topological indices [5,7]. A nonzero value of the strong index signifies a "strong topological insulator;" Surface states of strong insulators have a spectrum with an odd number of Dirac cones, and they are robust to disorder or other perturbations that break the lattice translation symmetry. In a "weak topological insulator," i.e., if the strong invariant is trivial and the weak invariant is nontrivial, the lattice translation symmetry is essential for the protection of the surface states, although, as was pointed out in a seminal article by Ringel *et al.* [8], the surface states of a weak topological insulator show a remarkable robustness in the presence of perturbations that preserve the lattice translation symmetry on the average [9,10].

An important property of insulators with nontrivial weak indices is that a line dislocation may have topologically protected helical states, similar to the helical edge states of a two-dimensional topological insulator [11,12]. The precise conditions for the existence of such strongly protected states depends on the Burgers vector $\mathbf{b}$ of the dislocation [12,13]. The helical states along the dislocation line remain topologically protected as long as the notion of a separate dislocation with a well-defined Burgers vector remains valid. The presence of nonzero weak and strong indices is not mutually exclusive, and it is possible that a band insulator is at the same time a weak topological insulator *and* a strong topological insulator. Such a scenario is expected to be relevant, e.g., for BiSb compounds or for the putative Kondo topological insulator SmB_6 [14]. In principle, such a "weak-and-strong topological insulator" combines an odd number of Dirac cones in the surface-state spectrum with topologically protected helical states along lattice defects.

Realistic topological insulators are often layered materials, and flakes of such materials are usually investigated in a quasi-two-dimensional slab geometry, in which the slab thickness is large enough that surface states at the bottom and top surfaces remain well separated. The presence of dislocation lines that connect the top and bottom surfaces of a weak-and-strong topological insulator, as shown schematically in Fig. 1(a), may, however, provide a mechanism by which the two surfaces are coupled nevertheless. As we show here, a finite density of dislocation lines may lead to the opening of a gap in the surface-state spectrum of a slab and to a strong suppression of electron transport parallel to the surface, although the precise scenario depends on the phase that electrons accumulate along the dislocation line. The possibility of a coupling of surface states at bottom and top surfaces via dislocation lines presents a "weak side" of topological insulators with nontrivial strong and weak indices; it does not exist for strong topological insulators with trivial weak indices, for which dislocation lines do not carry protected helical states. We now proceed with a description of our results.

Description of dislocation line defect in terms of a π-flux line. The weak indices $\nu_j = 0,1$, $j = 1,2,3$, of a topological insulator are defined with respect to a basis $(\mathbf{G}_1,\mathbf{G}_2,\mathbf{G}_3)$ of reciprocal lattice vectors. Together they uniquely define a reciprocal lattice vector $\mathbf{M} = (1/2)(\nu_1\mathbf{G}_1 + \nu_2\mathbf{G}_2 + \nu_3\mathbf{G}_3)$ [12]. As shown by Ran, Zhang, and Vishwanath, a lattice dislocation binds an odd number of helical modes if and only if its Burgers vector $\mathbf{b}$ satisfies [12]

$$e^{i\mathbf{b}\cdot\mathbf{M}} = -1. \tag{1}$$

In that case, there is an odd number of surface-state Dirac cones within which electrons pick up a phase π upon going around the position $\mathbf{r}_\mathrm{d}$ at which the dislocation line pierces the surface. The low-energy Dirac Hamiltonian for such surface states is accordingly

$$H = v(\mathbf{p} + e\mathbf{A}/c)\cdot\boldsymbol{\sigma}, \tag{2}$$

where v is the surface-state velocity, $\mathbf{p} = (p_x,p_y)$, $\boldsymbol{\sigma} = (\sigma_x,\sigma_y)$, and $\mathbf{A}(\mathbf{r})$ is the vector potential corresponding to a flux line with flux $hc/2e$ at position $\mathbf{r}_\mathrm{d}$, a "π-flux [13]." Since the total number of Dirac cones in the surface-state spectrum is odd if the strong index $\nu_0 = 1$, the number of surface cones described by a Dirac Hamiltonian without π-flux line is even if $\mathbf{b}\cdot\mathbf{M}$ is an odd multiple of π [12]. For simplicity we focus on the minimal model, in which there is a single surface state with low-energy effective Hamiltonian (2) in the vicinity of a dislocation line for which the condition (1) holds.

To elucidate the relation between the surface states and the helical states propagating along the dislocation line, it is instructive to analyze the eigenstates of the Hamiltonian (2) at energy $\varepsilon = \hbar v k$ using polar coordinates (r,θ). We choose the π-flux line—the location where the dislocation line pierces the surface—as the origin. This is a problem that previously was considered in the context of graphene [15,16]. With the choice

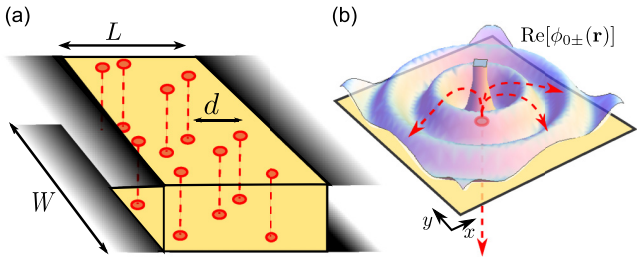

FIG. 1. (a) Topological insulator slab of size $L \times W$, with top and bottom surfaces connected via randomly placed dislocation lines with mean distance d. Ideal contacts are attached to the left and right, for top and bottom surfaces separately. (b) Zero-angular-momentum ($m = 0$) radial waves for nonzero wave number k at the surface of the topological insulator are transmitted perfectly into and out of the one-dimensional helical states along the dislocation line.

$\mathbf{A} = (\hbar/2er)\mathbf{e}_\theta$, where $\mathbf{e}_\theta$ is the unit vector for the azimuthal angle, the Hamiltonian (2) is invariant under rotations, so that we can look for eigenstates of the total angular momentum $j_z = l_z + (\hbar/2)\sigma_z$. These have the form

$$\psi_m(\mathbf{r}) = \begin{pmatrix} e^{i(m-1)\theta}\phi_{m+}(r) \\ e^{im\theta}\phi_{m-}(r) \end{pmatrix}, \tag{3}$$

where m is an integer and the radial wave functions $\phi_{m\pm}(r)$ satisfy

$$\left(\partial_r \pm \frac{m \pm 1/2}{r}\right)\phi_{m\mp}(r) = ik\phi_{m\pm}(r). \tag{4}$$

For generic m there is a single regular solution of Eq. (4), which describes the scattering of radial waves off the flux line. An exception is the case $m = 0$, for which there are *two* linearly independent solutions

$$\phi_{0\pm}(r) = \alpha_{\text{out}}\frac{e^{ikr}}{\sqrt{r}} \pm \alpha_{\text{in}}\frac{e^{-ikr}}{\sqrt{r}}, \tag{5}$$

for which the amplitudes α_{out} and α_{in} of outgoing and incoming radial waves can be freely chosen. Since time-reversal symmetry rules out backscattering for the $m = 0$ states and for the helical states propagating along the defect line [17], the incoming $m = 0$ mode must be fully transmitted into the outgoing defect state, and the incoming defect state is fully transmitted into the outgoing $m = 0$ mode, as shown schematically in Fig. 1(b).

Surface states in the presence of dislocation lines. We now consider transport properties and density of states of surface states for a slab geometry with multiple dislocation lines, piercing the top and bottom surfaces at random positions, see Fig. 1(a). We choose coordinates such that the bottom and top surfaces are parallel to the xy plane, with transport taking place in the x direction. For simplicity we take the dislocation lines to pierce bottom and top surfaces at the same in-plane position $\mathbf{r}_{\text{d}} = (x_{\text{d}}, y_{\text{d}})$, an assumption that is appropriate for a low-energy, long-wavelength description of a thin slab. The in-plane dimensions of the slab are $L \times W$, and we assume that the slab thickness is sufficient large, so that surface states at the bottom and top surfaces do not overlap in the absence of lattice dislocations. We take periodic boundary conditions in the y direction, choosing the aspect ratio W/L large enough that the results of our calculation do not depend on this choice of boundary conditions.

We calculate the density of states and the transport properties of the surface states using a scattering approach. The scattering matrix $S_{\sigma,\sigma'}$ links the amplitudes of incoming and outgoing waves in an "ideal" part of the two surfaces, to the left and right of a section with a finite density of dislocation lines. The indices $\sigma,\sigma' = +1, -1$ for the top and bottom surface, respectively. Dislocation lines connect the top and bottom surfaces, so that in general $S_{\sigma,\sigma'}$ is not block diagonal. We denote the amplitudes of incoming and outgoing waves to the left (right) of the section by vectors $a^{\text{in}}_{\text{L}\sigma n}$ and $a^{\text{out}}_{\text{L}\sigma n}$ ($a^{\text{in}}_{\text{R}\sigma n}$ and $a^{\text{out}}_{\text{R}\sigma n}$), respectively, where the index n refers to the transverse momentum $q_n = 2\pi n/W$. With this notation, the scattering matrix $S_{\sigma,\sigma'}$ relates outgoing and incoming waves as

$$\begin{pmatrix} a^{\text{out}}_{\text{L}\sigma} \\ a^{\text{out}}_{\text{R}\sigma} \end{pmatrix} = \sum_{\sigma'=\pm} S_{\sigma,\sigma'} \begin{pmatrix} a^{\text{in}}_{\text{L}\sigma'} \\ a^{\text{in}}_{\text{R}\sigma'} \end{pmatrix}. \tag{6}$$

Each component $S_{\sigma,\sigma'}$ can be decomposed into transmission and reflection blocks in the standard way,

$$S_{\sigma,\sigma'} = \begin{pmatrix} r_{\sigma,\sigma'} & t'_{\sigma,\sigma'} \\ t_{\sigma,\sigma'} & r'_{\sigma,\sigma'} \end{pmatrix}. \tag{7}$$

Our strategy will be to first calculate the scattering matrix $\tilde{S}$ for a "short" slab of length δL with only a pair of dislocation lines, and then calculate the scattering matrix S of a slab of full length L by concatenating scattering matrices of individual slices [18], see Fig. 2 (top). We place a pair of dislocation lines at $\mathbf{r}_{\text{d},1} = (x_{\text{d}}, y_{\text{d},1})$ and $\mathbf{r}_{\text{d},2} = (x_{\text{d}}, y_{\text{d},2})$, with $0 < x_{\text{d}} < \delta L$ and $0 < y_{\text{d},1} < y_{\text{d},2} < W$ randomly chosen. Since the aspect ratio $W/L \gg 1$, the pairwise placement of dislocation in a slab (compared to placement of single dislocation lines) does not affect the in-plane conductivity or the density of states. It does, however, allow us to choose a gauge such that the vector potential $\mathbf{A}(\mathbf{r})$ is nonzero for $x = x_{\text{d}}$ only,

$$\mathbf{A}(\mathbf{r}) = \frac{h}{2e}\delta(x - x_{\text{d}})\mathbf{e}_x \times \begin{cases} 1 & \text{if } y_{\text{d},1} < y < y_{\text{d},2}, \\ 0 & \text{else.} \end{cases} \tag{8}$$

An important further parameter in the calculation is the phase shift $e^{i\theta_{\text{d}}(\mathbf{r}_{\text{d}})}$ that electrons accumulate along the dislocation

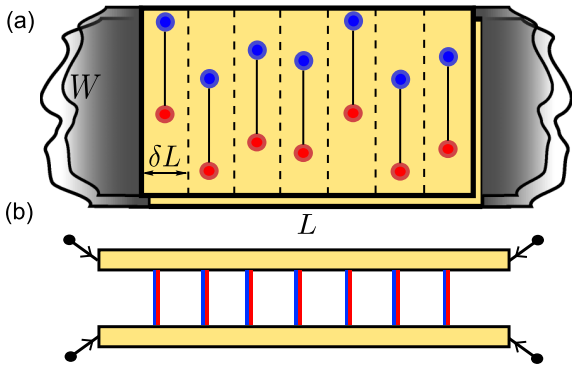

FIG. 2. Schematic picture of a top view (a) and side view (b) of the topological insulator slab. The calculational scheme involves the computation of the scattering matrix $\tilde{S}$ for a slab of width δL, followed by the concatenation of scattering matrices of individual slabs to obtain the scattering matrix S of the full structure.

line. For our calculations we found it advantageous to generalize the above procedure to slabs with an even number $2n$ of dislocation lines.

The calculation of the scattering matrix $\tilde{S}$ for a slab with a single pair of dislocation lines turned out to be an interesting problem in its own right. Although the scattering problem for a single dislocation line is easily solved in polar coordinates, see Eq. (4), we could not find a practical way to extract a scattering matrix for the geometry of Fig. 1(a) from this solution. Instead, we compute $\tilde{S}$ from a solution of the Dirac equation for a regularized (i.e., smeared out) π flux. (Without regularization the scattering problem with a π-flux line cannot be solved numerically.) The details of this calculation are given in the Supplemental Material [19].

Results. By concatenation of scattering matrices for slices of length δL, each with an even number $2n$ of dislocation lines, we can construct the full scattering matrix S for a slab of length L with randomly placed dislocation line pairs at concentration $1/d^2 = N_\mathrm{d}/WL$, with N_d the total number of dislocation lines, see Fig. 2(a). The Landauer formula expresses the in-plane conductance $G_\parallel$ and the cross conductance $G_\perp$ in terms of the transmission and reflection blocks of the scattering matrix S,

$$G_\parallel = \frac{e^2}{h} \sum_{\sigma,\sigma'=\pm 1} \mathrm{tr}\, t_{\sigma,\sigma'} t^\dagger_{\sigma,\sigma'}, \quad G_\perp = \frac{e^2}{h} \mathrm{tr}\, S_{+-} S^\dagger_{+-}. \tag{9}$$

For the calculation of the density of states, we consider a periodic array of slabs of length L. In this case the spectrum of Bloch states can be obtained from the condition that

$$S_{\kappa_x}(\varepsilon) \equiv \begin{pmatrix} 0 & e^{-i\kappa_x L} \\ e^{i\kappa_x L} & 0 \end{pmatrix} S(\varepsilon) \tag{10}$$

has a unit eigenvalue, where $\hbar\kappa_x$ is the crystal momentum.

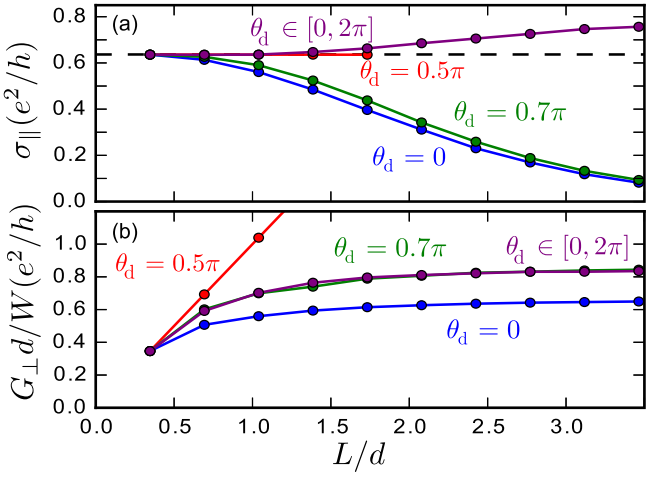

FIG. 3. Zero-energy in-plane conductivity $\sigma_\parallel$ (a) and cross conductance $G_\perp$ (b) for a slab of weak-and-strong topological insulator with a concentration $1/d^2$ of randomly placed dislocation lines. The different curves refer to different choices for the phases $\theta_\mathrm{d}(\mathbf{r}_\mathrm{d})$, as shown in the figure. The dashed line in (a) denotes the clean-limit in-plane conductivity $\sigma_{\parallel,0} = 2e^2/\pi h$. Data points denote an average over 500 disorder realizations, statistical error bars are typically smaller than the markers.

Results of the transport calculations are shown in Fig. 3 for an average over 500 random realizations of the dislocation lines. The energy ε is set to zero throughout the calculation, to maximize the effect of the dislocation lines. The sample length L is measured in units of the mean distance d between dislocation lines, which is the only fundamental length scale in the system at zero energy. The trivial W dependence of $G_\parallel$ is eliminated by considering the in-plane conductivity $\sigma_\parallel = G_\parallel L/W$. For $L/d \to 0$ we recover the clean-limit conductivity $\sigma_{\parallel,0} = 2e^2/\pi h$ of a pair of decoupled topological-insulator surfaces [20,21]. Anticipating a proportionality $G_\perp \propto W/d$, in Fig. 3(b) we show $G_\perp d/W$ as a function of L/d. Unlike the longitudinal conductivity $\sigma_\parallel$, the cross conductance vanishes in the clean limit $L/d \to 0$.

We observe that the in-plane conductivity has a strong dependence on the phase that electrons pick up while traveling along the dislocation lines. In particular, if all phases are equal, $\theta_\mathrm{d}(\mathbf{r}_\mathrm{d}) = \theta_\mathrm{d}$ for all $\mathbf{r}_\mathrm{d}$, $\sigma_\parallel$ is strongly suppressed for $L \gtrsim d$ except for $\theta_\mathrm{d} = \pm\pi/2$, for which we find that $\sigma_\parallel$ is independent of L/d within numerical accuracy [22] Figure 3 shows the representative cases $\theta_\mathrm{d} = 0$, 0.7π, and $\pi/2$, and we also present the case $0 \leqslant \theta_\mathrm{d}(\mathbf{r}_\mathrm{d}) < 2\pi$ uniformly distributed, which shows a slight increase of $\sigma_\parallel$ with L/d. The θ_d dependence of the cross conductance is not as strong; θ_d mainly determines the value at which $G_\perp$ saturates for large L/d. An exception is $\theta_\mathrm{d} = \pi/2$, for which we could not observe a saturation for the system sizes we could achieve.

Results for the density of states are shown in Fig. 4, again for four representative choices of the phase shifts $\theta_\mathrm{d}(\mathbf{r}_\mathrm{d})$. For fixed $\theta_\mathrm{d}(\mathbf{r}_\mathrm{d}) = 0$ we observe one or two gaps placed asymmetrically around $\varepsilon = 0$. For generic fixed $\theta(\mathbf{r}_\mathrm{d}) = \theta_\mathrm{d}$ (such as the case $\theta_\mathrm{d} = 0.7\pi$ shown in the figure) we observe an asymmetric gap around $\varepsilon = 0$. For $\theta_\mathrm{d}(\mathbf{r}_\mathrm{d}) = \pi/2$ a symmetric gap is restored, but with one midgap state at $\varepsilon = 0$ per dislocation line. Finally, for random $0 \leqslant \theta_\mathrm{d}(\mathbf{r}_\mathrm{d}) < 2\pi$ the gap is closed and the density of states near $\varepsilon = 0$ is essentially constant. The gap sizes and the occurrence of states at energy $\varepsilon = 0$ can be heuristically

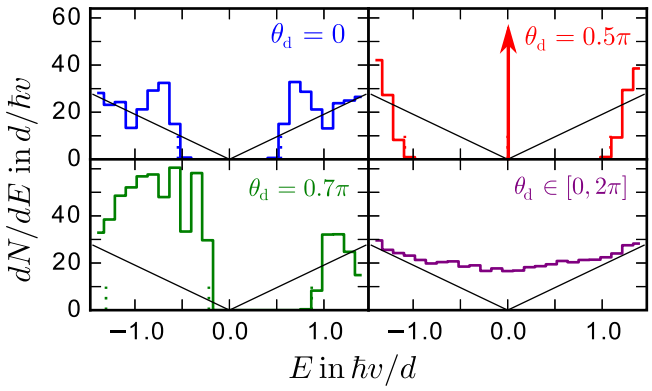

FIG. 4. Density of states dN/dE of a sample with dislocation line density $1/d^2$. The four curves represent the four representative scenarios for the choice of the phase shifts $\theta_\mathrm{d}(\mathbf{r}_\mathrm{d})$, as explained in the text. The vertical dashed lines correspond to energies calculated from Eq. (11). The thin black lines denote the ideal surface-state density of states without dislocation lines. The arrow represents a Dirac delta function at zero energy. Data points denote an average over five disorder realizations and 80 values of the crystal momentum κ_x.

explained by inspecting the phase matching condition for periodic trajectories traveling between the two surfaces at two neighboring dislocation lines at positions $\mathbf{r}_\mathrm{d}$ and $\mathbf{r}'_\mathrm{d}$. Including the Berry phase π for two-dimensional Dirac particles, this phase matching condition reads

$$\frac{2\varepsilon}{\hbar v}|\mathbf{r}_{\mathrm{d},i}-\mathbf{r}_{\mathrm{d},j}|+\theta_\mathrm{d}(\mathbf{r}_\mathrm{d})+\theta_\mathrm{d}(\mathbf{r}'_\mathrm{d})+\pi=0 \pmod{2\pi}. \quad (11)$$

Setting $|\mathbf{r}_\mathrm{d}-\mathbf{r}'_\mathrm{d}|=W/2n$, which is the largest typical distance between neighboring dislocation lines with $2n=6$ dislocations in a slice gives a good estimate of the numerically obtained gap sizes, see Fig. 4. The absence of states around $\varepsilon=0$ indicates that pairing of more distant dislocation lines does not occur.

Conclusion. We have investigated the effects of dislocation line zero modes coupling top and bottom surfaces of a strong-and-weak topological insulator slab. Our numerical calculations based on a scattering approach reveal a rich phenomenology for transport properties and density of states depending on the phase shifts $\theta_\mathrm{d}(\mathbf{r}_\mathrm{d})$ that electrons accumulate along the dislocation lines. For a thin, homogenous slab, a constant phase shift θ_d for all dislocation lines can be expected to be a good approximation. Except for the special cases $\theta_\mathrm{d}=\pm\pi/2$, this results in a spectral gap around zero energy and a corresponding strong suppression of in-plane transport. For a thick slab, where dislocation lines are not necessarily straight, it is conceivable that the phase shifts $\theta_\mathrm{d}(\mathbf{r}_\mathrm{d})$ are uniformly distributed. In this case, the in-plane conductivity and the density of states at the nodal energy are enhanced by the presence of dislocation lines. In this work, we neglected the wavefunction overlap for neighboring dislocation line modes. Recently, such hybridization effects were studied in Ref. [23].

In principle, the dislocation-line-mediated coupling between the top- and bottom surfaces can be described by an effective Hamiltonian involving two Dirac cones coupled by a matrix-valued "potential." Such an effective model was considered by Mong *et al.* in the context of the transport through a single surface of a weak topological insulator with two (coupled) Dirac cones [9]. The same description can also be applied to the system studied here, although the two Dirac cones now refer to different surfaces. Our analysis shows that the disorder type in such a model depends strongly on the phases accumulated along the dislocation lines: While a mass term is responsible for the opening of a spectral gap (as for $\theta_\mathrm{d}(\mathbf{r}_\mathrm{d})=\theta_\mathrm{d}$ constant, $\theta_\mathrm{d}\neq\pm\pi/2$), a constant scalar potential creates the asymmetry around $\varepsilon=0$ (which we observe for generic $0\leqslant|\theta_\mathrm{d}|<\pi/2$), and zero-average disorder terms lead to the "flattening" of the density-of-states singularity at zero energy. Establishing a more rigorous understanding of our results in terms of a Hamiltonian theory would be a formidable task for future work.

Acknowledgments. We gratefully acknowledge financial support by the Helmholtz Virtual Institute "New states of matter and their excitations" and the Alexander von Humboldt-Stiftung.

[1] C. L. Kane and E. J. Mele, Phys. Rev. Lett. **95**, 226801 (2005).
[2] C. L. Kane and E. J. Mele, Phys. Rev. Lett. **95**, 146802 (2005).
[3] B. A. Bernevig and S.-C. Zhang, Phys. Rev. Lett. **96**, 106802 (2006).
[4] J. E. Moore and L. Balents, Phys. Rev. B **75**, 121306 (2007).
[5] L. Fu, C. L. Kane, and E. J. Mele, Phys. Rev. Lett. **98**, 106803 (2007).
[6] R. Roy, Phys. Rev. B **79**, 195322 (2009).
[7] L. Fu and C. L. Kane, Phys. Rev. B **76**, 045302 (2007).
[8] Z. Ringel, Y. E. Kraus, and A. Stern, Phys. Rev. B **86**, 045102 (2012).
[9] R. S. K. Mong, J. H. Bardarson, and J. E. Moore, Phys. Rev. Lett. **108**, 076804 (2012).
[10] I. C. Fulga, B. van Heck, J. M. Edge, and A. R. Akhmerov, Phys. Rev. B **89**, 155424 (2014).
[11] J. C. Y. Teo and C. L. Kane, Phys. Rev. B **82**, 115120 (2010).
[12] Y. Ran, Y. Zhang, and A. Vishwanath, Nat. Phys. **5**, 298 (2009).
[13] K.-I. Imura, Y. Takane, and A. Tanaka, Phys. Rev. B **84**, 035443 (2011); R.-J. Slager, A. Mesaros, V. Juričić, and J. Zaanen, *ibid.* **90**, 241403 (2014).
[14] Y. Ando, J. Phys. Soc. Jpn. **82**, 102001 (2013).
[15] J. Heinl, M. Schneider, and P. W. Brouwer, Phys. Rev. B **87**, 245426 (2013).
[16] M. Schneider and P. W. Brouwer, Phys. Rev. B **89**, 205437 (2014).
[17] For the gauge chosen here, time-reversal amounts to the operation $\psi\to i\sigma_y\psi^*$, followed by a gauge transformation $\psi\to e^{i\theta}\psi$. This corresponds to the change $m\to -m$, so that time-reversal symmetry forbids backscattering for the $m=0$ mode only.
[18] J. H. Bardarson, J. Tworzydlo, P. W. Brouwer, and C. W. J. Beenakker, Phys. Rev. Lett. **99**, 106801 (2007).
[19] See Supplemental Material http://link.aps.org/supplemental/10.1103/PhysRevB.93.161105 for the derivation of the scattering matrix as well as for details of the transport and density of states calculation.
[20] M. I. Katsnelson, Eur. Phys. J. B **51**, 157 (2006).
[21] J. Tworzydlo, B. Trauzettel, M. Titov, A. Rycerz, and C. W. J. Beenakker, Phys. Rev. Lett. **96**, 246802 (2006).
[22] In the case $\theta_\mathrm{d}=\pi/2$, we observe that the scattering matrix at zero energy ceases to be unitary for $L/d\gtrsim 2$, which is the reason for the relatively small upper bound on the system sizes shown in Fig. 3. This can be understood from the perspective of bound state formation, once the number of bound states N_d is of the same order as the number of modes considered in the scattering matrix, N_eff.
[23] R.-J. Slager, V. Juricic, V. Lahtinen, and J. Zaanen, arXiv:1509.07705v2 (2015).

Supplemental Material

I. SCATTERING MATRIX FOR SCATTERING OFF A DISLOCATION LINE

A. Polar coordinates

In the main text we derived the scattering states for a π flux line. For a true flux line, the scattering states for a π flux and a $-\pi$ flux are identical. Here, we consider the same problem, but include a regularization of the flux line. The regularization will lead to a complete backscattering of the "$m = 0$" mode, see Eq. (5). With regularization, the backscattering phase shift depends on the sign of the flux.

We start with a sharp flux tube for which the vector potential in a polar gauge reads

$$\mathbf{A}(\mathbf{r}) = \frac{hc}{e}\frac{\Phi}{2\pi r}\mathbf{e}_\theta, \tag{1}$$

where Φ labels the "flux" of the dislocation line in units of the flux quantum (i.e. $\Phi = \pm 1/2$ for a $\pm\pi$-flux). With this choice for the vector potential $\mathbf{A}$ the Dirac equation has the form

$$v(\mathbf{p} + e\mathbf{A}/c)\cdot\boldsymbol{\sigma}\psi = -i\hbar v \begin{pmatrix} 0 & D_- \\ D_+ & 0 \end{pmatrix}\psi = \varepsilon\psi, \tag{2}$$

with operators

$$D_\pm = e^{\pm i\theta}(\partial_r \pm \frac{i}{r}\partial_\theta \mp \frac{\Phi}{r}). \tag{3}$$

Since Eq. (1) uses a rotationally symmetric gauge the states can be assumed to be eigenstates of the total angular momentum $j_z = l_z + \frac{\hbar}{2}\sigma_z$. For $j_z = \hbar\,(m - 1/2)$ they have the form of Eq. (3), where $m \in \mathbb{Z}$. The radial part of the wavefunction is then determined by the equations

$$\left(\partial_r + \frac{m+\Phi}{r}\right)\phi_{m,-}(r) = ik\phi_{m,+}(r), \tag{4}$$

$$\left(\partial_r - \frac{m+\Phi-1}{r}\right)\phi_{m,+}(r) = ik\phi_{m,-}(r). \tag{5}$$

where $k = \varepsilon/\hbar v$.

It is convenient to introduce the kinematic angular momentum

$$j_{z,\mathrm{kin}} = [\mathbf{r}\times(\mathbf{p} + e\mathbf{A}/c)]_z + \frac{\hbar}{2}\sigma_z = \hbar\,(m - 1/2 + \Phi) \tag{6}$$

The case of interest is $j_{z,\mathrm{kin}} = 0$, *i.e.*, $m = 1/2 - \Phi$. Here, the radial equations become

$$\left(\partial_r + \tfrac{1}{2r}\right)\phi_\pm(r) = ik\phi_\mp(r), \tag{7}$$

where we dropped the index m. These equations are straightforward to solve, and one finds independent incoming and outgoing radial solutions.

$$\begin{pmatrix}\phi_+(r)\\ \phi_-(r)\end{pmatrix} = \alpha_{\mathrm{out}}\frac{1}{\sqrt{r}}e^{ikr}\begin{pmatrix}1\\1\end{pmatrix} + \alpha_{\mathrm{in}}\frac{1}{\sqrt{r}}e^{-ikr}\begin{pmatrix}1\\-1\end{pmatrix}. \tag{8}$$

As argued in the main text, the interpretation of the fact that the coefficients α_{out} and α_{in} can be chosen independently is that the incoming $j_{z,\mathrm{kin}} = 0$ surface mode is fully transmitted into the outgoing mode in the dislocation line, whereas the incoming dislocation line mode is transmitted in the outgoing surface mode.

Next, we regularize the π-flux tube. This requires the breaking of time-reversal symmetry and induces full backscattering of the $j_{z,\mathrm{kin}} = 0$ modes. The simplest way to regularize the flux line using polar coordinates is to take Φ in Eq. (1) r dependent. We choose $\Phi(r) = 0$ for $r < \rho$ and $\Phi = \pm 1/2$ for $r > \rho$, which corresponds to a situation in which the flux is not located at the origin, but on a circle of radius ρ. Obviously, the problem is now well-defined at the origin, and for $r < \rho$ we can take the known solution of the Dirac equation with $\Phi = 0$, matching to the solution (8) at $r = \rho$. For $\Phi = 1/2$ and $m = 0$ this procedure yields $\alpha_{\mathrm{out}} = -\alpha_{\mathrm{in}}$. For $\Phi = -1/2$ and $m = 1$ we find $\alpha_{\mathrm{out}} = \alpha_{\mathrm{in}}$.

Summarizing: For a regularized flux line the zero-angular-momentum mode is fully backscattered, but with opposite phase factors for a regularization as a positive or as a negative flux. This property will be used in the numerical approach to find the scattering matrix of a dislocation line in Cartesian coordinates, which is outlined in the next Sections.

B. Cartesian coordinates: Scattering off a regularized flux line

We first consider the scattering problem for a *single* surface Hamiltonian (2) with a regularized vector potential $\mathbf{A}(\mathbf{r})$. We consider scattering off a string of $2n$ flux lines, all with the same x coordinate x_d, but with different y coordinates $0 < y_{\mathrm{d},j} < W$, $j = 1, 2, \ldots, 2n$.

For compatibility with the use of cartesian coordinates, we use a different gauge for the vector potential than in the previous subsection,

$$\mathbf{A}(\mathbf{r}) = \frac{hc}{2e}\delta(x - x_\mathrm{d})\mathbf{e}_x\alpha(y), \tag{9}$$

where the function $\alpha(y)$ jumps by one at $y = y_{\mathrm{d},j}$, see Eq. (8) of the main text. The vector potential (9) corresponds to the matching condition

$$\lim_{x\downarrow x_\mathrm{d}} \psi(x, y) = s(y) \lim_{x\uparrow x_\mathrm{d}} \psi(x, y), \tag{10}$$

where

$$s(y) = e^{-i\pi\alpha(y)}. \tag{11}$$

For sharp flux lines [see Fig. 1(a)], the phase of $s(y)$ changes by π at each flux line. Since $s(y)$ is confined to the unit circle in the complex plane, regularization of the flux line corresponds to "smearing out" the π jumps of the phase factor. There are two possibilities to regularize these jumps: A continuous increase by π or a continuous decrease by π, corresponding to the two signs of the flux in a regularized flux line. In our numerical calculations we smear out each flux line over a distance a, see Fig. 1(b), where we make sure that the distance between neighboring flux lines is much larger than a. We encode the different regularization possibilities by taking the expression

$$s_{\tau_1\ldots\tau_{2n}}(y) = -\,e^{\frac{i\pi}{2}\sum_{j=1}^{2n}\tau_j\left[f\left(\frac{y-y_{\mathrm{d},j}}{a}\right)+f\left(\frac{y-y_{\mathrm{d},j}-W}{a}\right)+f\left(\frac{y-y_{\mathrm{d},j}+W}{a}\right)-1\right]}, \tag{12}$$

where $\tau_j = \pm 1$ labels the sign of the regularization for the jth flux line and the function $f(p)$ is defined as

$$f(p) = \begin{cases} -1 & \text{if } p \le -1, \\ \tanh(\pi p/\sqrt{1-p^2}) & \text{if } -1 < p < 1, \\ 1 & \text{if } p \ge 1. \end{cases} \tag{13}$$

The function $f(p)$ is infinitely differentiable at $p = \pm 1$. All 2^{2n} functions $s_{\tau_1\ldots\tau_{2n}}$ have the smeared step as their real part, but different imaginary parts, with positive and negative peaks at each $y_{\mathrm{d},j}$, thus realizing all 2^{2n} possible realizations of the $2n$ flux lines.

The scattering matrix is written in the basis of propagating eigenstates in ideal reference regions immediately to the left and right of the string of flux lines. Following Ref. 1, we take the Hamiltonian for these reference regions as $H_\mathrm{ref} = vp_x\sigma_x$. The omission of the term $vp_y\sigma_y$ is inconsequential, since the reference regions are used for reference purposes only and their length is sent to zero at the end of the calculation. In each reference region we expand the wavefunction $\psi(\mathbf{r})$ in basis states $|q_n, \pm\rangle$, where the sign $\pm$ refers to right-/leftmoving states, and $q_n = 2\pi n/W$ labels the transverse momenta for periodic boundary conditions. The corresponding wavefunctions are

$$\phi_{n,\pm}(x, y) = \langle x, y|q_n, \pm\rangle = \frac{1}{\sqrt{2W}} e^{\pm ikx + iq_n y} \begin{pmatrix} 1 \\ \pm 1 \end{pmatrix}. \tag{14}$$

To obtain the scattering matrix of the string of (regularized) dislocation lines, we solve for scattering states of the form

$$\psi(x, y) = \begin{cases} \sum_n \left[a^\mathrm{in}_{\mathrm{L},n}\phi_{n,+}(x, y) + a^\mathrm{out}_{\mathrm{L},n}\phi_{n,-}(x, y)\right] & \text{for } x < x_\mathrm{d}, \\ \sum_n \left[a^\mathrm{in}_{\mathrm{R},n}\phi_{n,-}(x, y) + a^\mathrm{out}_{\mathrm{R},n}\phi_{n,+}(x, y)\right] & \text{for } x > x_\mathrm{d}, \end{cases} \tag{15}$$

and obtain the scattering matrix from the linear relation

$$\begin{pmatrix} a^\mathrm{out}_L \\ a^\mathrm{out}_R \end{pmatrix} = S \begin{pmatrix} a^\mathrm{in}_L \\ a^\mathrm{in}_R \end{pmatrix}, \quad S = \begin{pmatrix} r & t' \\ t' & r \end{pmatrix}. \tag{16}$$

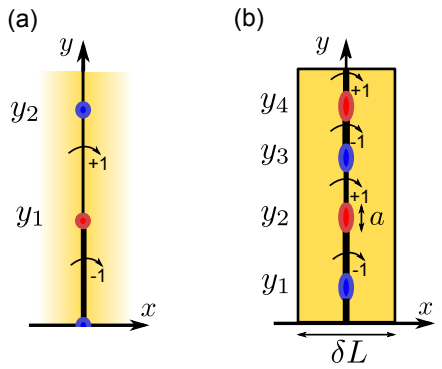

FIG. 1: Setup of the scattering problem for a string of $2n$ dislocation lines / π-fluxes located at $x = x_{\rm d}$. The curved arrows denote the phase shift of wavefunctions $s(y)$ that jumps (a) abruptly for sharply defined π-fluxes or (b) is smeared out over distance a in a regularized setup that also features free propagation in the transport direction of total length δL.

The amplitudes r_{nm}, r'_{nm}, t_{nm}, and t'_{nm} of the reflection and transmission blocks of the scattering matrix can be calculated from the matching condition (10). Since the matching condition does not relate to the pseudospin and only affects the phase of the wavefunction, we directly conclude that there is no reflection caused by the dislocation line,

$$r_{nm} = r'_{nm} = 0. \tag{17}$$

To obtain t_{nm}, we substitute Eq. (15) into Eq. (10) and perform a Fourier transform to y,

$$t_{nm} \;=\; t'^{*}_{mn} = \frac{1}{W}\int_0^W dy s(y) e^{i(q_m - q_n)y}. \tag{18}$$

We have suppressed the dependence of the transmission matrices t and t' and the function $s(y)$ on the flux regularization parameters τ_j to keep our notation simple.

Up to this point the number of transverse modes has been infinite. For a practical implementation, we need to employ a mode cutoff N such that $n = -N+1, ..., 0, ..., N-1$. Naive truncation of the transmission matrices t and t', however, leads to a non-unitary scattering matrix. To circumvent this problem, we add segments of a finite width $\delta L/2$ to the left and to the right of the impurity lines, as shown in Fig. 1(b). The scattering matrix for such slices are known. For zero energy the reflection and transmission amplitudes ρ_{nm} and τ_{nm} read [2]

$$\begin{aligned} \rho_{nm} &= -\rho'_{nm} = -\tanh(q_n \delta L/2)\delta_{nm}, \\ \tau_{nm} &= \tau'_{nm} = \frac{1}{\cosh(q_n \delta L/2)}\delta_{nm}. \end{aligned} \tag{19}$$

Since modes with high momenta $q_n \gg 2/\delta L$ are blocked from propagation, we should be allowed to safely truncate the scattering matrix of the dislocation line string with the two dislocation-line free sigments of length $\delta L/2$ on each side, once N is much larger than $W/\delta L$. Thus, we consider the concatenated scattering matrix of a single surface in a geometry of Fig. 1(b) with regularized fluxes which reads

$$S_{\rm reg}^{\tau_1 \ldots \tau_{2n}} = \begin{pmatrix} \rho & \tau' \\ \tau & \rho' \end{pmatrix} \otimes \begin{pmatrix} 0 & t'^{\tau_1 \ldots \tau_{2n}} \\ t^{\tau_1 \ldots \tau_{2n}} & 0 \end{pmatrix} \otimes \begin{pmatrix} \rho & \tau' \\ \tau & \rho' \end{pmatrix} = \begin{pmatrix} \rho + \tau' t' \frac{1}{1-\rho t \rho' t'} \rho t \tau & \tau' t' \frac{1}{1-\rho t \rho' t'} \tau' \\ \tau \frac{1}{1-t\rho' t' \rho} t \tau & \rho' + \tau \frac{1}{1-t\rho' t' \rho} t \rho' t' \tau' \end{pmatrix} \tag{20}$$

where $\otimes$ denotes concatenation of scattering matrices and we restored the regularization indices τ_j. For sufficiently large N the matrix $S_{\rm reg}^{\tau_1 \ldots \tau_{2n}}$ is unitary to within our numerical accuracy.

C. Structure of regularized scattering matrices

The calculation of Sec. I A showed, that in the limit $\delta L \gg a$ the choice of the regularization of the dislocation lines affects precisely one mode. This can also be verified numerically for plane-wave scattering states.

For the numerical analysis, we take $a \ll \delta L \ll d$, with $d = \min_j |y_{\mathrm{d},j} - y_{\mathrm{d},j-1}|$ the minimum distance between neighboring flux lines, and choose the mode cut-off $N \gg W/\delta L$. We then find that the *difference*

$$\Delta S_{\mathrm{reg}}^{(j)} \equiv S_{\mathrm{reg}}^{\tau_1,\ldots,\tau_{j-1},+,\tau_{j+1},\ldots,\tau_{2n}} - S_{\mathrm{reg}}^{\tau_1,\ldots,\tau_{j-1},-,\tau_{j+1},\ldots,\tau_{2n}} \tag{21}$$

is (i) independent of the regularization parameters $\tau_1,\ldots,\tau_{j-1},\tau_{j+1},\ldots,\tau_{2n}$, (ii) of unit rank, and (iii) with norm two. Hence, there exists a normalized vector v_j such that

$$\Delta S_{\mathrm{reg}}^{(j)} = 2 v_j v_j^\dagger, \tag{22}$$

independent of $\tau_1,\ldots,\tau_{j-1},\tau_{j+1},\ldots,\tau_{2n}$. (Since at zero energy the problem at hand has chiral symmetry, $\sigma_z H \sigma_z = -H$, the scattering matrix is hermitian and the single non-vanishing eigenvalue of $\Delta S_{\mathrm{reg}}^{(j)}$ has to be ± 2. For our choice of the function $s(y)$, we find the positive sign realized.) The interpretation of this result is that difference $\Delta S_{\mathrm{reg}}^{(j)}$ relates to the choice of the regularization of the jth flux line only. Since the change of the regularization of the jth flux line changes the sign of the scattering amplitude of the zero angular momentum mode (defined with respect to the jth flux line) and leaving all other scattering amplitudes unchanged, the difference $\Delta S_{\mathrm{reg}}^{(j)}$ precisely describes that contribution to the total scattering matrix S_{reg} that originates from scattering of the zero angular momentum mode for the jth flux line off that same flux line. As long as the separation between flux lines is much larger than the slice width δL, contributions from different flux lines do not interfere, which is why $\Delta S_{\mathrm{reg}}^{(j)}$ and, hence, the vector v_j is independent of the regularization parameters $\tau_1,\ldots,\tau_{j-1},\tau_{j+1},\ldots,\tau_{2n}$ of the remaining $2n-1$ flux lines.

Repeating this procedure for all $2n$ flux lines, we find that we can write

$$S_{\mathrm{reg}}^{\tau_1\ldots\tau_{2n}} = S_0 + \sum_{j=1}^{2n} \tau_j \, v_j v_j^\dagger \tag{23}$$

with

$$S_0 = \frac{1}{2}(S_{\mathrm{reg}}^{+\ldots+} + S_{\mathrm{reg}}^{-\ldots-}) \tag{24}$$

the part of the scattering matrix that describes transport not affected by the choice of regularization of any dislocation line. It has rank $2N-1-2n$. In keeping with the above interpretation, the matrix S_0 describes scattering from the non-zero-angular momentum modes, whereas the term $v_j v_j^\dagger$ describes the contribution to S_{reg} from the zero-angular momentum mode at the jth flux line.

It is instructive (though inessential for future calculations) to look at the Fourier spectrum of the vectors v_j whose first (second) $2N+1$ entries encode the real space structure of the eigenmodes scattering at the dislocation lines at position $x = \mp\delta L/2$ at the left (right) lead. The Fourier transforms are real and depicted in Fig. 2 where dashed lines indicate the positions of the dislocation lines.

D. Time-reversal symmetry

The scattering matrices $S_{\mathrm{reg}}^{\tau_1\cdots\tau_{2n}}$ are not time-reversal symmetric because of the presence of the smeared flux line. However, the matrix S_0 is time-reversal symmetric. We here summarize how time reversal symmetry is implemented in the present problem.

The time-reversal operator is $\mathcal{T} = i\sigma_y K$, with K complex conjugation. It satisfies $\mathcal{T}^2 = -1$. Time reversal symmetry applied to basis states gives

$$\mathcal{T}\,|q_n,\pm\rangle = \pm\,|-q_n,\mp\rangle\,. \tag{25}$$

If the Hamiltonian is time-reversal symmetric, the scattering matrix satisfies $\langle f|\hat{S}|i\rangle = \langle \mathcal{T}i|\hat{S}|\mathcal{T}f\rangle$. From that, one finds the conditions

$$t_{nm} = t'_{-m,-n}, \quad r_{nm} = -r_{-m,-n}, \quad r'_{nm} = -r'_{-m,-n}$$

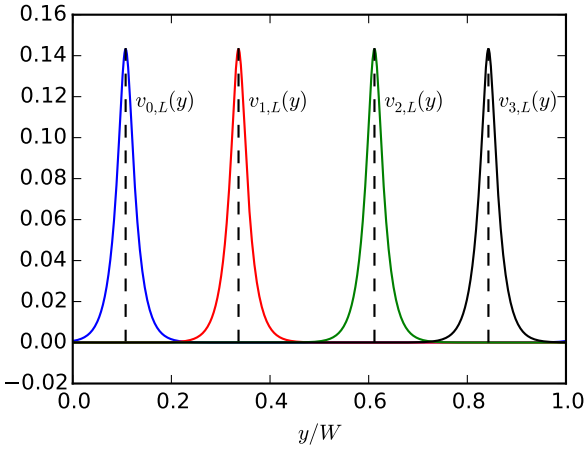

FIG. 2: Fourier transform of the first $2N+1$ entries $v_{j,L}$ of the vectors v_j, $j=1,2,3,4$ ($2n=4$) that describes the real space wavefunction of the eigenmodes scattering at the dislocation lines at $y=y_{\mathrm{d},j}$ at the left lead at $x=-\delta L/2$. The parameters are $\delta L=0.03W$, $a=0.3\delta L$, $N=400$.

for the reflection and transmission amplitudes. One rewrite these equations using the matrix

$$U=\begin{pmatrix} 0 & \dots & 0 & 1 \\ 0 & \dots & 1 & 0 \\ \vdots & & & \vdots \\ 1 & 0 & \dots & 0 \end{pmatrix} \tag{26}$$

with $U^2=1$, which switches from positive to negative momenta. Then:

$$t=Ut'^{\mathrm{T}}U,\quad r=-Ur^{\mathrm{T}}U,\quad r'=-Ur'^{\mathrm{T}}U,$$

or, equivalently,

$$S=-\begin{pmatrix} U & 0 \\ 0 & -U \end{pmatrix} S^{\mathrm{T}} \begin{pmatrix} U & 0 \\ 0 & -U \end{pmatrix}. \tag{27}$$

As remarked above, the scattering matrices $S_{\mathrm{reg}}^{\sigma\sigma'}$ are not time-reversal symmetric because of the presence of the smeared flux tube. However, the matrix S_0 is time-reversal symmetric. Similarly, the difference $\Delta S_{\mathrm{reg}}^{(j)}$ acquires a minus sign under time reversal. This property can be used to remove the over-all phase factor ambiguity of the vectors v_j [the phase was not specified in the definition (23)], up to a sign ambiguity,

$$v_j=\begin{pmatrix} U & 0 \\ 0 & -U \end{pmatrix} v_j^*. \tag{28}$$

E. Scattering scattering matrix $\tilde{S}$ for a thin slice

The key element of our calculation of the scattering scattering matrix $\tilde{S}$ for a thin slice is that a regularization of the π-flux lines does not affect the way angular modes with nonzero (kinetic) angular momentum are scattered off the flux line, see Eq. (4), but that regularization does lead to full backscattering of the zero angular momentum modes. In the real weak-and-strong topological insulator, it is these latter modes that are fully transmitted from the surface into the dislocation line and vice versa.

As we have discussed above, the backscattering phase shift for the zero angular momentum mode depends on whether one chooses to regularize the π-flux line with a magnetic field in the positive z direction, or with a magnetic field in the negative z direction. By calculating the scattering matrices with different regularizations of the π-flux lines, we can separate the contributions from angular modes with nonzero angular momentum, which are independent of the

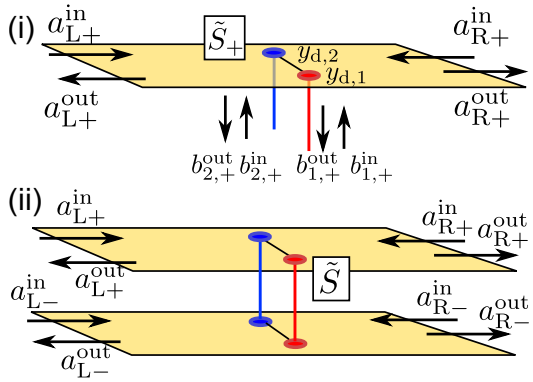

FIG. 3: (i) Scattering setup for two dislocation lines impinging on a top surface. The dislocation lines are explicitly treated as terminals in the unitary scattering relation Eq. (29) involving the scattering matrix $\tilde{S}_+$. (ii) Enlarged scattering matrix $\tilde{S}$ describing scattering between top and bottom surface via a pair of dislocation lines.

regularization and which do not transmit into the dislocation line from modes with zero angular momentum, which are dependent on the regularization, and which are fully transmitted into the dislocation line. The decomposition (23) allows us to uniquely separate these different contributions to the scattering matrix.

These arguments can be used to construct a larger scattering matrix for a surface and the $2n$ helical modes corresponding to the $2n$ dislocation lines piercing the surface at $x = x_{\rm d}$. We denote the amplitudes for the surface-state modes in the top surface by $a^{\rm in,out}_{\rm L,R,+}$, and the amplitudes for surface-state modes in the bottom surface by $a^{\rm in,out}_{\rm L,R,-}$. We denote the amplitudes of the upward and downward traveling helical modes in the jth dislocation line at the top surface by $b^{\rm in}_{j,+}$ and $b^{\rm out}_{j,+}$, respectively, and we denote the amplitudes of the upward and downward traveling helical modes in the jth dislocation line at the bottom surface by $b^{\rm out}_{j,-}$ and $b^{\rm in}_{j,-}$, respectively. Following the above arguments, the scattering matrix $\tilde{S}_+$ relating the surface states in the top surface and the helical modes along the dislocation lines at the top surface then reads

$$\begin{pmatrix} a^{\rm out}_{\rm L,R+} \\ b^{\rm out}_{1,+} \\ \vdots \\ b^{\rm out}_{2n,+} \end{pmatrix} = \underbrace{\begin{pmatrix} S_0 & v_1 & \dots & v_{2n} \\ e^{i\phi_1} v_1^\dagger & 0 & \dots & 0 \\ \vdots & \vdots & & \vdots \\ e^{i\phi_{2n}} v_{2n}^\dagger & 0 & \dots & 0 \end{pmatrix}}_{\equiv \tilde{S}_+} \begin{pmatrix} a^{\rm in}_{\rm L,R+} \\ b^{\rm in}_{1,+} \\ \vdots \\ b^{\rm in}_{2n,+} \end{pmatrix}. \tag{29}$$

A similar expression can be found for the scattering matrix $\tilde{S}_-$ relating the surface states in the top surface and the helical modes along the dislocation lines at the bottom surface. The phases ϕ_j can not be determined using the above arguments. Instead, we can determine these phases from the condition of time-reversal symmetry. With the convention

$$\mathcal{T}|{\rm in}\rangle = -|{\rm out}\rangle \quad \text{and} \quad \mathcal{T}|{\rm out}\rangle = |{\rm in}\rangle \tag{30}$$

for the time-reversal symmetry operation $\mathcal{T}$ (with $\mathcal{T}^2 = -1$) on the in and outgoing dislocation line states $|{\rm in}\rangle$ and $|{\rm out}\rangle$, we find that $\tilde{S}_+$ must obey the condition

$$\tilde{S}_+ = -\begin{pmatrix} U & 0 & 0 \\ 0 & -U & 0 \\ 0 & 0 & -1_{2n} \end{pmatrix} \tilde{S}_+^{\rm T} \begin{pmatrix} U & 0 & 0 \\ 0 & -U & 0 \\ 0 & 0 & -1_{2n} \end{pmatrix}, \tag{31}$$

where the matrix U was defined in Eq. (26) and where 1_{2n} is the $2n \times 2n$ unit matrix. Comparison with Eq. (29) and using Eq. (28) then gives that $\phi_j = 0$.

In the next step we connect the scattering matrices $\tilde{S}_+$ and $\tilde{S}_-$ to obtain the scattering matrix $\tilde{S}$ describing the scattering off a string of dislocation lines of surface states in *both* surfaces of the weak-and-strong topological insulator. The procedure is shown schematically in Fig. 3(ii). In order to connect the two layers we need the

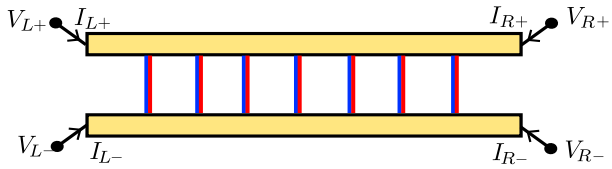

FIG. 4: Schematic picture of a sideview of the topological insulator slab, together with the definitions of the potentials and currents at the four contacts.

additional requirement

$$b^{\rm in}_{j,+} = e^{i\theta_{{\rm d},j}} b^{\rm out}_{j,-}, \tag{32}$$
$$b^{\rm out}_{j,+} = -e^{-i\theta_{{\rm d},j}} b^{\rm in}_{j,-}, \tag{33}$$

which relates the helical-state amplitudes at the top and bottom layers. The phase $\theta_{{\rm d},j}$ describes the phase accumulated during the propagation along the dislocation line. The minus sign ensures that the time-reversal convention Eq. (30) applies to each layer separately. Eliminating the amplitudes for the dislocation line and using the same sign choice for v_j for top and bottom layer, *c.f.* Eq. (28), one arrives at the scattering matrix

$$\begin{pmatrix} a^{\rm out}_{\rm L+} \\ a^{\rm out}_{\rm R+} \\ a^{\rm out}_{\rm L-} \\ a^{\rm out}_{\rm R-} \end{pmatrix} = \tilde{S} \begin{pmatrix} a^{\rm in}_{\rm L+} \\ a^{\rm in}_{\rm R+} \\ a^{\rm in}_{\rm L-} \\ a^{\rm in}_{\rm R-} \end{pmatrix}, \quad \tilde{S} = \begin{pmatrix} S_0 & \sum_{j=1}^{2n} e^{i\theta_{{\rm d},j}} v_j v_j^\dagger \\ -\sum_{j=1}^{2n} e^{i\theta_{{\rm d},j}} v_j v_j^\dagger & S_0 \end{pmatrix}. \tag{34}$$

One easily verifies that this scattering matrix is time-reversal symmetric.

II. TRANSPORT PROPERTIES

For a description of transport properties, four ideal contacts are added to the top and bottom surfaces for $x < 0$ and $x > L$. Following Ref. 2 these are described by the Hamiltonian $H_{\rm ref} = v p_x \sigma_x$. We do not place dislocation lines in the contact regions, so that the scattering states in the contacts remain unaffected by the presence of the dislocation lines. Voltages $V_{{\rm L}\sigma}$ and $V_{{\rm R}\sigma}$ and currents $I_{{\rm L}\sigma}$ and $I_{{\rm R}\sigma}$ at the four contacts are defined as shown in Fig. 4.

The different transport properties require different configurations for the voltages at the four contacts. The in-plane conductance $G_\parallel = I_\parallel / V_\parallel$ is obtained by setting $V_{\rm L+} = V_{\rm L-} = V_\parallel$ and $V_{\rm R+} = V_{\rm R-} = 0$ and measuring the current $I_\parallel = I_{\rm R+} + I_{\rm R-} = I_{\rm L+} + I_{\rm L-}$. The cross conductance $G_\perp = I_\perp / V_\perp$ between the bottom and top surface is defined by setting $V_{\rm L+} = V_{\rm R+} = V_\perp$, $V_{\rm L-} = V_{\rm R-} = 0$, and measuring the total current $I_\perp = I_{\rm L-} + I_{\rm R-} = -(I_{\rm L+} + I_{\rm R+})$. Expressions for $G_\parallel$ and $G_\perp$ in terms of the scattering matrix and the results of numerical calculations of $G_\parallel$ and $G_\perp$ are given in the main text.

In addition to $G_\parallel$ and $G_\perp$ we also considered the drag resistance $R_{\rm d} = V_{\rm d}/I_{\rm d}$, which is the ratio of an open-circuit voltage at one surface induced by an applied current at the other surface. It is based on the configuration $I_{\rm L+} = -I_{\rm R+} = I_{\rm d}$, $I_{\rm L-} = I_{\rm R-} = 0$, $V_{\rm R-} = 0$, and $V_{\rm L-} = V_{\rm d}$. For the calculation of the drag resistance $R_{\rm d}$ we start from the conductance matrix connecting a generic configuration of voltages and currents. Using current conservation and the reference $V_{R-} \equiv 0$, we have

$$\begin{pmatrix} I_{\rm L+} \\ I_{\rm L-} \\ I_{\rm R+} \end{pmatrix} = \begin{pmatrix} G_{\rm L+,L-} + G_{\rm L+,R+} + G_{\rm L+,R-} & -G_{\rm L+,L-} & -G_{\rm L+,R+} \\ -G_{\rm L-,L+} & G_{\rm L-,L+} + G_{\rm L-,R+} + G_{\rm L-,R-} & -G_{\rm L-,R+} \\ -G_{\rm R+,L+} & -G_{\rm R+,L-} & G_{\rm R+,L+} + G_{\rm R+,L-} + G_{\rm R+,R-} \end{pmatrix} \begin{pmatrix} V_{\rm L+} \\ V_{\rm L-} \\ V_{\rm R+} \end{pmatrix} \tag{35}$$

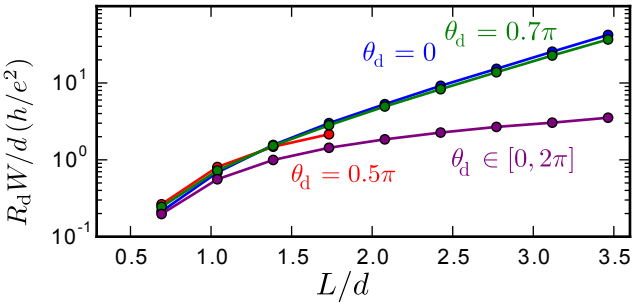

FIG. 5: Zero-energy drag resistance R_d for a slab of weak-and-strong topological insulator with a concentration $1/d^2$ of randomly placed dislocation lines. The different curves refer to different choices for the phases $\theta_d(\mathbf{r}_d)$, as shown in the figure. Data points denote an average over 500 disorder realizations, statistical error bars are typically smaller than the markers.

where, in terms of the scattering matrix defined in Eq. (7),

$$G_{L\sigma,L\sigma'} = \frac{e^2}{h}\mathrm{tr}\, r_{\sigma\sigma'} r^\dagger_{\sigma\sigma'}, \tag{36}$$

$$G_{L\sigma,R\sigma'} = \frac{e^2}{h}\mathrm{tr}\, t'_{\sigma\sigma'} t'^\dagger_{\sigma\sigma'}, \tag{37}$$

$$G_{R\sigma,L\sigma'} = \frac{e^2}{h}\mathrm{tr}\, t_{\sigma\sigma'} t^\dagger_{\sigma\sigma'}, \tag{38}$$

$$G_{R\sigma,R\sigma'} = \frac{e^2}{h}\mathrm{tr}\, r'_{\sigma\sigma'} r'^\dagger_{\sigma\sigma'}. \tag{39}$$

Inverting Eq. (35), the resistance matrix is obtained as

$$\begin{pmatrix} V_{L+} \\ V_{L-} \\ V_{R+} \end{pmatrix} = \begin{pmatrix} R_{L+,L+} & R_{L+,L-} & R_{L+,R+} \\ R_{L-,L+} & R_{L-,L-} & R_{L-,R+} \\ R_{R+,L+} & R_{R+,L-} & R_{R+,R+} \end{pmatrix} \begin{pmatrix} I_{L+} \\ I_{L-} \\ I_{R+} \end{pmatrix} \tag{40}$$

and the configuration specified for the drag resistance ($I_{L+} = -I_{R+} = I_d$, $I_{L-} = I_{R-} = 0$, $V_{R-} = 0$, and $V_{L-} = V_d$) can be applied. Solving for $R_d = V_d/I_d$ yields

$$R_d = V_d/I_d = R_{L-,L+} - R_{L-,R+}. \tag{41}$$

Figure 5 shows the ensemble averaged drag resistance, multiplied by d/W to remove a trivial dependence on the sample width. Analogous to the in-plane and cross conductances discussed in the main text, there is a strong dependence on the choice of the phases $\theta_d(\mathbf{r}_d)$ accumulated along the dislocation lines.

III. PARAMETERS FOR SIMULATION

For the numerical simulation, we chose $W/L = 5$ for the aspect ratio of the slab, we verified that this is large enough that $G_{\parallel,\perp}$ and R_d were proportional and inversely proportional to W, respectively. We divided the slab in transport direction in 10 slices with $2n = 6$ dislocation lines each, so that $d/W = 0.058$. For each slice of width δL, the scattering matrix is calculated with mode cutoff $N = 600$. For the concatenation of scattering matrices of different slices we imposed a smaller cut-off $N_{\mathrm{eff}} = 65$ for the number of modes. We verified that N and N_{eff} are large enough that the results do not depend on these numbers.

IV. DENSITY OF STATES

We discuss how the density of states can be calculated for a periodic array of segments of length L. Equivalently, one may apply "twisted" boundary conditions in the x direction, in which electrons pick up an additional phase $e^{i\kappa_x L}$, κ_x being the crystal momentum, while passing across the "boundary".

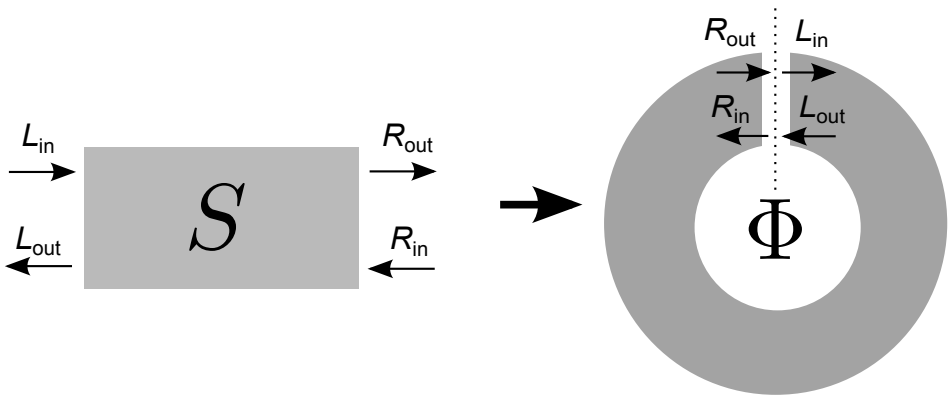

FIG. 6: Calculation of density of states of a periodic array (right) from scattering matrix $S(\varepsilon)$ of an open system (left). The incoming and outcoming states should match, up to a phase factor $\Phi = \kappa_x L$ from the crystal momentum.

The procedure is illustrated in Fig. 6. We start from the scattering matrix of the open slice at energy ε, which we calculate as described previously,

$$\begin{pmatrix} L_{\rm out} \\ R_{\rm out} \end{pmatrix} = \underbrace{\begin{pmatrix} r & t' \\ t & r' \end{pmatrix}}_{S(\varepsilon)} \begin{pmatrix} L_{\rm in} \\ R_{\rm in} \end{pmatrix}.$$

The matching conditions on the in- and outgoing states for a Bloch state with crystal momentum κ_x read

$$\begin{pmatrix} R_{\rm out} \\ L_{\rm out} \end{pmatrix} = \begin{pmatrix} e^{i\kappa_x L} L_{\rm in} \\ e^{-i\kappa_x L} R_{\rm in} \end{pmatrix}$$

which has a non-trivial solution (indicating an eigenstate of the closed system at energy ε) if and only if the matrix

$$S_{\kappa_x}(\varepsilon) \equiv \begin{pmatrix} 0 & e^{-i\kappa_x L} \\ e^{i\kappa_x L} & 0 \end{pmatrix} S(\varepsilon)$$

has a unit eigenvalue. In practice, since the matrix $S_{\kappa_x}(\varepsilon)$ is unitary, we track the eigenvalue phases with varying ε and identify states at energies where a phase crosses zero. The phase $\kappa_x L$ controls the boundary condition in x direction and averaging over $\kappa_x L \in [0, 2\pi]$ thus reduces finite-size effects (we used 80 equally spaced values for $\kappa_x L$ from the interval $[0, 2\pi]$). A similar procedure could be applied with a phase controlling the boundary conditions in transversal direction.

V. ADDITIONAL CHOICES FOR THE PHASES $\theta_{\rm d}(\mathbf{r}_{\rm d})$

We have also studied the cases in which the phases $\theta_{\rm d}(\mathbf{r}_{\rm d})$ randomly fluctuate between the values 0 and π, or between $\pi/2$ and $-\pi/2$. Results for transport properties and for the density of states are shown in Figs. 7 and 8.

[1] J. H. Bardarson, J. Tworzydlo, P. W. Brouwer, and C. W. J. Beenakker, Phys. Rev. Lett. **99**, 106801 (2007).
[2] J. Tworzydlo, B. Trauzettel, M. Titov, A. Rycerz, and C. W. J. Beenakker, Phys. Rev. Lett. **96**, 246802 (2006).

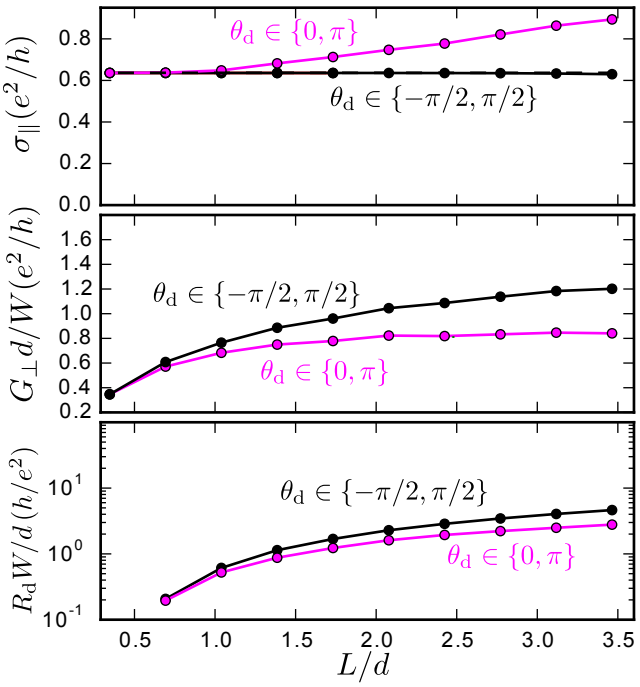

FIG. 7: In-plane conductivity $\sigma_\parallel$ (a), cross conductance $G_\perp$ (b), and drag resistance R_d (c) for a slab of weak-and-strong topological insulator with a concentration $1/d^2$ of randomly placed dislocation lines. The different curves refer to the phases $\theta_d(\mathbf{r}_d)$ randomly chosen from $\{0, \pi\}$ or from $\{-\pi/2, \pi/2\}$, as indicated in the figure. Data points denote an average over 500 disorder realizations, statistical error bars are typically smaller than the markers.

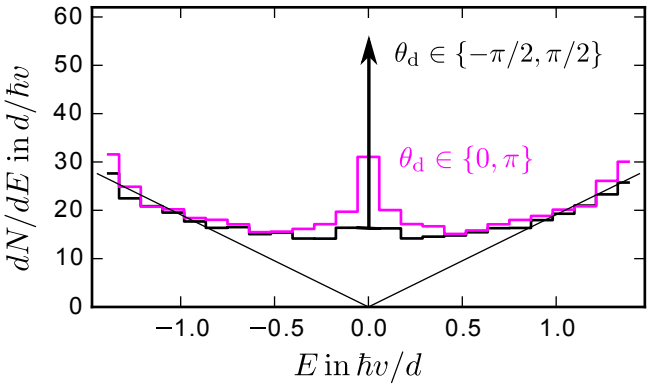

FIG. 8: Density of states dN/dE of a sample with dislocation line density $1/d^2$. The two curves represent are for phases $\theta_d(\mathbf{r}_d)$ randomly chosen from $\{0, \pi\}$ or from $\{-\pi/2, \pi/2\}$, as indicated in the figure. The thin black lines denotes the ideal surface-state density of states without dislocation lines. The arrow denotes a Dirac delta function at zero energy. Data points denote an average over 5 disorder realizations and 80 values of the crystal momentum κ_x.

3 Disorder effects in topological semimetals

3.1 Disorder induced quantum phase transition in Weyl nodes

In chapter 1 we have discussed the basic notions of topological Weyl (semi-)metals. We considered the Bloch-Hamiltonian

$$H_0 = \hbar v \boldsymbol{\sigma} \cdot \mathbf{k} \tag{3.1}$$

and argued for the stability of the degeneracy point with respect to perturbations. However, all of our discussion above including the definition of the topological charge of a Weyl point took place in reciprocal space. We now consider the fate of a Weyl point in a disordered environment, where crystal momentum is not a good quantum number any more. Obviously, to address the stability of the Weyl point, concepts that do not rely on the notion of k-space have to be invoked. One particular simple concept that is well defined in the presence of disorder is the density of states per volume and energy interval. For Equation 3.1 it reads,

$$\rho_0(E) = \frac{E^2}{2\pi^2(\hbar v)^3}. \tag{3.2}$$

The characteristic property of a clean Weyl node is thus a quadratically vanishing density of states around the nodal point. One could ask how disorder affects this density of states profile qualitatively and quantitatively. The earliest study of this problem dates back to the 1980s, when Fradkin [50, 51], based on some type of mean field theory argued for a disorder induced quantum phase transition to occur, the order parameter being $\rho\,(E=0)$: For weak disorder, the situation as in the clean case is maintained $\rho\,(E=0) = 0$, only above a critical disorder strength, $\rho\,(E=0)$ becomes finite. Similar conclusions can be drawn from SCBA [52] or from a RG calculation [53] based on the replicated, disorder averaged action. We do not want to detail on the above approaches but give a simple qualitative argument for the appearance of a quantum phase transition.

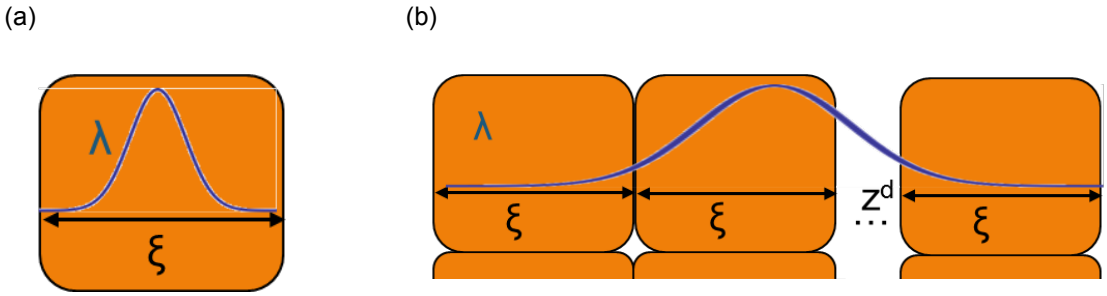

Figure 3.1: Qualitative explanation for the presence of a disorder induced phase transition for Dirac type Hamiltonians. While fitting a Dirac particle wave packet in a single disorder valley (a) might not succeed for weak disorder, the energy conditions can always be matched for larger disorder in less than two spatial dimensions (b).

Let us generalize to d-dimensional Dirac Hamiltonians $E \sim \hbar v k$ subject to disorder with correlation length ξ. The typical peaks and valleys of the disorder potential are extended regions of linear size ξ with finite potential of magnitude $\bar{V} = \hbar v \sqrt{K}/\xi$, found as the standard deviation $\sqrt{\langle V^2(\mathbf{r})\rangle_{dis}}$ from Equation 1.33 up to numerical factors. Let us consider the question if an electron can be trapped in such a volume ξ^d with potential $\bar{V}$. This is the case if for wavelengths λ of order ξ the potential energy exceeds the kinetic energy $\bar{V} > \hbar v/\xi$ equivalent to $K > 1$, see Figure 3.1(a). If the disorder is weaker, $K < 1$, one can ask if we can instead increase the wavelength to $\lambda = z\xi$, $z \in \mathbb{N}$ to cover a larger hypercube, see Figure 3.1(b). The kinetic energy thus decreases to $\hbar v/z\xi$ and the typical average potential energy is the standard deviation of the sum of z^d uncorrelated potential values with standard deviation $\bar{V}$, which is $\bar{V}/\sqrt{z^d}$. The corresponding condition for a bound state is

$$\bar{V}/\sqrt{z^d} > \hbar v/z\xi \tag{3.3}$$

or $\sqrt{K} > z^{d/2-1}$. For $d < 2$, this equation can be solved for any finite K since the right hand side converges to zero as $z \to \infty$. Thus for $d < 2$, arbitrarily small disorder causes a finite density of states. For $d > 2$, the right hand side increases with z and for weak disorder $K < 1$, there are no states at zero energy, in agreement with the assertions for Weyl nodes in $d = 3$ quoted above.

The qualitative argument above obviously lacks some rigor but also the existent analytical calculations are not fully controlled at the nodal point. RG calculations use an epsilon expansion, treating ϵ as a small parameter which is set to unity at the end, the SCBA omits potentially important crossing diagrams as discussed at

the end of chapter 1. Although a numerical calculation for the density of states of a disordered Dirac semimetal existed when we gained interest in the problem [54], internode scattering effects could not be controlled in this simulation.

The first paper of this chapter, reference [3] "*Quantum transport of disordered Weyl semimetals at the nodal point*", DOI: 10.1103/PhysRevLett.113.026602, now trades the density of states perspective on the phase transition in favor for the study of quantum transport properties like conductance and shot noise. We answer the question in which respect these properties of a mesoscopic system signal the predicted quantum criticality. As discussed in chapter 1, for the clean Weyl node, $K = 0$, we have

$$G_0 = 0.11\frac{W^2}{L^2}, \qquad F_0 = 0.574, \tag{3.4}$$

for the conductance and the Fano factor, respectively. We will show in a fully controlled numerical simulation that these ballistic transport properties persist in large enough samples for weak (subcritical) disorder strength. We thus call this transport regime 'pseudoballistic'. Beyond the critical disorder strength, transport characteristics change drastically - diffusive transport with a conductivity σ *increasing* with disorder is observed. We compare our numerical results for the conductivity to predictions of the SCBA and show that it is the omission of the crossing diagrams which leads to a ~50% quantitative error in the diagrammatic analytical calculation. We also explain how the underlying nontrivial Weyl node topology can be in agreement with the previous prediction of vanishing bulk conductivity, $\sigma = 0$, in the pseudoballistic phase.

We emphasize that the results in this chapter, where single, independent Weyl nodes are considered, do not necessarily hold for realistic Weyl semimetals which harbor at least a pair of Weyl nodes. In the presence of disorder, Weyl nodes can only be considered as independent if the disorder scattering does not couple quasiparticles from different Weyl nodes. Weyl nodes separated a distance Δk in reciprocal space are connected by a scattering rate proportional to the Fourier transform amplitude of the disorder correlator at momentum Δk. If the disorder potential varies on a typical length scale $\xi \gg 1/\Delta k$, the effective internode scattering is negligible. Thus our results should apply to Weyl semimetals with Weyl nodes distant in k-space and subject to a smooth disorder potential.

Moreover, some of our results only apply in the case of chemical potential positioned strictly at the Weyl node. None of the Weyl semimetal materials available to date fulfill this property, although chances to realize ideal materials are growing [55]. However, for finite chemical potential μ^* we predict a crossover lengthscale $L^* \sim \mu^*/\hbar v$ below which the system properties can be well approximated by $\mu = 0$. For realistic material parameters μ^* and v, crossover lengthscales L^* can be well

in the range of microns, feasible for experiments.

Quantum Transport of Disordered Weyl Semimetals at the Nodal Point

Björn Sbierski, Gregor Pohl, Emil J. Bergholtz, and Piet W. Brouwer
Dahlem Center for Complex Quantum Systems and Institut für Theoretische Physik, Freie Universität Berlin, D-14195 Berlin, Germany

(Received 26 February 2014; revised manuscript received 24 June 2014; published 11 July 2014)

Weyl semimetals are paradigmatic topological gapless phases in three dimensions. We here address the effect of disorder on charge transport in Weyl semimetals. For a single Weyl node with energy at the degeneracy point and without interactions, theory predicts the existence of a critical disorder strength beyond which the density of states takes on a nonzero value. Predictions for the conductivity are divergent, however. In this work, we present a numerical study of transport properties for a disordered Weyl cone at zero energy. For weak disorder, our results are consistent with a renormalization group flow towards an attractive pseudoballistic fixed point with zero conductivity and a scale-independent conductance; for stronger disorder, diffusive behavior is reached. We identify the Fano factor as a signature that discriminates between these two regimes.

DOI: 10.1103/PhysRevLett.113.026602 PACS numbers: 72.10.Bg, 03.65.Vf, 05.60.Gg, 72.10.Fk

Introduction.—Topological considerations not only can be used to describe and classify band insulators and superconductors [1,2], they were also found to apply to gapless phases of matter [3–10]. Perhaps the best known example of a topologically nontrivial gapless band structure is that of graphene [11], which has four topologically protected band touchings. The paradigmatic example of a topological gapless phase in three dimensions is the Weyl semimetal [12–14], which features pairs of topologically protected gap closing points in its Brillouin zone. The dispersion in the vicinity of a single isotropic nodal point can be described by the effective Hamiltonian

$$H_0(\mathbf{k}) = \pm\hbar v \boldsymbol{\sigma}\cdot\mathbf{k}, \tag{1}$$

where v is the Fermi velocity, $\boldsymbol{\sigma}$ is the vector of Pauli matrices, $\pm$ denotes the chirality, and $\mathbf{k}$ measures the Bloch wave vector relative to the momentum in the Brillouin zone at which the gap closing appears.

Weyl semimetals have attracted considerable attention due to the prediction of protected surface states with a Fermi arc [13] and the chiral anomaly in an electromagnetic response [15]. An ideal Weyl semimetal with Fermi energy at the Weyl point $\varepsilon = 0$ has a vanishing conductivity σ, but a finite conductance [16], making it neither conducting nor insulating. The excitement is further fueled by the existence of concrete theoretical proposals for material candidates for Weyl semimetals, both in the solid state [13,17,18] and in cold atom systems [19], as well as the experimental identification of "Dirac semimetals" [20–22], which have a pair of Weyl nodes forced to overlap by time-reversal and inversion symmetry. Although spectroscopic confirmation of a Weyl node in a real material is still lacking, magneto-transport signatures consistent with Weyl nodes were reported for BiSb [23].

An important question that concerns the comparison of theory and experimental realizations is about the stability of the Weyl nodes to the presence of disorder [24]. This question is of particular fundamental interest if the disorder is sufficiently smooth that scattering between different Weyl nodes is avoided, since disorder that does not satisfy this condition immediately removes any topological protection and leads to a trivial gapping of the spectrum and/or localization of the wave functions.

In the theoretical literature, the study of the effect of disorder on a single Weyl node, without the inclusion of electron-electron interactions, goes back to the mid 1980s [25,26]. Far away from the Weyl point, the expected behavior resembles that of normal metals: Disorder leads to diffusive dynamics, with a conductivity σ that decreases with increasing disorder strength. However, unlike a normal metal, a Weyl semimetal has no transition into an Anderson-localized phase in the limit of strong disorder [27]. Exactly at the Weyl point $\varepsilon = 0$ a completely different picture emerges: There is consensus that weak disorder is irrelevant [25,26,28,29], so that the vanishing density of states $\nu(\varepsilon) \propto \varepsilon^2$ of the Hamiltonian, Eq. (1), is maintained at finite disorder strength [30,31], up to possible rare-region effects [32]. For stronger disorder, a quantum phase transition takes place, beyond which $\nu(0)$ is finite. There is no consensus for the implications of this scenario for the conductivity σ, however. Using the self-consistent Born approximation (SCBA), Ominato and Koshino [31] find $\sigma = 0$ up to the critical disorder strength, and a finite conductivity that increases for stronger disorder, whereas the renormalization group approach of Ref. [29] gives a finite conductivity for subcritical disorder strengths. Boltzmann theory also gives a Weyl-point conductivity that is a decreasing function of disorder strength, but there is no critical disorder strength and σ is finite throughout [28,31,33].

Remarkably, the question about the effect of disorder on a single Weyl node has never been put to the test numerically. Recently, similar physics has been investigated for a disordered Dirac semimetal employing diagonalization of a large tight binding model [34]. The extension of these results to a Weyl semimetal is problematic, however, because any tight binding model with a Weyl node inevitably comes with its opposite-chirality partner node [35], coupling to which cannot be fully avoided. Yet, resorting to a numerical test is particularly relevant in the present case, because none of the theoretical methods applied in the analytical theory cited above are fully controlled at the Weyl point $\varepsilon = 0$ (see Ref. [29] for a critical discussion).

In this Letter, we report numerical calculations of the transport properties of a single Weyl node in the presence of a random potential. We limit ourselves to transport at the Weyl point $\varepsilon = 0$, which is the energy at which the differences between a Weyl semimetal and a normal metal are most pronounced. The focus on the nodal point is not entirely academic: In contrast to the two-dimensional case (graphene or surface states of topological insulators), where unintended doping generically shifts the chemical potential away from the nodal point, in the bulk of three-dimensional Weyl semimetals $\varepsilon = 0$ can be expected from the stoichiometric filling of the energy bands [30].

Our results for the conductivity are qualitatively similar to the predictions of the SCBA [31], although quantitatively the numerical results for the critical disorder strength and for the conductivity approximately differ by a factor of 2. In the weak-disorder phase the system is better characterized by its conductance, which is finite, than by its conductivity, which is zero within the accuracy of our calculations. A transport signature that is nonzero in both phases is the Fano factor F, the ratio of the shot-noise power and the conductance, which we show to be an excellent indicator to discriminate between the pseudoballistic transport of the weak-disorder phase and the diffusive transport of the strong-disorder phase.

Model and numerical method.—Our numerical procedure closely follows Refs. [36,37], which considered the effect of disorder on the conductivity of graphene. We consider a Weyl semimetal of length $0 < x < L$ and transverse dimensions $0 < y, z < W$ with Hamiltonian

$$H = H_0 + U(\mathbf{r}), \tag{2}$$

where $U(\mathbf{r})$ is a Gaussian random potential with zero mean $\langle U_{\mathbf{q}} \rangle = 0$ and fluctuations

$$\langle U_{\mathbf{q}} U^*_{\mathbf{q}'} \rangle = \frac{K\xi\hbar^2 v^2}{W^2 L} e^{-q^2\xi^2/2} \delta_{\mathbf{q},\mathbf{q}'}, \tag{3}$$

where ξ is the correlation length and K the dimensionless disorder strength. A similar random potential has been used in studies of the Dirac equation in two dimensions [36]. For $x < 0$ and $x > L$ the Weyl semimetal is connected to ideal leads, which we model as Weyl semimetals with Hamiltonian $H_0 + V$, taking the limit $V \to -\infty$ [38]. We numerically compute the transmission matrix t at zero energy and determine the zero-temperature conductance using the Landauer formula $G(L, W) = (e^2/h)\mathrm{tr}tt^\dagger$ and the Fano factor $F(L) = \mathrm{tr}[tt^\dagger(1 - tt^\dagger)]/\mathrm{tr}tt^\dagger$. To quantize transverse momenta, we apply periodic or antiperiodic boundary conditions in the y and z directions, and truncate at $|q_y|, |q_z| \le 2M/\xi$, where we verified that the results do not depend on the cutoff M. To ensure bulk behavior, the width W is taken large enough that the results do not depend on the boundary conditions and the scaling $G \propto W^2$, F independent of W, holds.

Pseudoballistic regime.—For the low-disorder regime, we rescale the calculated conductance $G(L, W)$ to find the dimensionless conductance $g(L)$ of a cube with linear dimension L,

$$G(L, W) = \frac{e^2 W^2}{hL^2} g(L). \tag{4}$$

In the absence of disorder, g and the Fano factor F are independent of L [16], taking the values

$$g_0 = \frac{\ln 2}{2\pi} c, \quad F_0 = \frac{1}{3} + \frac{1}{6\ln 2} \approx 0.574, \tag{5}$$

with c a numerical factor that takes the value $c = 1$ (so that $g_0 \approx 0.110$) for an isotropic Weyl cone. The results of numerical calculations of $g(L)$ and $F(L)$ for disorder strengths $K = 1$, 2, and 3 are shown in Fig. 1. The numerical data show that the presence of the random potential $U(\mathbf{r})$ leads to a bulk conductance g that is always larger than the pseudoballistic value g_0, but also that the conductance $g(L)$ is a bounded function of L and monotonically decreases in the large-L limit. For the system sizes within our reach this decrease is most pronounced for weak disorder ($K = 1$), and less pronounced for stronger disorder ($K = 3$), which is consistent with the theoretical expectation that weak disorder is an irrelevant perturbation at $\varepsilon = 0$ [28,29]. The fact that $g(L)$ remains bounded as a function of L is consistent with a vanishing conductivity $\sigma = 0$. [A finite conductivity would correspond to $g(L) \propto L$; see the inset in Fig. 1.] The Fano factor F takes the pseudoballistic value F_0 for all system sizes considered. We postpone a further discussion of these results until the end of this article.

Diffusive regime.—For stronger disorder, the conductivity σ becomes finite. Although σ can, in principle, be obtained from the conductance using the relation $G(L, W) = \sigma W^2/L$, we employ a slightly different procedure to obtain σ from the numerically calculated conductance $G(L, W)$, in order to eliminate the effect of a finite contact resistance. Figure 2 shows the resistance

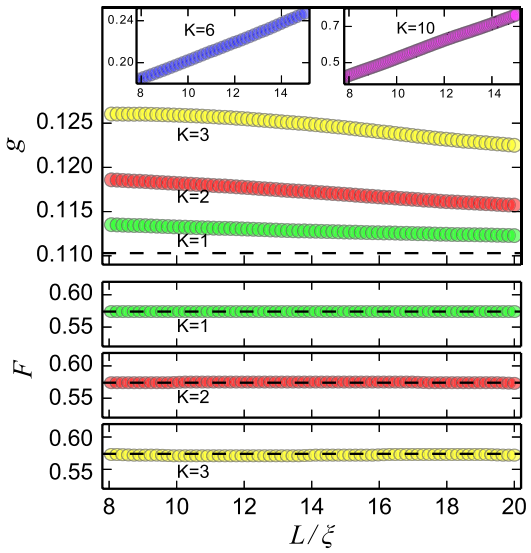

FIG. 1 (color online). Dimensionless conductance g referred to a cubic sample of size L (top) and Fano factor F (bottom) for a single Weyl cone with a random potential for disorder strengths $K = 1$, 2, and 3 in the pseudoballistic regime. The data represent a disorder average over at least 10 realizations. The dashed lines refer to the clean limits g_0 and F_0 for an isotropic Weyl cone ($c = 1$). For comparison, diffusive scaling of g for $K = 6$, 10 is shown in the insets.

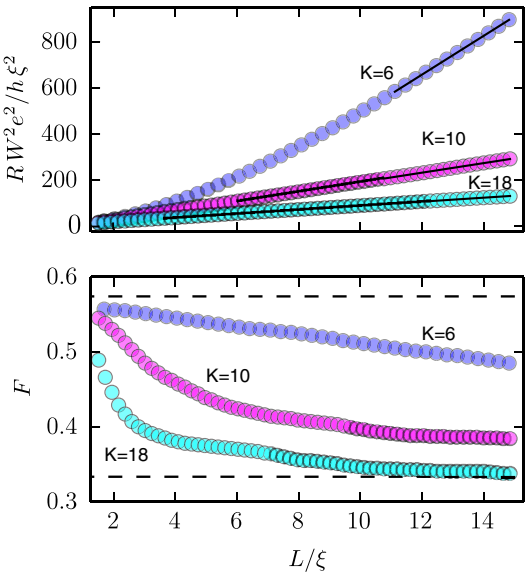

FIG. 2 (color online). Resistance R (top) and Fano factor F (bottom) for a single Weyl cone vs system length L, for disorder strengths $K = 6$, 10, and 18. The thin solid lines indicate the linear fit for the conductivity σ. The dashed lines refer to the pseudoballistic and diffusive limits for the Fano factor F. The data represent a disorder average over at least 100 realizations.

$R(L, W) = 1/G(L, W)$ and the Fano factor $F(L)$ as a function of length L, for disorder strengths $K = 6$, 10, and 18. In the diffusive regime, one expects $R(L, W) \propto L/W^2\sigma$, so that the conductivity can be calculated as $\sigma^{-1} = W^2\partial R/\partial L$. We indeed observe a linear R vs L dependence for sufficiently large L. The Fano factor F takes the diffusive value $F = 1/3$ for large L for the stronger disorder strengths such as $K = 18$. For $K = 6$ and $K = 10$, the Fano factor F is below the pseudoballistic limit and decreases with increasing L, but no limiting value could be determined for the system sizes available in our calculations. The dependence of the conductivity σ on disorder strength K is summarized in Fig. 3. We estimate that the conductivity is nonzero above a critical disorder $K_c \approx 5$, the behavior for K just above K_c being consistent with a linear increase $\propto K - K_c$ [26,31,39]. Finite-size effects prohibit a more accurate determination of the critical disorder strength. Although we adopted the expression "critical disorder strength," we note that our numerical analysis does not allow us to determine the precise nature of the transition. In passing, we also note that the conductance distribution is widest around K_c (data not shown), a behavior well known from the three-dimensional Anderson phase transition [40].

A recent work by Ominato and Koshino [31] calculates the Weyl-point conductivity σ using the SCBA but without further approximations, employing a correlated disorder potential compatible with the random potential used in the present numerical simulation. Relating the impurity model of Ref. [31] to our Gaussian model we find a theoretical value $K_c^{\mathrm{SCBA}} \approx 11.3$ and a conductivity as shown by the dashed line Fig. 3 [41]. Both the value of K_c^{SCBA} and the slope of the SCBA conductivity vs disorder strength K are roughly off by a factor of 2 from the numerical results.

In order to understand the quantitative failure of the SCBA, we have analyzed the corrections to the SCBA result for the self-energy $\Sigma(\mathbf{k}, \omega)$, which is related to the single-particle Green function $\mathcal{G}(\mathbf{k}, \omega)$ through the standard relation $\mathcal{G}(\mathbf{k}, \omega) = [\omega - H_0 - \Sigma(\mathbf{k}, \omega)]^{-1}$. The diagrammatic expression for $\Sigma(\mathbf{k}, \omega)$ in the SCBA is shown in Fig. 4(a), where the double lines denote the single-particle

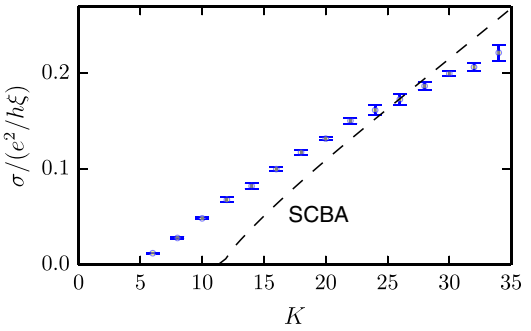

FIG. 3 (color online). Conductivity σ for the disordered Weyl cone as a function of the disorder strength K. The data represent a disorder average over at least 50 disorder realizations. The dashed line refers to the SCBA theory of Ref. [31].

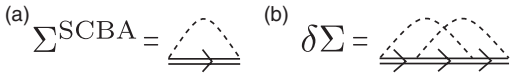

FIG. 4. Diagrammatic representation of the SCBA self-energy Σ^{SCBA} (a) and the leading correction $\delta\Sigma$ (b). The double solid lines denote the SCBA propagator; dashed lines are disorder correlators.

Green function $\mathcal{G}$ with Σ replaced by Σ^{SCBA}. Figure 4(b) contains the leading correction $\delta\Sigma$ to Σ^{SCBA}. The consistency of the SCBA requires that $\delta\Sigma$ is parametrically smaller than Σ^{SCBA}. Indeed, for a standard disordered metal one finds $\delta\Sigma/\Sigma^{\mathrm{SCBA}} = \mathcal{O}(1/k_F l)$ [42], where k_F is the Fermi wave vector and l the mean free path.

For the Weyl semimetal at zero energy one has $k_F = 0$ and this standard argument does not apply. We have calculated the leading correction $\delta\Sigma$ at $k = 0$ and $\omega = 0$ using a simplified model for the disorder potential [31], in which the Gaussian correlator (3) is replaced by a cutoff at $q = 2/\xi$,

$$\langle U_{\mathbf{q}} U^*_{\mathbf{q}'} \rangle = \frac{K'\xi\hbar^2 v^2}{W^2 L}\Theta(2/\xi - q)\delta_{\mathbf{q},\mathbf{q}'}. \tag{6}$$

In this simplified model, one has the critical disorder strength $K_c{}' = \pi^2$ and the SCBA self-energy $\Sigma(0,0)^{\mathrm{SCBA}} = (4\pi i\hbar v/\xi)(1/K' - 1/K_c{}')\Theta(K' - K_c{}')$ [31]. The calculation of the diagram of Fig. 4(b) for K' close to the critical disorder strength $K_c{}'$ then gives [43]

$$\frac{\delta\Sigma(0,0)}{\Sigma(0,0)^{\mathrm{SCBA}}} \simeq 0.62 + 11\left(\frac{1}{K_c{}'} - \frac{1}{K'}\right), \tag{7}$$

which is not parametrically small. Since the simplified model, Eq. (6), does not qualitatively differ from the Gaussian model used in the numerical calculations [31], we expect that this result carries over to that case, too.

Discussion.—In the framework of Drude transport theory for normal metals, the quasiparticles at the Fermi energy are endowed with a mean free path, which becomes shorter if the disorder becomes stronger. At the same time, the presence of a random impurity potential has a negligible effect on the density of states. The result is a conductivity that decreases upon increasing the disorder strength. In contrast, for a Weyl node at the degeneracy point it is the disorder which generates the density of states [25,26,28–31], a finite density of states appearing only above a certain critical disorder strength. As a result of this vastly different physical mechanism, a Weyl node at the degeneracy point shows behavior opposite to that of a normal metal: Increasing disorder beyond the critical disorder strength leads to an increase of the conductivity. This remarkable theoretical prediction has been confirmed in our numerical calculations.

The increase in conductivity with disorder is reminiscent of the two-dimensional Dirac Hamiltonian $H_0^{2d} \propto v(k_x\sigma_x + k_y\sigma_y)$, for which the conductivity σ was also found to be an increasing function of disorder strength [36,37,44]. A fundamental difference with H_0^{2d} is, however, that H_0^{2d} has a finite conductivity for all disorder strengths, whereas the Weyl semimetal at the degeneracy point requires a minimum disorder strength for diffusive behavior to set in.

For the two-dimensional Dirac Hamiltonian, the inverted dependence of conductivity on disorder strength was found to be related to the fact that H_0^{2d} (with a disorder term but without the condition that the disorder be smooth, because of the absence of other Dirac nodes) is the surface theory of a three-dimensional time-reversal invariant topological insulator [27]. Similarly, the surface theory of a hypothetical four-dimensional topological insulator is described by the Hamiltonian H_0 of Eq. (1). Thus, it is expected on general grounds that H_0 evades localization [27]. Our numerical results are consistent with this expectation. Indeed, although the conductivity σ vanishes in the weak-disorder regime, the conductance g remains finite. It is a finite conductance, not a finite conductivity, which is the proper signature of the absence of localization [45].

There is a subtle but important difference between the numerical calculations we performed here and the analytical theories of the conductivity cited in the Introduction: In our calculations, the conductivity σ is obtained from the conductance G of a finite-size sample, for which the energy ε is set to zero at the beginning of the calculation. In contrast, in the renormalization group, SCBA, and Boltzmann theories, the sample size is infinite and the limit $\varepsilon \to 0$ is taken at the end of the calculation [28–31]. This different order of limits may be responsible for the qualitative difference with Refs. [28–30], which predict a finite conductivity in the limit $\varepsilon \to 0$. Which order of limits is relevant for experiments depends on the competition between the finite sample size L and the finite temperature or doping [29,30]—although the latter is expected to be intrinsically small. The order of the limits $\varepsilon \to 0$ and $L \to \infty$ does not affect the comparison to the SCBA, because this theory predicts $\sigma = 0$ even if the limit $\varepsilon \to 0$ is taken at the end of the calculation [31]. Above the critical disorder strength, the self-energy at $\varepsilon = 0$ acquires a nonzero (imaginary) value and the order of limits issue is no longer relevant.

Our numerical calculations have shown that the conductance g and the Fano factor F contain important additional information that is not contained in the conductivity σ. This is particularly relevant for the pseudoballistic weak-disorder regime, where σ vanishes, whereas g and F take on nonzero values. A three-dimensional phase with a finite scale-independent bulk conductance is known from the Anderson metal-insulator transition, where it occurs at the critical disorder strength. A crucial difference of the

pseudoballistic phase at the Weyl point is that its scale-independent conductance represents an attractive fixed point, which requires no fine-tuning of disorder strength.

We acknowledge helpful discussions with Georg Schwiete, Martin Schneider, Sergey Syzranov, Leo Radzihovsky, Victor Gurarie, and we thank Jörg Behrmann for support with the computations. Financial support was granted by the Helmholtz Virtual Institute "New states of matter and their excitations," by the Alexander von Humboldt Foundation in the framework of the Alexander von Humboldt Professorship, endowed by the Federal Ministry of Education and Research, and by DFG's Emmy Noether program (BE 5233/1-1).

[1] M. Z. Hasan and C. L. Kane, Rev. Mod. Phys. **82**, 3045 (2010).
[2] B. A. Bernevig, *Topological Insulators and Topological Superconductors* (Princeton University Press, Princeton, 2013).
[3] X. G. Wen and A. Zee, Phys. Rev. B **66**, 235110 (2002).
[4] P. Hořava, Phys. Rev. Lett. **95**, 016405 (2005).
[5] M. Sato, Phys. Rev. B **73**, 214502 (2006).
[6] B. Béri, Phys. Rev. B **81**, 134515 (2010).
[7] G. Volovik, JETP Lett. **93**, 66 (2011).
[8] D. Bernard, E.-A. Kim, and A. LeClair, Phys. Rev. B **86**, 205116 (2012).
[9] Y. X. Zhao and Z. D. Wang, Phys. Rev. Lett. **110**, 240404 (2013).
[10] S. Matsuura, P.-Y. Chang, A. P. Schnyder, and S. Ryu, New J. Phys. **15**, 065001 (2013).
[11] P. R. Wallace, Phys. Rev. **71**, 622 (1947).
[12] S. Murakami, New J. Phys. **9**, 356 (2007).
[13] X. Wan, A. M. Turner, A. Vishwanath, and S. Y. Savrasov, Phys. Rev. B **83**, 205101 (2011).
[14] For a review see P. Hosur and X. Qi, C.R. Phys. **14**, 857 (2013).
[15] P. Goswami and S. Tewari, Phys. Rev. B **88**, 245107 (2013); M. M. Vazifeh and M. Franz, Phys. Rev. Lett. **111**, 027201 (2013).
[16] P. Baireuther, J. M. Edge, I. C. Fulga, C. W. J. Beenakker, and J. Tworzydlo, Phys. Rev. B **89**, 035410 (2014).
[17] A. A. Burkov and L. Balents, Phys. Rev. Lett. **107**, 127205 (2011).
[18] D. Bulmash, C.-X. Liu, and X.-L. Qi, Phys. Rev. B **89**, 081106 (2014).
[19] Y. Xu, R.-L. Chu, and C. Zhang, Phys. Rev. Lett. **112**, 136402 (2014).
[20] M. Neupane *et al.*, Nat. Commun. **5**, 3786 (2014).
[21] S. Borisenko and Q. Gibson, arXiv:1309.7978.
[22] Z. K. Liu, B. Zhou, Y. Zhang, Z. J. Wang, H. M. Weng, D. Prabhakaran, S.-K. Mo, Z. X. Shen, Z. Fang, X. Dai, Z. Hussain, and Y. L. Chen, Science **343**, 864 (2014).
[23] H.-J. Kim, K.-S. Kim, J.-F. Wang, M. Sasaki, N. Satoh, A. Ohnishi, M. Kitaura, M. Yang, and L. Li, Phys. Rev. Lett. **111**, 246603 (2013).
[24] The effect of a single impurity on the electronic structure of a Weyl node has been studied recently in Z. Huang, T. Das, A. Balatsky, and D. Arovas, Phys. Rev. B **87**, 155123 (2013).
[25] E. Fradkin, Phys. Rev. B **33**, 3257 (1986).
[26] E. Fradkin, Phys. Rev. B **33**, 3263 (1986).
[27] S. Ryu, A. P. Schnyder, A. Furusaki, and A. W. W. Ludwig, New J. Phys. **12**, 065010 (2010).
[28] A. A. Burkov, M. D. Hook, and L. Balents, Phys. Rev. B **84**, 235126 (2011).
[29] S. V. Syzranov, L. Radzihovsky, and V. Gurarie, arXiv:1402.3737.
[30] R. R. Biswas and S. Ryu, Phys. Rev. B **89**, 014205 (2014).
[31] Y. Ominato and M. Koshino, Phys. Rev. B **89**, 054202 (2014).
[32] R. Nandkishore, D. Huse, and S. Sondhi, Phys. Rev. B **89**, 245110 (2014).
[33] P. Hosur, S. A. Parameswaran, and A. Vishwanath, Phys. Rev. Lett. **108**, 046602 (2012).
[34] K. Kobayashi, T. Ohtsuki, K.-I. Imura, and I. F. Herbut, Phys. Rev. Lett. **112**, 016402 (2014).
[35] H. Nielsen and M. Ninomiya, Nucl. Phys. **B185**, 20 (1981).
[36] J. H. Bardarson, J. Tworzydlo, P. W. Brouwer, and C. W. J. Beenakker, Phys. Rev. Lett. **99**, 106801 (2007).
[37] S. Adam, P. W. Brouwer, and S. Das Sarma, Phys. Rev. B **79**, 201404 (2009).
[38] J. Tworzydlo, B. Trauzettel, M. Titov, A. Rycerz, and C. W. J. Beenakker, Phys. Rev. Lett. **96**, 246802 (2006).
[39] P. Goswami and S. Chakravarty, Phys. Rev. Lett. **107**, 196803 (2011).
[40] K. Slevin and T. Ohtsuki, Phys. Rev. Lett. **78**, 4083 (1997).
[41] The theory of Ref. [31] can be applied to our calculations by making the substitutions $d_0 \leftrightarrow \xi$ and $W \leftrightarrow K/2\pi$.
[42] J. Rammer, *Quantum Transport Theory* (Perseus Books, New York, 1998).
[43] See Supplemental Material at http://link.aps.org/supplemental/10.1103/PhysRevLett.113.026602 for details of this calculation.
[44] S. Das Sarma, E. H. Hwang, and Q. Li, Phys. Rev. B **85**, 195451 (2012).
[45] Y. Imry, *Introduction to Mesoscopic Physics* (Oxford University Press, New York, 2002).

Supplemental Material: Quantum transport of disordered Weyl semimetals at the nodal point

LEADING CORRECTION TO SCBA SELF ENERGY

We compute the leading correction $\delta\Sigma$ to the SCBA self energy $\Sigma^{\rm SCBA}$ at zero momentum $\mathbf{k}=0$ and zero energy $\omega=0$. The diagrammatic representation for the correction $\delta\Sigma(\mathbf{k},\omega)$ is shown in Fig. 4(b) in the main text,

$$\delta\Sigma(\mathbf{k},\omega)=\sum_{\mathbf{k}_1,\mathbf{k}_2}\mathcal{G}(\mathbf{k}+\mathbf{k}_1,\omega)\mathcal{G}(\mathbf{k}+\mathbf{k}_1+\mathbf{k}_2,\omega)\mathcal{G}(\mathbf{k}+\mathbf{k}_2,\omega)\langle|U_{\mathbf{k}_1}|^2\rangle\langle|U_{\mathbf{k}_2}|^2\rangle, \tag{1}$$

where $\mathcal{G}(\mathbf{k},\omega)=[\omega-H_0-\Sigma(\mathbf{k},\omega)^{\rm SCBA}]^{-1}$ is the SCBA propagator and U the disorder potential. Taking the disorder correlator $\langle|U_{\mathbf{k}}|^2\rangle$ from Eq. (6) of the main text, setting $\mathbf{k}=0$, $\omega=0$, and replacing the summation over $\mathbf{k}_1$ and $\mathbf{k}_2$ by an integration one finds

$$\delta\Sigma(0,0)=K'^2\xi^2\,(\hbar v)^4\int_{k_1<2/\xi}\frac{d\mathbf{k}_1}{(2\pi)^3}\int_{k_2<2/\xi}\frac{d\mathbf{k}_2}{(2\pi)^3}\mathcal{G}(\mathbf{k}_2,0)\mathcal{G}(\mathbf{k}_1+\mathbf{k}_2,0)\mathcal{G}(\mathbf{k}_1,0).$$

Employing the identity $(a-\mathbf{b}\cdot\boldsymbol{\sigma})^{-1}=(a+\mathbf{b}\cdot\boldsymbol{\sigma})/(a^2-|\mathbf{b}|^2)$ and substituting [1]

$$\Sigma(0,0)^{\rm SCBA}=\frac{4\pi i\hbar v}{\tilde{K}'\xi},\quad \tilde{K}'=\frac{1}{1/K'-1/K'_{\rm c}}, \tag{2}$$

for disorder strength $K'>K'_{\rm c}$, one finds that (for a positive helicity Weyl node) the single-particle propagator $\mathcal{G}$ is given by the expression

$$\mathcal{G}(\mathbf{k},0)=\left(\frac{\xi}{2\hbar v}\right)\frac{(2\pi/\tilde{K}')i-(\xi/2)\mathbf{k}\cdot\boldsymbol{\sigma}}{(2\pi/\tilde{K}')^2+(\xi/2)^2k^2}. \tag{3}$$

Switching to the dimensionless variables $\mathbf{x}_{1,2}=\mathbf{k}_{1,2}\xi/2$ we arrive at

$$\begin{aligned}\frac{\delta\Sigma(0,0)}{\Sigma(0,0)^{\rm SCBA}}=&\frac{K'^2\tilde{K}'}{32\pi^7 i}\\&\times\int_{x_1<1}d\mathbf{x}_1\int_{x_2<1}d\mathbf{x}_2\left(\frac{2\pi i/\tilde{K}'-\mathbf{x}_2\cdot\boldsymbol{\sigma}}{(2\pi/\tilde{K}')^2+x_2^2}\right)\left(\frac{2\pi i/\tilde{K}'-(\mathbf{x}_1+\mathbf{x}_2)\cdot\boldsymbol{\sigma}}{(2\pi/\tilde{K}')^2+|\mathbf{x}_1+\mathbf{x}_2|^2}\right)\left(\frac{2\pi i/\tilde{K}'-\mathbf{x}_1\cdot\boldsymbol{\sigma}}{(2\pi/\tilde{K}')^2+x_1^2}\right).\end{aligned} \tag{4}$$

Finally, after introducing polar coordinates for the integrations over $\mathbf{x}_1$ and $\mathbf{x}_2$ one finds after some standard manipulations

$$\begin{aligned}\frac{\delta\Sigma(0,0)}{\Sigma(0,0)^{\rm SCBA}}=&\frac{K'^2}{4\pi^4}\int_0^1dx_1\int_0^1dx_2\frac{x_1^2x_2^2}{[(2\pi/\tilde{K}')^2+x_1^2][(2\pi/\tilde{K}')^2+x_2^2]}\left\{6-\left[\frac{5}{2}(2\pi/\tilde{K}')^2+\frac{1}{2}(x_1^2+x_2^2)\right]\right.\\&\left.\times\int_0^\pi d\zeta\int_\zeta^\pi d\theta\frac{\cos\zeta-\cos\theta}{\sqrt{[(2\pi/\tilde{K}')^2+x_1^2+x_2^2+2x_1x_2\cos\zeta][(2\pi/\tilde{K}')^2+x_1^2+x_2^2+2x_1x_2\cos\theta]}}\right\}.\end{aligned} \tag{5}$$

Numerical evaluation of the fourfold integral for K' in the vicinity of the critical disorder strength $K'_{\rm c}$ then results in the estimate (7) quoted in the main text.

[1] Y. Ominato and M. Koshino , Phys. Rev. B 89 054202 (2014).

3.2 Critical exponents for a disordered three-dimensional Weyl node

After having discussed the nature of the weak and strong disorder phase of the Weyl node in some detail from the quantum transport perspective, we now turn our attention to the critical point that separates the two phases. In the modern theory of continuous phase transitions building on RG ideas, a variety of microscopic models can have critical behavior that share the same exponents for its associated power laws. If this is the case, these models are said to be in the same universality class [56]. The universality class is usually determined by the physical dimension of the model and its specific symmetries.

The paper below, reference [4] titled "*Quantum critical exponents for a disordered three-dimensional Weyl node*", DOI: 10.1103/PhysRevB.92.115145, is devoted to the study of the universal properties belonging to the disorder induced quantum phase transition in Weyl nodes. For that purpose, we tune the disorder strength K and energy ε in the vicinity of the critical point at $K = K_c$ and $\varepsilon = 0$ and fit numerically obtained transport properties of these close-to-critical samples to scaling functions that involve the correlation length and dynamical exponent ν and z. In detail, to assess ν, we study the interplay of a finite system size L and the correlation length ζ (that diverges at the critical point as $(K - K_c)^{-\nu}$) by a method termed finite-size scaling. A similar analysis, using finite energies but (practically) infinite system size can be repeated to obtain z.

Previous approaches to the problem (see e.g. [54]), studied the density of states as a function of K and ε. Due to inherent difficulties of the method employed, the estimates for ν and z had large errors, partially propagating from uncertainty in the value of K_c. Instead, we devise a novel scheme that allows to employ the conductance and Fano factor for the scaling analysis. Our efficient and reliable scattering matrix based computational scheme described above allows unprecedented precision for estimates of the critical exponents. The paper concludes that the disorder induced critical point is of a novel and so far unknown universality class.

PHYSICAL REVIEW B **92**, 115145 (2015)

Quantum critical exponents for a disordered three-dimensional Weyl node

Björn Sbierski, Emil J. Bergholtz, and Piet W. Brouwer
Dahlem Center for Complex Quantum Systems and Institut für Theoretische Physik, Freie Universität Berlin, D-14195, Berlin, Germany
(Received 27 May 2015; published 24 September 2015)

Three-dimensional Dirac and Weyl semimetals exhibit a disorder-induced quantum phase transition between a semimetallic phase at weak disorder and a diffusive-metallic phase at strong disorder. Despite considerable effort, both numerically and analytically, the critical exponents ν and z of this phase transition are not known precisely. Here we report a numerical calculation of the critical exponent $\nu = 1.47 \pm 0.03$ using a minimal single-Weyl node model and a finite-size scaling analysis of conductance. Our high-precision numerical value for ν is incompatible with previous numerical studies on tight-binding models and with one- and two-loop calculations in an ϵ-expansion scheme. We further obtain $z = 1.49 \pm 0.02$ from the scaling of the conductivity with chemical potential.

DOI: 10.1103/PhysRevB.92.115145 PACS number(s): 72.10.Bg, 03.65.Vf, 05.60.Gg, 72.10.Fk

Introduction. Materials with an electronic band structure dispersing linearly from a Fermi point are among the driving themes in contemporary condensed matter physics [1–3]. After the experimental verification of such a Dirac-type band structure in single-layer graphene [4], the focus has now turned to three-dimensional materials. The compounds Na_3Bi and Cd_3As_2 have been confirmed as Dirac semimetals [5–9]. In materials that break either time- or space-inversion symmetry, the twofold band degeneracy of Dirac semimetals is lifted and the resulting phase is termed Weyl semimetal. The noncentrosymmetric compounds TaAs and NbAs have recently proven experimentally to harbor such Weyl nodes in their band structures [10–12]. Similar band structures have been achieved in a photonic crystal realization in Ref. [13].

Theoretical work accompanied and, in part, preceded the recent experiments. Beyond the single-particle picture, Coulomb interactions were argued to be marginally irrelevant in the renormalization group (RG) sense due to the vanishing density of states at the Fermi point [14,15]. Quenched disorder, however, inevitably present in realistic materials, is a much more subtle issue. Dating back to work from the 1980s [16,17], the presence of a disorder-induced quantum phase transition is by now firmly established analytically [14,18–20] and numerically [21–26]. In the weak-disorder phase, the random potential is irrelevant in an RG sense. Thus, for large system sizes and low temperatures, a weakly disordered system qualitatively behaves as a clean system with renormalized Fermi velocity. This leads to a number of experimentally important predictions for weak disorder, such as quadratically vanishing density of states [20,22] or pseudoballistic charge transport [21] at the nodal point. In contrast, for strong disorder one finds a metallic phase with finite density of states at the Fermi energy and diffusive transport characteristics [21,27].

Signatures of the disorder-induced quantum criticality are expected in almost any experimentally relevant observable, from heat capacity to transport properties. Standard scaling theory [28] predicts power-law dependences on disorder, chemical potential, or temperature in the vicinity of the critical point [19,22]. The only input to this variety of predicted power laws is a pair of critical exponents characteristic of the universality class. Denoting the dimensionless disorder strength and chemical potential by K and μ, respectively, close to the critical point $K = K_c$, $\mu = 0$ the correlation length exponent ν and the dynamical critical exponent z govern the relation between reduced disorder strength $k = |K - K_c|/K_c$ and the emerging correlation length ζ as $\zeta \propto k^{-\nu}$, and the relation between emergent energy and length scales as $\varepsilon \propto \zeta^{-z}$. Although the critical point is located at zero chemical potential, predictions of scaling theory persist for small finite doping.

To date, the best analytical estimates for ν and z for a single Weyl or Dirac node follow from a Wilsonian momentum shell RG calculation in an ϵ-expansion scheme around critical dimension two. The results of the one-loop calculation by Goswami and Chakravarty are $\nu = 1$ and $z = 1.5$ [14]. The accuracy of the one-loop exponents was challenged by a calculation of two-loop diagrams by Roy and Das Sarma [29], who found $\nu = 1.14$ and $z = 1.31$. On the other hand, there are instances where the ϵ expansion strategy is known to fail completely, the Anderson metal-insulator transition in three dimensions being a well-known example [30]—although the present transition is of a different type as it connects two noninsulating phases [23]. Numerical results for the critical exponents obtained from tight-binding models harboring multiple Weyl or Dirac nodes [22–26] are in reasonable agreement with the one-loop results above, albeit with large uncertainties in ν, z, and K_c.

Motivated by the lack of a firm theoretical prediction and in view of potential experiments, we performed a numerical calculation of the critical exponents in a single Weyl node using state-of-the-art finite-size scaling for quantum transport properties. Our results, which we report in detail below, have significantly reduced uncertainties in comparison to the previously known estimates. Whereas our result for the dynamical critical exponent, $z = 1.49 \pm 0.02$, is consistent with the previous numerical calculations and with the one-loop calculation (but not with the two-loop calculation), our value for the correlation length exponent, $\nu = 1.47 \pm 0.03$, deviates rather significantly.

Minimal model and numerical method. The minimal model for the disorder-induced quantum criticality is a single Weyl node with potential disorder,

$$H = \hbar v \boldsymbol{\sigma} \cdot \mathbf{k} + \mu + U(\mathbf{r}), \tag{1}$$

where v is the Fermi velocity, $\boldsymbol{\sigma}$ denotes the vector of Pauli matrices, and $\mathbf{k}$ measures the Bloch wave vector relative to

the nodal point. We connect the Weyl semimetal to two ideal leads, both modeled as Weyl nodes with μ taken to infinity and without the random potential U. The Weyl semimetal has dimension $0 < x < L$ and $0 < y,z < W$ in transport and transverse directions, respectively. To quantize transverse momenta $k_{y,z}$ we apply periodic or antiperiodic boundary conditions (PBCs or APBCs). An ultraviolet cutoff Λ restricts the magnitude of transverse wave vector $|k_{y,z}| \leqslant \Lambda$ and $1/\Lambda$ sets the microscopic length scale. The random potential $U(\mathbf{r})$ is assumed to have zero mean and Gaussian white-noise fluctuations

$$\langle U(\mathbf{r})U(\mathbf{r}')\rangle = \frac{K}{\Lambda}(\hbar v)^2\delta(\mathbf{r}-\mathbf{r}'), \tag{2}$$

with K the dimensionless disorder strength. The chemical potential μ has to vanish to reach the critical point, however, we will work with finite μ below to assess the dynamical critical exponent z.

We study the signatures of disorder-induced quantum criticality of Eq. (1) in a quantum transport framework at zero temperature, employing the numerical scattering matrix method of Ref. [21], which is based on related studies of disordered Dirac fermions in two dimensions [31,32]. The conductance can be computed from the scattering matrix's transmission block t using the Landauer formula $G = \mathrm{tr}\, tt^\dagger$ and is measured in units of e^2/h throughout.

Correlation length exponent ν: Finite-size scaling of the conductance for $\mu = 0$. The standard method to assess the correlation length exponent ν is finite-size scaling [28]. To perform such an analysis, one needs to identify a dimensionless observable that assumes different values on the two sides of the (bulk) phase transition. In Ref. [21] we showed numerically that the conductance G fulfills these requirements. For large aspect ratio $r \equiv W/L \gg 1$ and in the thermodynamic limit $L \to \infty$, the conductance takes the values $G_{K=0} = r^2(\ln 2/2\pi) \simeq 0.11r^2$ in the pseudoballistic phase at disorder strength $K = 0$ [33] and $G_{K\to\infty} = \sigma r^2 L \to \infty$ in the diffusive phase for $K > K_c$ (with bulk conductivity σ) [21]. In the vicinity of the critical point $K = K_c$, when the system dimensions L, W are larger than all internal length scales other than the emerging correlation length ζ, G assumes a scaling form $G = G(L/\zeta, W/\zeta)$. Using $\zeta \propto k^{-\nu}$ and fixing the aspect ratio $r = W/L$, we arrive at $G = G_r(L^{1/\nu}k)$, with universal correlation length exponent ν and a scaling function G_r that depends on r and the boundary conditions.

Numerically, the conductance G is found to vary considerably for different disorder realizations, however, with the restriction $G > G_{K=0}$ for every disorder realization. The histogram of $\delta G \equiv G - G_{K=0}$ is shown in Fig. 1 for the specific choice $L = 2\pi/(\Lambda r) \times 11$, PBC. For weak disorder, $K \lesssim 5$, we find that the distribution of δG can be well fitted by a log-normal distribution $p_{\mathrm{LN}}(\delta G) = e^{-(\ln \delta G - \mu_{\mathrm{LN}})^2/2\sigma_{\mathrm{LN}}^2}/\sigma_{LN}\delta G\sqrt{2\pi}$, with parameters μ_{LN} and σ_{LN}, see Fig. 1. A feature not captured by this fit is the tail of large but rare conductances, which are possibly related to rare region effects [34]. As G is not self-averaging (analogous to Anderson localization), we choose the median m of the distribution as a scaling quantity, i.e., we search a scaling function $m = m_r(L^{1/\nu}k)$. The standard error of the median is calculated using the asymptotic variance formula $\sigma_m^2 = 1/4p(m)^2N$, where N is the total number of disorder realizations and the unknown exact probability density p is approximated by a smooth interpolation of the measured histogram. For further research, it would be desirable to understand the occurrence of the empirical log-normal conductance distribution.

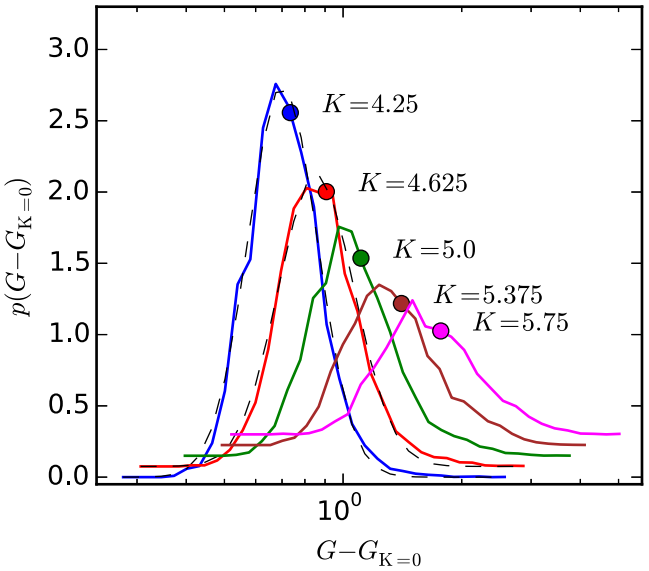

FIG. 1. (Color online) Probability distribution of the difference $\delta G = G - G_{K=0}$ of the conductance with and without disorder potential. The aspect ratio $r = W/L = 5$, periodic boundary conditions were applied in the transverse direction, and the sample length $L = (2\pi/\Lambda) \times 11/r$. The dimensionless disorder strength is indicated in the figure. The number of disorder realizations is 4000. Dots indicate the value of the median m, which is used as the scaling variable. Dashed lines show fits to a log-normal probability distribution. The data for $K > 4.25$ is offset in vertical direction for clarity.

We compute m for a range of disorder strengths K and lengths L, for aspect ratios $r = 5$ and 7, and we also varied the boundary condition between periodic and antiperiodic. The data for $r = 5$, PBC, is shown in Fig. 2, the other data sets can be found in the Supplemental Material [35]. At criticality, where ζ diverges, m_r is independent of L and the data traces in Fig. 2 cross in one point. In the Supplemental Material [35], we show the details of a least-squares fit for $m_r(L^{1/\nu}k)$ for small k to a polynomial of fourth order in $L^{1/\nu}k$ (solid lines). An excellent and stable fit was achieved even without including any irrelevant scaling variable that we took in leading order as L^y with $y < 0$. Taking into account the fitting results of all other parameter sets in a standard procedure (see Ref. [35] and Refs. [36–39]) we find $\nu = 1.47 \pm 0.03$. The conductance data for smaller aspect ratios $r \lesssim 3$ (data not shown) reveals a large irrelevant contribution to the scaling function that hindered a successful fit in terms of a simple low-order polynomial.

In Ref. [21] it was argued that the Fano factor F (the ratio of shot-noise power and conductance) is an alternative quantity to distinguish the pseudoballistic from the diffusive phase. In the pseudoballistic phase one has $F(K < K_c) \simeq 0.574$ while in the diffusive phase $F(K > K_c) = 1/3$. In the Supplemental Material we show that our result for ν is consistent with the value obtained from a finite-size scaling analysis using the

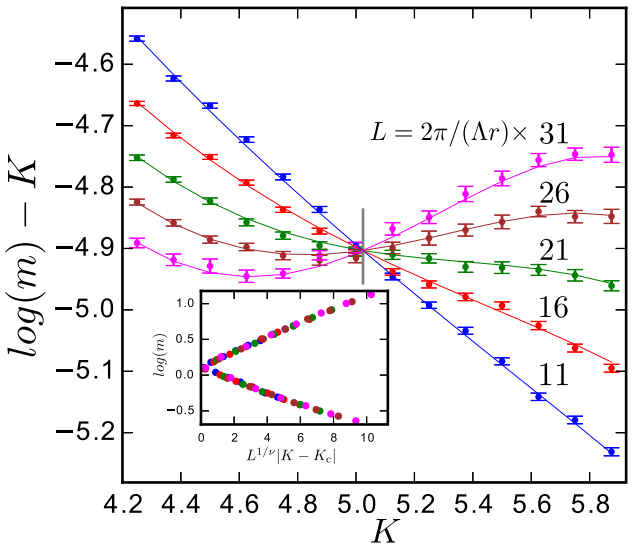

FIG. 2. (Color online) Scaling plot for the logarithm of the median m of the distribution of $\delta G = G - G_{K=0}$ for a disordered Weyl node with $W/L = 5$ and periodic transverse boundary conditions. For better visibility we plot $\log(m) - K$ vs. K on the vertical axis. The solid curves show the results of a least-squares fit to a scaling form $m = m_r(L^{1/\nu}k)$, expanded in a fourth-order polynomial (for details, see Ref. [35]). The estimates for the most important fit parameters and their standard error are $K_c = 5.024 \pm 0.004$, $\log(m_c) = 0.12 \pm 0.004$, $\nu = 1.47 \pm 0.02$. The quality of the fit is $\chi^2/N = 0.93$. The sample lengths are indicated in the figure. The gray vertical line indicates the position of the estimated critical disorder strength. The inset shows a scaling collapse of the data in the main panel using the estimated values of K_c and ν.

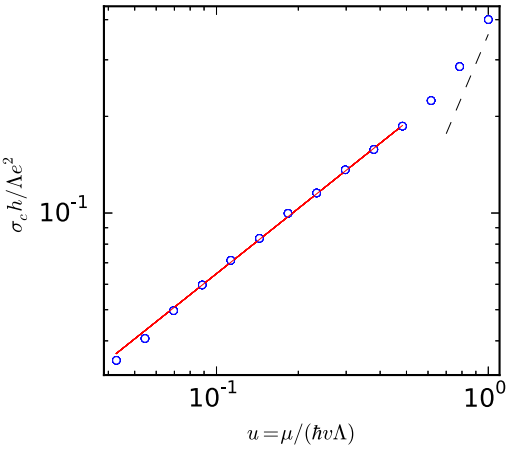

FIG. 3. (Color online) Scaling of the conductivity $\sigma(K,\mu)$ for (near) critical disorder strengths $K = 5.0$ (dots) with chemical potential μ. The solid line is a power-law fit $\sigma \propto \mu^{1/z}$ to the data points, with $z = 1.49 \pm 0.02$. The dashed line indicates a $\sigma \propto \mu^2$ power law as expected from Drude transport theory when scaling breaks down. The sample width $W = (2\pi/\Lambda) \times 29$ and periodic boundary conditions were applied. For chemical potentials below the values shown in the figure a bulk conductivity could not be reliably obtained from the calculated conductance data.

Fano factor ($\nu = 1.40 \pm 0.05$). This method however suffers from an inferior quality of the data set, both in terms of error bars of the individual data points as well as in the range of system sizes available.

Dynamical critical exponent: Scaling of critical bulk conductivity. We now turn to the dynamical critical exponent z that connects the emergent length scale ζ and the corresponding energy scale ε in the vicinity of the fixed point. In our transport geometry, a natural choice of a quantity that has a scaling involving the dynamical exponent z is the bulk conductivity σ, which is also of immediate experimental relevance.

To connect the dynamical critical exponent to the conductivity, we again start with a scaling form around criticality [19]. Since the unit of σ in three dimensions is inverse length, we find $\sigma(k,\mu) = \zeta^{-1} f(\mu/\varepsilon)$ with an unknown dimensionless scaling function f. We define a new scaling function $f(x) = x^{1/z}\tilde{f}(x^{-1})$ in terms of which $\sigma(k,\mu) = \mu^{1/z}\tilde{f}(k^{z\nu}/\mu)$. At $K = K_c$, the critical conductivity σ_c thus scales as

$$\sigma_c(\mu) \propto \mu^{1/z}. \tag{3}$$

The scaling form (3) is valid with small corrections within an extended quantum critical region [20] for finite k when the argument of $\tilde{f}$ is sufficiently small, i.e., $k \ll k^*(\mu) \propto \mu^{1/(\nu z)}$. This allows us to numerically compute an estimate of z in spite of the fact that the value of K_c is known only within error bars.

We compute $G(L)$ for fixed large W, PBC, a range of μ and for $K = 5.0$, which is within the K_c confidence interval [35]. We perform a disorder average over at least ten disorder realizations. Since transport in a Weyl node at finite μ is diffusive, we expect $G = \sigma W^2/L$, which is confirmed in the simulation. Finite-size effects are irrelevant once W,L are larger than the characteristic μ-induced length scale $\propto \mu^{-1/z}$. We show σ_c vs μ for $K = K_c$ in Fig. 3 (dots) and indeed observe a power law (solid line) for $\mu \lesssim \hbar v\Lambda$ with inverse exponent $z = 1.49 \pm 0.02$. For larger chemical potentials, μ comparable to the band edge $\hbar v\Lambda$, the scaling breaks down and from Drude transport theory we expect a crossover to $\sigma \propto \mu^2$, proportional to the density of states (dashed line).

Discussion. We numerically studied the disorder-induced quantum phase transition in three-dimensional Dirac materials in terms of a minimal model, a single Weyl node with potential disorder. In contrast to the well-known Anderson metal-insulator transition, this disorder-induced phase transition for a single Weyl node is between two noninsulating phases. In addition to the correlation-length exponent ν, it features a nontrivial dynamical critical exponent z, which has no counterpart in the standard metal-insulator transition.

Our high-precision results for the exponents ν and z not only allow for a variety of quantitative predictions of experimentally observable power laws around criticality—such as the density-of-states exponent $\beta = \nu(3 - z)$ for $K > K_c$ [22]—but also improve on previously reported theoretical predictions. Our result $\nu = 1.47 \pm 0.03$ differs significantly from analytical results obtained from a one- or two-loop ε-expansion RG calculation ($\nu = 1$, 1.14, respectively [14,29]). The failure of the ϵ-expansion calculation is reminiscent of the situation for the Anderson localization in three dimensions [30], where $\nu = 1.375$ in the symplectic class [40]. Our estimate for the dynamical critical exponent is $z = 1.49 \pm 0.02$, in agreement with the one-loop RG calculation ($z = 1.5$), but not with the two-loop prediction ($z = 1.31$).

In principle, the model of Eq. (1), which has white-noise disorder and a sharp momentum cutoff, could be modified to include a more faithful representation of the microscopic disorder, albeit at an increased numerical cost. For example, Ref. [21] employed a finite disorder correlation length that sets the microscopic length scale; the mode cutoff then can safely be taken to infinity. However, the difference between these two models is irrelevant in the RG sense and thus both models are in the same universality class. To see this, recall that a finite disorder correlation length is equivalent to a higher-order momentum dependence of the disorder-induced interaction vertex in the replicated disorder-averaged action and is thus irrelevant [41]. On the other hand, the numerical value of K_c is nonuniversal and, thus, sensitive to the disorder model. In this context we note that a model with sharp momentum cutoff has also been used in Ref. [31], where it was found to give the same results as a model with finite disorder correlation length. Moreover, in a realistic band structure the linear form of Eq. (1) is only an approximation. Quadratic corrections, however, are RG irrelevant and thus will not change the critical exponents [14].

Realistic Weyl and Dirac semimetals. Realistic Weyl or Dirac semimetals have multiple Weyl nodes [42], either separated in momentum space or distinguished by their transformation properties under point group symmetries. The same applies to numerical studies based on tight-binding models [22–26], which confirmed the presence of a disorder-induced phase transition on the basis of density-of-states calculations. With multiple Weyl nodes, disorder might not only cause intranode but also internode scattering of quasiparticles. The latter process is not captured by our minimal model. Symmetries in more realistic models with multiple Weyl nodes may also be different from the minimal model: While our minimal model has an effective time-reversal symmetry mapping the single Weyl node onto itself, in realistic models, time-reversal or inversion symmetries can relate different nodes or be absent. Although the precise nature of disorder potentials in realistic three-dimensional Dirac materials is yet to be determined, there are plausible scenarios in which intranode scattering dominates over internode scattering, *a priori* justifying the use of our minimal model. For example, in Weyl semimetals the ratio of scattering rates is controlled by the smoothness of the disorder potential and the separation of Weyl nodes in momentum space [43].

The applicability of the minimal model in the presence of sizable internode scattering, i.e., the question whether or not the presence of some amount of internode scattering changes the universality class of the disorder-induced semimetal-metal transition, is an issue that has not been conclusively settled [44]. Internode scattering is omitted in field-theoretical approaches [14,19]. Empirical evidence that internode scattering does not affect the universality of the transition comes from Ref. [24], which found a remarkable universality for three different disorder types in a tight-binding Dirac semimetal model, albeit with large error bars on the critical exponents.

If the assertion of a single universality class insensitive to intercone or intracone scattering (and the related symmetry differences) is correct, the observed critical exponents should match with those obtained in tight-binding models. However, such studies [22–26] yield a value for ν inconsistent with our result, for a typical example see Ref. [22], which finds $\nu = 0.92 \pm 0.13$ at $K > K_c$ and $\nu = 0.81 \pm 0.21$ at $K < K_c$. The value of the dynamical critical exponent $z = 1.5 \pm 0.1$ from Ref. [22] is in agreement with our result. Assuming that the type of scattering is indeed immaterial for critical exponents, we attribute the large difference with the tight-binding model exponent ν to difficulties in accurately estimating the critical disorder strength from density-of-states data. The uncertainty of K_c translates to a large uncertainty in the critical exponent ν. In contrast, our very precise estimate of K_c was possible using the finite-size scaling method where K_c can be obtained from the unique crossing of the data in Fig. 2.

In the Supplemental Material [35], we exemplify this interpretation by revisiting the density of states data from Ref. [22] [cf. Fig. 3(a)] obtained at zero energy for a range of disorder values around the critical disorder strength. Using the critical exponent $\beta = 2.22$ calculated with our estimates for ν and z we are able to produce an excellent fit for the data points in the vicinity of the critical disorder strength, though we find a much smaller critical disorder strength than asserted in Ref. [22]. Since the microscopic model in Ref. [22] and in this work are different, the values of the nonuniversal critical disorder strengths cannot be compared. Uncertainty in K_c does not cause comparable problems when determining the critical exponent z, because the large size of the critical region in the chemical potential–disorder parameter plane renders the extraction of z much less sensitive to the uncertainty in K_c. This is consistent with the mutual agreement between our estimate for z and the value in Ref. [22].

Acknowledgments. It is a pleasure to thank Johannes Reuther, Maximilian Trescher, and Tomi Ohtsuki for helpful discussions and Jörg Behrmann and Jens Dreger for support on the computations done on the HPC cluster of Fachbereich Physik at FU Berlin. We further acknowledge discussion with Sankar Das Sarma and correspondence with Pallab Goswami and Jed Pixley. Financial support was granted by the Helmholtz Virtual Institute "New states of matter and their excitations", by the Alexander von Humboldt Foundation in the framework of the Alexander von Humboldt Professorship, endowed by the Federal Ministry of Education and Research, and by the DFG's Emmy Noether program (BE 5233/1-1).

[1] T. O. Wehling, A. M. Black-Schaffer, and A. V. Balatsky, Adv. Phys. **63**, 1 (2014).

[2] J. Cayssol, C. Rend. Phys. **14**, 760 (2013); P. Hosur and X. Qi, *ibid.* **14** 857 (2013).

[3] A. Burkov, J. Phys.: Condens. Matter **27**, 113201 (2015).

[4] K. S. Novoselov, A. K. Geim, S. V. Morozov, D. Jiang, M. I. Katsnelson, I. V. Grigorieva, S. V. Dubonos, and A. A. Firsov, Nature (London) **438**, 197 (2005).

[5] Z. K. Liu, B. Zhou, Y. Zhang, Z. J. Wang, H. M. Weng, D. Prabhakaran, S.-K. Mo, Z. X. Shen, Z. Fang, X. Dai, Z. Hussain, and Y. L. Chen, Science **343**, 864 (2014).
[6] M. Neupane, S.-Y. Xu, R. Sankar, N. Alidoust, G. Bian, C. Liu, I. Belopolski, T.-R. Chang, H.-T. Jeng, H. Lin, A. Bansil, F. Chou, and M. Z. Hasan, Nat. Commun. **5**, 3786 (2014).
[7] S. Borisenko, Q. Gibson, D. Evtushinsky, V. Zabolotnyy, B. Büchner, and R. J. Cava, Phys. Rev. Lett. **113**, 027603 (2014).
[8] S. Jeon, B. B. Zhou, A. Gyenis, B. E. Feldman, I. Kimchi, A. C. Potter, Q. D. Gibson, R. J. Cava, A. Vishwanath, and A. Yazdani, Nature Mater. **13**, 851 (2014).
[9] L. P. He, X. C. Hong, J. K. Dong, J. Pan, Z. Zhang, J. Zhang, and S. Y. Li, Phys. Rev. Lett. **113**, 246402 (2014).
[10] B. Q. Lv, H. M. Weng, B. B. Fu, X. P. Wang, H. Miao, J. Ma, P. Richard, X. C. Huang, L. X. Zhao, G. F. Chen, Z. Fang, X. Dai, T. Qian, and H. Ding, Nat. Phys. **11**, 724 (2015).
[11] S.-Y. Xu, I. Belopolski, N. Alidoust, M. Neupane, C. Zhang, R. Sankar, S.-M. Huang, C.-C. Lee, G. Chang, B. Wang, G. Bian, H. Zheng, D. S. Sanchez, F. Chou, H. Lin, S. Jia, and M. Z. Hasan, Science **349**, 613 (2015).
[12] S.-Y. Xu, N. Alidoust, I. Belopolski, Z. Yuan, G. Bian, T.-R. Chang, H. Zheng, V. Strocov, D. S. Sanchez, G. Chang, C. Zhang, D. Mou, Y. Wu, L. Huang, C.-C. Lee, S.-M. Huang, B. Wang, A. Bansil, H.-T. Jeng, T. Neupert, A. Kaminski, H. Lin, S. Jia, M. Z. Hasan, Nat. Phys. **11**, 748 (2015).
[13] L. Lu, Z. Wang, D. Ye, L. Ran, L. Fu, J.-D. Joannopoulos, and M. Soljačić, Science **349**, 622 (2015).
[14] P. Goswami and S. Chakravarty, Phys. Rev. Lett. **107**, 196803 (2011).
[15] P. Hosur, S. A. Parameswaran, and A. Vishwanath, Phys. Rev. Lett. **108**, 046602 (2012).
[16] E. Fradkin, Phys. Rev. B **33**, 3263 (1986).
[17] E. Fradkin, Phys. Rev. B **33**, 3257 (1986).
[18] Y. Ominato and M. Koshino, Phys. Rev. B **89**, 054202 (2014).
[19] S. V. Syzranov, L. Radzihovsky, and V. Gurarie, Phys. Rev. Lett. **114**, 166601 (2015).
[20] S. V. Syzranov, V. Gurarie, and L. Radzihovsky, Phys. Rev. B **91**, 035133 (2015).
[21] B. Sbierski, G. Pohl, E. J. Bergholtz, and P. W. Brouwer, Phys. Rev. Lett. **113**, 026602 (2014).
[22] K. Kobayashi, T. Ohtsuki, K.-I. Imura, and I. F. Herbut, Phys. Rev. Lett. **112**, 016402 (2014).
[23] J. H. Pixley, P. Goswami, and S. Das Sarma, Phys. Rev. Lett. **115**, 076601 (2015).
[24] J. H. Pixley, P. Goswami, S. Das Sarma, arXiv:1505.07938v2.
[25] S. Bera, J. D. Sau, and B. Roy, arXiv:1507.07551v1.
[26] S. Liu, T. Ohtsuki, and R. Shindou, arXiv:1507.02381v1.
[27] A. Altland and D. Bagrets, Phys. Rev. Lett. **114**, 257201 (2015).
[28] J. Cardy, *Scaling and Renormalization in Statistical Physics* (Cambridge University Press, Cambridge, 1996).
[29] B. Roy and S. Das Sarma, Phys. Rev. B **90**, 241112(R) (2014).
[30] B. Kramer and A. McKinnon, Rep. Prog. Phys. **56**, 1469 (1993).
[31] J. H. Bardarson, J. Tworzydło, P. W. Brouwer, and C. W. J. Beenakker, Phys. Rev. Lett. **99**, 106801 (2007).
[32] S. Adam, P. W. Brouwer, and S. Das Sarma, Phys. Rev. B **79**, 201404 (2009).
[33] P. Baireuther, J. M. Edge, I. C. Fulga, C. W. J. Beenakker, and J. Tworzydlo, Phys. Rev. B **89**, 035410 (2014).
[34] R. Nandkishore, D. A. Huse, and S. L. Sondhi, Phys. Rev. B **89**, 245110 (2014).
[35] See Supplemental Material at http://link.aps.org/supplemental/10.1103/PhysRevB.92.115145 for details of the finite-size scaling analysis, scaling of the Fano factor and comparison to density-of-states scaling for tight-binding model.
[36] K. Slevin and T. Ohtsuki, Phys. Rev. Lett. **82**, 382 (1999).
[37] H. Obuse, I. A. Gruzberg, and F. Evers, Phys. Rev. Lett. **109**, 206804 (2012).
[38] H. Obuse, S. Ryu, A. Furusaki, and C. Mudry, Phys. Rev. B **89**, 155315 (2014).
[39] H. Obuse, S. Bera, A. W. W. Ludwig, I. A. Gruzberg, and F. Evers, Europhys. Lett. **104**, 27014 (2013).
[40] Y. Asada, K. Slevin, and T. Ohtsuki, J. Phys. Soc. Jpn. **74**, 238 (2005).
[41] R. Shankar, Rev. Mod. Phys. **66**, 129 (1994).
[42] H. Nielsen and M. Ninomiya, Nucl. Phys. B **185**, 20 (1981).
[43] For disordered Dirac semimetals where Weyl nodes coincide, spatial symmetries of the specific model can suppress internode scattering.
[44] Internode scattering, if strong enough, leads to a standard Anderson localization transition for strong disorder [23], which can be regarded as a competing physical scenario.

Supplemental information

Details of the finite-size scaling analysis. We here provide details of the finite-size scaling procedure, following Refs. [1–3]. In addition to the data set presented in the main text — aspect ratio $r = 5$ and periodic boundary conditions (PBC) —, we have obtained conductance distributions for antiperiodic boundary conditions (APBC) with $r = 5$ and for aspect ratio $r = 7$, PBC.

The sample width $W = L \cdot r$ is set to be $W = (2\pi/\Lambda)(M - 1/2)$ for APBC and $W = (2\pi/\Lambda)M$ for PBC, with M a positive integer. The transverse wavenumbers are $k_{y,z} = (2\pi/W)n_{y,z}$, with $n_{y,z} = -M, -M + 1, \ldots, M$ for PBC and $n_{y,z} = -M + 1/2, -M + 3/2, \ldots, M - 1/2$ for APBC. A summary of all data sets used in this work is given in Table I.

For each data set, the median $m(K, M)$ of the conductance distribution is determined. We perform a least-squares fit to a polynomial of the form

$$\begin{aligned} m(K,M) \;=\; & a_0(1 + b_{01}L^y + \ldots + b_{0q_0}L^{yq_0}) + a_1 \cdot (L^{1/\nu}k) \cdot (1 + b_{11}L^y + \ldots + b_{1q_1}L^{yq_1}) \\ & + \ldots + a_p \cdot (L^{1/\nu}k)^p \cdot (1 + b_{11}L^y + ...b_{1q_p}L^{yq_p}) \end{aligned} \tag{1}$$

for medians obtained at the same value of the aspect ratio r and the same boundary conditions. Data points (*i.e.*, medians of conductance distributions) and fits are shown in Fig. 2 of the main text for $r = 5$ and PBC, and in Fig. 1 for $r = 5$, APBC, and and $r = 7$, PBC. The following algorithm for the fitting procedure is used: The order of the polynomials in Eq. (1) is increased by adding a new fit parameter a_i or b_{ij} if (i) the merit function $\chi^2/N \in [0, \infty]$ (N is the number of data points) for the resulting fit is lowered by more than 2% compared to the previous fit and (ii) the error of any fitting parameter (as calculated from error propagation theory) does not exceed the parameter's estimate in magnitude. Initial values for each fitting procedure are chosen randomly and the parameter estimates for the best fit out of a few hundred fitting trials is reported in Table I along with the error estimates and the value of χ^2/N. A fit is acceptable if $\chi^2/N < 1$, another measure is the 'goodness of the fit' $\mathcal{G} \in [0, 1]$ where $\mathcal{G} = 1$ indicates a perfect fit (for definitions of $\mathcal{G}$ and χ^2/N see, for example, Ref. [3]).

Ideally, fitting parameters should not strongly depend on the number of different values of M within a data set. We successfully checked the stability of the fitting results by repeating the fitting procedure above for reduced data sets (deleting data points of the largest or smallest M in the data set $r = 5$, PBC), as indicated in Table I. Finally, the estimate for ν is calculated as an average of the best fit estimates for ν for each data set whereas the total error bars are unions of error bars from each single data set ('practical-error-bar procedure', see Ref. [4]).

$r = W/L$	B.C.	M	N	χ^2/N	$\mathcal{G}$	ν	K_c	$log(m_c) = a_0$	$a_1 \cdot 10^1$	$a_2 \cdot 10^2$	$-a_3 \cdot 10^2$	$-a_4 \cdot 10^3$
5	PBC	11, 16, 21, 26, 31	70	0.93	0.4	1.47 ± 0.02	5.024 ± 0.004	0.12 ± 0.004	5.0 ± 0.1	3.0 ± 0.3	1.3 ± 0.1	1.8 ± 0.9
5	PBC	16, 21, 26, 31	56	0.62	0.94	1.46 ± 0.02	5.007 ± 0.007	0.102 ± 0.006	4.9 ± 0.2	3.3 ± 0.4	1.2 ± 0.1	2.6 ± 1.2
5	PBC	11, 16, 21, 26	56	0.84	0.55	1.48 ± 0.02	5.036 ± 0.006	0.128 ± 0.004	5.0 ± 0.1	3.2 ± 0.4	1.4 ± 0.1	2.3 ± 1.3
5	APBC	14, 19, 24, 29	56	0.97	0.29	1.47 ± 0.02	5.031 ± 0.005	0.169 ± 0.004	4.9 ± 0.1	2.8 ± 0.3	1.1 ± 0.1	1.7 ± 0.8
7	PBC	19, 26, 33	42	0.64	0.87	1.47 ± 0.03	4.983 ± 0.009	0.782 ± 0.007	4.8 ± 0.2	2.1 ± 0.2	1.5 ± 0.2	-

Table I: Details of the finite-size scaling procedure. The left part of the table specifies the data sets subject to a least squares fit with model (1) while the right part gives the fitting results. Numbers with ± are error bars (one standard deviation). The range of disorder strength for all data sets is $K = 4.25, 4.375, \ldots, 5.875$.

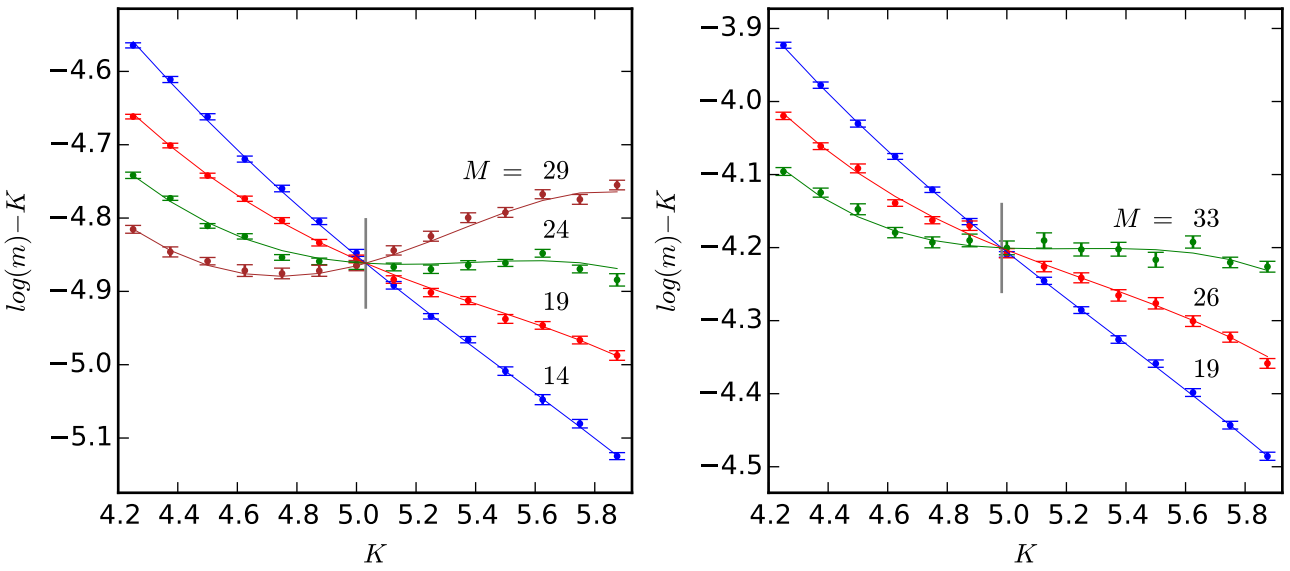

Figure 1: (color online) Scaling plots for the logarithm of the median m of the distribution of the difference $\delta G = G - G_{K=0}$ of the two-terminal conductance with and without disorder potential, for a Weyl cone with aspect ratio $r = W/L = 5$ and antiperiodic boundarity conditions (left) and $r = 7$ and periodic boundary conditions (right). For clarity, we plot $log(m) - K$ vs. K. The solid curves show the results of a least-squares fit to a scaling form $m = m_r\left(L^{1/\nu}k\right)$ expanded in a fourth ($r = 5$) and third ($r = 7$) order polynomial, respectively. The estimates for the most important fit parameters are given in Table I. The gray vertical line indicates the position of the estimated critical disorder strength.

Comparison with finite-size scaling for Fano factor. As discussed in the main text, besides the conductance, also the Fano factor can be expected to be a suitable observable for a finite-size scaling analysis. A scaling plot is shown in Fig. 2 and the details of the analysis (done as above for the conductance data) are reported in Table II. Although the number of disorder realizations is comparable to the corresponding conductance data in Fig. 1 (left), for the Fano factor error bars are much larger. Moreover, while for conductance scaling data traces for system sizes $M = 14, 19, 24, 29$ all cross in a single point, the Fano factor data for $M = 14$ does not cross with the traces of the larger system sizes, indicating that shot noise around criticality is controlled by larger emergent length scales than conductance. For the remaining system sizes, the analysis yields $\nu = 1.40 \pm 0.05$. Given the intrinsic difficulties for the Fano factor data discussed above we consider the error bar overlap with the conductance result $\nu = 1.47 \pm 0.03$ as a confirmation for consistency of the two finite-size scaling methods.

$W/L = r$	B.C.	M	N	χ^2/N	$\mathcal{G}$	ν	K_c	$log(m_c) = a_0$	$a_1 \cdot 10^1$	$a_2 \cdot 10^2$	$a_3 \cdot 10^3$	$a_4 \cdot 10^3$
5	APBC	19, 24, 29	42	0.72	0.69	1.40 ± 0.05	4.994 ± 0.015	-3.4 ± 0.01	4.3 ± 0.5	5.9 ± 1.5	-6 ± 2	-5 ± 3

Table II: Details of the finite-size scaling procedure for the Fano factor. The left part of the table specifies the data sets subject to a least squares fit with model (1) while the right part gives the fitting results. Numbers with ± are error bars (one standard deviation). The range of disorder strength is $K = 4.25, 4.375, \ldots, 5.875$.

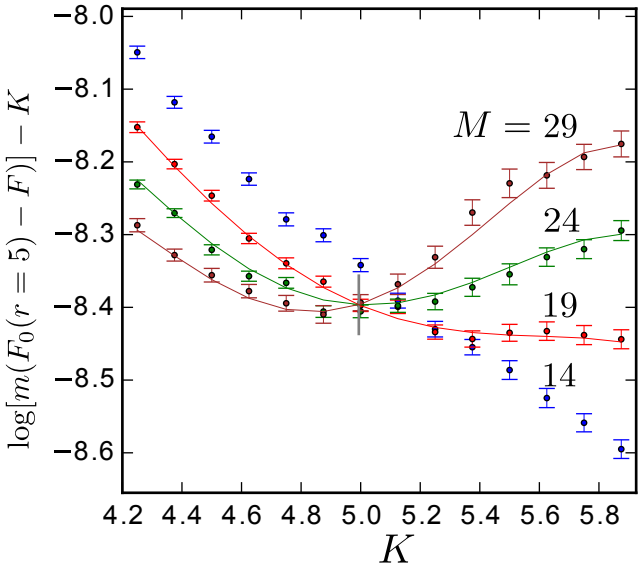

Figure 2: (color online) Scaling plots for the logarithm of the median m of the distribution of the difference $\delta F = F_{K=0} - F$ of the two-terminal Fano factor without and with disorder potential, for a Weyl cone with aspect ratio $r = W/L = 5$ and antiperiodic boundarity conditions. For clarity, we plot $log(m) - K$ vs. K. The solid curves show the results of a least-squares fit to a scaling form $m = m_r \left(L^{1/\nu} k\right)$ expanded in a fourth order polynomial. The data set for $M = 14$ was not included in the analysis. The estimates for the most important fit parameters are given in Table II. The gray vertical line indicates the position of the estimated critical disorder strength.

Comparison with density-of-states scaling for tight-binding model. We revisit the results of a recent density-of-states simulation in a disordered Dirac semimetal from Ref. [5]. The study is based on a large four-band tight-binding model tuned at the topological phase transition between a strong and weak topological insulator. If inter-node processes can be neglected, around criticality the density of states at zero energy should increase as $\rho(\epsilon = 0) \propto (K - K_c)^\beta$ with $\beta = (3 - z)\nu$. Using our estimate $\beta = 2.2$, we successfully fit the data from from Ref. [5], (cf. Fig. 3a) in Fig. 3 (solid line), except for the three data points with largest disorder strength. In contrast, the emphasis in the interpretation of Ref. [5] was laid on data points for larger K, excluding the immediate vicinity of the critical point at $K = K_c$. This leads to a larger estimate for K_c and a smaller estimate for β.

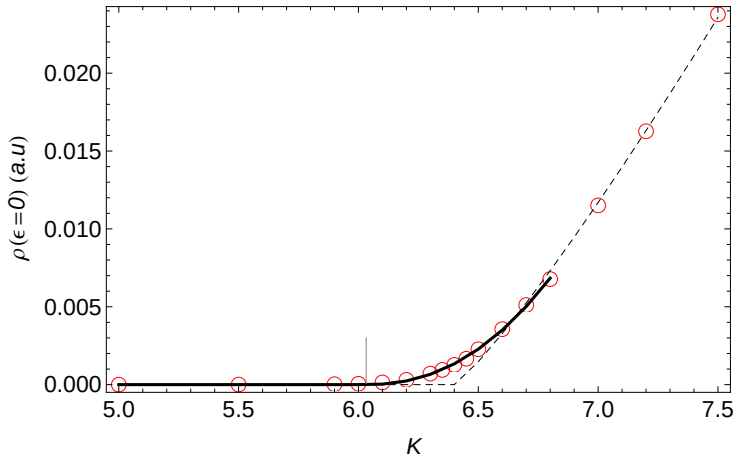

Figure 3: (color online) Bulk density of states of a disordered tight-binding model of a Dirac semimetal at zero energy as a function of disorder strength around criticality. The data (dots) is adapted from Ref. [5], Fig. 3a. The solid line is a fit to the scaling form $\rho(\epsilon = 0) \propto (K - K_c)^\beta$ with $\beta = (3 - z)\nu$ fixed to 2.22 from our finite-size scaling analysis taking into account data points with $K < 7$ only. The vertical gray line shows the corresponding estimate $K_c = 6.03$. The dashed line is a fit of the eight data points with the largest K with setting $K_c = 6.4$ [5], the estimate for the exponent is $\beta = 1.16$.

[1] K. Slevin and T. Ohtsuki, Phys. Rev. Lett. **82**, 382 (1999).
[2] H. Obuse, I. A. Gruzberg, and F. Evers, Phys. Rev. Lett. **109**, 206804 (2012)
[3] H. Obuse, S. Ryu, A. Furusaki, and C. Mudry, Phys. Rev. B **89**, 155315 (2014).
[4] H. Obuse, S. Bera, A. W. W. Ludwig, I. A. Gruzberg, and F. Evers, Europhys. Lett. **104**, 27014 (2013).
[5] K. Kobayashi, T. Ohtsuki, K.-I. Imura, and I. F. Herbut, Phys. Rev. Lett. **112**, 016402 (2014).

4 Conclusion

Topological semimetals and topological insulators are closely related, indeed, as Altland and Bagrets put it [57]:

> "Where the latter support a gapped spectrum, and gap closure means a topological phase transition, the former have a gapless spectrum, and gap opening requires a phase transition."

In special cases, these two bandstructure classes are even more intricately intertwined: In the absence of inversion symmetry, a topological semimetal may appear as an intermediate phase between topological trivial and nontrivial insulating phases when a tuning parameter is varied [58].

In this thesis, we have theoretically studied topological insulator and semimetal phases and in particular their various phase transitions in the presence of elastic disorder scattering. As a powerful, versatile and well developed framework, we employed scattering theory as our main method of numerical investigation. We have demonstrated the topological content of the scattering matrix in the case for topological insulators and its ability to efficiently capture the coupling of two-dimensional topological surface states to one-dimensional dislocation line zero modes propagating in the bulk material. For Weyl topological semimetals, we indirectly inferred information about various phases and their critical points from the quantum transport properties like conductance and shot noise computed from the scattering matrix.

Wherever possible, we have corroborated our results by analytical calculations like the self-consistent Born approximation to the self energy. Often, only the unified picture stemming from both numerical and analytical approaches enabled us to fully grasp the underlying physics.

An overarching theme in all chapters of this thesis is the concept of disorder induced quantum phase transitions. In the topological insulator model, the phase transitions, which separate various topological and non-topological insulating phases are also known from the clean model, where they can be triggered by a tuning parameter in the Hamiltonian. In realistic topological insulators, alloy composition has been shown to serve as such a tuning knob experimentally. For the disordered sample, we studied the topological invariant by tracking the evolution of the eigenvalue phases of the reflection matrix under Aharonov-Bohm flux insertion. In this way,

we could show that variations in disorder strength alone enable similar topological phase transitions, an effect captured by band structure renormalization in the framework of the self-consistent Born approximation. In this setting the superior properties of our scattering matrix method, in particular its applicability for large systems, were instrumental to establish a high resolution phase diagram of the topological invariant without resorting to indirect measures of topology like the presence of edge states or the Witten effect. Even the subtle odd-even effect in the dependence of weak topological invariants on system size could be observed and previous poorly founded claims in literature about putative phase pockets could safely be rejected.

In the topological Weyl semimetal model, the effects of disorder are even more interesting in the sense that, first, the phase transition is genuinely disorder driven and thus has no counterpart in the clean system and, second, all previously employed analytical methods have limited applicability around the phase transition point. Our main results, based on the exact scattering matrix approach include

- The characterization of the semimetal to diffusive metal phase transition in terms of quantum transport properties which are of immediate interest for putative experiments involving mesoscopic samples.
- The prediction of a finite scale-invariant cube conductance in the weakly disordered pseudoballistic *phase*, as required by the inherent topology of a Weyl node and usually only found at the critical *point* of an Anderson metal-insulator transition.
- The identification of the Fano factor as a well suited signature for experimental observation of the pseudoballistic phase in a measurement based on just a single sample.
- For the pseudoballistic phase, the demonstration of a non-commutativity of the limits of zero chemical potential and infinite system size in this phase.
- The numerical determination of correlation length and dynamical critical exponents at the critical point with unprecedented precision enabled by a novel finite size scaling scheme.

While our research on topological insulators mainly demonstrated the performance and versatility of scattering matrix methods, we are optimistic that our results on disordered semimetals can be confirmed in future experiments as material science and the degree of control in sample fabrication makes tremendous progress. A particular promising research avenue, especially for experiments, is the field of magnetotransport in novel semimetals. Various quantum phenomena, some of topological origin, have been reported in such experiments [59, 60, 61, 62]. Part of the excitement stems from the fact that Weyl semimetals provide a solid state realization of the chiral anomaly known from field theory. We expect that a careful

study of disorder effects on transport physics in the presence of a magnetic field (and correspondingly another - magnetic - length scale) could be a fruitful, highly appreciated and rewarding research endeavor. Likewise, quantum transport properties of the Weyl metal surface states, although featured prominently in a recent magnetotransport experiment [60] has not enjoyed corresponding attention from the theory side.

In the case of dislocation line zero modes in a strong topological insulator slab, first steps towards the characterization of the emergent electronic phases have been demonstrated. The resulting electronic structure is controlled by the phase shifts associated to wave-packet propagation along the dislocation line. Characteristic properties easily accessible within the scattering matrix approach are the density of states at zero energy or the longitudinal conductivity. As an intriguing problem for further research beyond our work based on the scattering approach, we suggest the formulation of a corresponding theory in terms of a Hamiltonian and the experimental confirmation of our predictions.

Acknowledgments

I want to express my deep gratitude to my thesis advisor and referee Piet Brouwer. I am thankful for uncountable many discussion about ongoing research, bringing my thoughts back on track but also his trust, patience and acceptance while I was wandering off in foreign research areas. Thank you for your guidance, overspilling enthusiasm, advise and also the freedom I enjoyed during my PhD.

I appreciated the friendly and inspiring atmosphere at the Dahlem Center for Complex Quantum Systems. The numerous seminars, journal clubs and lectures constitute an excellent research environment, in particular I appreciated plentiful discussions with my coauthors and close collaborators Maximilian Trescher, Emil Bergholtz, Gregor Pohl and Martin Schneider. I further benefited from additional scientific discussions with Johannes Reuther, Andreas Dechant, Michele Filippone, Maresa Rieder, Tobias Micklitz, Christian Fräßdorf and Georg Schwiete. I enjoyed co-supervising the master and bachelor projects of Nils Buchholz, Gunnar Riemenschneider and Farhad Arbabzadeh. Beyond physics, I thank my numerous fellow group members for countless hours at the beach-volleyball court, the "Bertablock" climbing gym and at our favorite restaurants and bars in Berlin that are well remembered. Thank you!

Further, I want to thank Gabriele Herrmann for handling all administrative details, a prerequisite for the peace of mind required to do physics, and, last but not least, her wonderful birthday cards.

I want to thank Matthias Vojta for serving as a co-referee for my thesis.

This thesis would not have been possible without the tireless help I received from experts in computing from the first few lines of code onwards. I am indebted to Jörg Behrmann, Samuel Sanchez and particularly Jens Dreger and his 24/7 cluster support.

I acknowledge the funding received from the Helmholtz virtual institute "New states of matter and their excitations" that also covered several workshops, conferences, schools and a research stay at California Institute of Technology with Gil Refael.

Finally, I want to express my deepest gratitude to Julia who helped to keep my spirits up and my family for all their loving support and encouragement in the past years.

Bibliography

[1] B. Sbierski and P. W. Brouwer. Z2 phase diagram of three-dimensional disordered topological insulators via a scattering matrix approach. *Phys. Rev. B*, 89:155311, 2014.

[2] Björn Sbierski, Martin Schneider, and Piet W. Brouwer. The weak side of strong topological insulators. *Phys. Rev. B*, 93:161105, 2016.

[3] B. Sbierski, G. Pohl, E. J. Bergholtz, and P. W. Brouwer. Quantum Transport of Disordered Weyl Semimetals at the Nodal Point. *Phys. Rev. Lett.*, 113:026602, 2014.

[4] B. Sbierski, E. J. Bergholtz, and P. W. Brouwer. Quantum critical exponents for a disordered three-dimensionalWeyl node. *Phys. Rev. B*, 92:115145, 2015.

[5] M. Trescher, B. Sbierski, P. W. Brouwer, and E. J. Bergholtz. Quantum transport in Dirac materials: Signatures of tilted and anisotropic Dirac and Weyl cones. *Phys. Rev. B*, 91:115135, 2015.

[6] K. V. Klitzing, G. Dorda, and M. Pepper. New method for high accuracy determination of the fine structure constant based on quantized hall resistance. *Phys. Rev. Lett.*, 45:494, 1980.

[7] D. J. Thouless, M. Kohmoto, M. P. Nightingale, and M. Den Nijs. Quantized hall conductance in a two-Dimensional periodic potential. *Phys. Rev. Lett.*, 49:405, 1982.

[8] B. Halperin. Quantized Hall conductance, current-carrying edge states, and the existence of extended states in a two-dimensional disordered potential. *Phys. Rev. B*, 25:2185, 1982.

[9] D. C. Tsui, H. L. Stormer, and a. C. Gossard. Two-dimensional magnetotransport in the extreme quantum limit. *Phys. Rev. Lett.*, 48:1559, 1982.

[10] F. Haldane. Model for a quantum Hall effect without Landau levels: Condensed-matter realization of the "parity anomaly". *Phys. Rev. Lett.*, 61:2015, 1988.

[11] C. L. Kane and E. J. Mele. Quantum Spin Hall Effect in Graphene. *Phys. Rev. Lett.*, 95:226801, 2005.

[12] C. L. Kane and E. J. Mele. Z2 Topological Order and the Quantum Spin Hall Effect. *Phys. Rev. Lett.*, 95:146802, 2005.

[13] L. Fu and C. Kane. Time reversal polarization and a Z2 adiabatic spin pump. *Phys. Rev. B*, 74:195312, 2006.

[14] B. A. Bernevig, T. Hughes, and S.-C. Zhang. Quantum spin Hall effect and topological phase transition in HgTe quantum wells. *Science*, 314:1757, 2006.

[15] Markus König, Steffen Wiedmann, Christoph Brüne, Andreas Roth, Hartmut Buhmann, Laurens W Molenkamp, Xiao-liang Qi, and Shou-cheng Zhang. Quantum Spin Hall Insulator State in HgTe Quantum Wells. *Science*, 318:766, 2007.

[16] K. Nowack, E. Spanton, M. Baenninger, M. König, J. Kirtley, B. Kalisky, C. Ames, P. Leubner, C. Brüne, H. Buhmann, L. Molenkamp, D. Goldhaber-Gordon, and K. Moler. Imaging currents in HgTe quantum wells in the quantum spin Hall regime. *Nature materials*, 12:787, 2013.

[17] S. Hart, H. Ren, T. Wagner, P. Leubner, M. Mühlbauer, C. Brüne, H. Buhmann, L. Molenkamp, and A. Yacoby. Induced superconductivity in the quantum spin Hall edge. *Nat. Phys.*, 10:1, 2014.

[18] L. Fu, C. Kane, and E. Mele. Topological Insulators in Three Dimensions. *Phys. Rev. Lett.*, 98:106803, 2007.

[19] J. Moore and L. Balents. Topological invariants of time-reversal-invariant band structures. *Phys. Rev. B*, 75:121306, 2007.

[20] L. Fu and C. Kane. Topological insulators with inversion symmetry. *Phys. Rev. B*, 76:045302, 2007.

[21] Y. Ando. Topological insulator materials. *JPSJ*, 82:102001, 2013.

[22] S. Borisenko, Q. Gibson, D. Evtushinsky, V. Zabolotnyy, B. Büchner, and R. Cava. Experimental Realization of a Three-Dimensional Dirac Semimetal. *Phys. Rev. Lett.*, 113:027603, 2014.

[23] H. Nielsen and M. Ninomiya. Absence of neutrinos on a lattice. *Nuclear Physics B*, 185:20, 1981.

[24] A. Turner and A. Vishwanath. Beyond Band Insulators: Topology of Semimetals and Interacting Phases. *arXiv*, 1301.0330, 2013.

[25] X. Wan, A. Turner, A. Vishwanath, and S. Savrasov. Topological semimetal and Fermi-arc surface states in the electronic structure of pyrochlore iridates. *Phys. Rev. B*, 83:205101, 2011.

[26] B. A. Bernevig. It's been a Weyl coming. *Nat. Phys.*, 11:698, 2015.

[27] S.-Y. Xu, I. Belopolski, N. Alidoust, M. Neupane, G. Bian, C. Zhang, R. Sankar, G. Chang, Z. Yuan, C. Lee, S. Huang, H. Zheng, D. Sanchez, B. Wang, A. Bansil, F. Chou, P. Shibayev, H. Lin, S. Jia, and M. Z. Hasan. Discovery of a Weyl fermion semimetal and topological Fermi arcs. *Science*, 349:613, 2015.

[28] B. Q. Lv, N. Xu, H. M. Weng, J. Z. Ma, P. Richard, X. C. Huang, L. X. Zhao, G. F. Chen, C. Matt, F. Bisti, V. Strokov, J. Mesot, Z. Fang, X. Dai, T. Qian, M. Shi, and H. Ding. Observation of Weyl nodes in TaAs. *Nat. Phys.*, 11:724, 2015.

[29] S.-Y. Xu, I. Belopolski, D. Sanchez, C. Guo, G. Chang, C. Zhang, G. Bian, Z. Yuan, H. Lu, Y. Feng, T. Chang, P. Shibayev, M. Prokopovych, N. Alidoust, H. Zheng, C. Lee, S. Huang, R. Sankar, F. Chou, C. Hsu, H. Jeng, A. Bansil, T. Neupert, V. Strocov, H. Lin, S. Jia, and M. Z. Hasan. Experimental discovery of a topological Weyl semimetal state in TaP. *Sci. Adv.*, 1:e1501092, 2015.

[30] S. Borisenko, D. Evtushinsky, Q. Gibson, A. Yaresko, T. Kim, M. N. Ali, B. Buechner, M. Hoesch, and R. J. Cava. Time-reversal symmetry breaking Weyl state in YbMnBi2. *arXiv*, 1507.04847, 2015.

[31] J. Y. Liu, J. Hu, D. Graf, S. M. a. Radmanesh, D. J. Adams, Y. L. Zhu, G. F. Chen, X. Liu, J. Wei, I. Chiorescu, L. Spinu, and Z. Q. Mao. Discovery of a topological semimetal phase coexisting with ferromagnetic behavior in Sr1-yMnSb2. *arXiv*, 1507.07978, 2015.

[32] L. Lu, Z. Wang, D. Ye, L. Ran, L. Fu, J. D. Joannopoulos, and M. Soljacic. Experimental observation of Weyl points. *Science*, 349:622, 2015.

[33] M. Neupane, S. Xu, R. Sankar, N. Alidoust, G. Bian, C. Liu, I. Belopolski, T. Chang, H. Jeng, H. Lin, A. Bansil, F. Chou, and M. Z. Hasan. Observation of a three-dimensional topological Dirac semimetal phase in high-mobility Cd3As2. *Nat. Comm.*, 5:3786, jan 2014.

[34] Z. Liu, B. Zhou, Y. Zhang, Z. Wang, H. Weng, D. Prabhakaran, S.-K. Mo, Z. Shen, Z. Fang, X. Dai, Z. Hussain, and Y. Chen. Discovery of a three-dimensional topological Dirac semimetal, Na3Bi. *Science*, 343:864, 2014.

[35] S. Datta. *Electronic Transport in Mesoscopic Systems*. Cambridge University Press, 1997.

[36] H. Bruus and K. Flensberg. *Many-Body Quantum Theory in Condensed Matter Physics*. Oxford Graduate Texts, 2004.

[37] Y.M. Nazarov Y.V., Blanter. *Theory of Quantum Transport*. Cambridge University Press, 2009.

[38] C. Groth, M. Wimmer, A. Akhmerov, and X. Waintal. Kwant: a software package for quantum transport. *New J. Phys.*, 16:063065, 2014.

[39] P. Baireuther, J. M. Edge, I. C. Fulga, C. W. J. Beenakker, and J. Tworzydlo. Quantum phase transitions of a disordered antiferromagnetic topological insulator. *Phys. Rev. B*, 89:035410, 2014.

[40] J. Tworzydlo, B. Trauzettel, M. Titov, A. Rycerz, and C. Beenakker. Sub-Poissonian Shot Noise in Graphene. *Phys. Rev. Lett.*, 96:246802, 2006.

[41] E. Akkermans and G. Montambaux. *Mesoscopic Physics of Electrons and Photons*. Cambridge University Press, 2007.

[42] J. Rammer. *Quantum Transport Theory*. Perseus Books, 1998.

[43] C. Groth, M. Wimmer, A. Akhmerov, J. Tworzydlo, and C. Beenakker. Theory of the Topological Anderson Insulator. *Phys. Rev. Lett.*, 103:196805, 2009.

[44] D. Meidan, T. Micklitz, and P. W. Brouwer. Optimal topological spin pump. *Phys. Rev. B*, 82:161303, 2010.

[45] D. Meidan, T. Micklitz, and P. W. Brouwer. Topological classification of adiabatic processes. *Phys. Rev. B*, 84:195410, 2011.

[46] I. Fulga, F. Hassler, and A. Akhmerov. Scattering theory of topological insulators and superconductors. *Phys. Rev. B*, 85:165409, 2012.

[47] D. Xiao, M. Chang, and Q. Niu. Berry phase effects on electronic properties. *Rev. Mod. Phys.*, 82:1959, 2010.

[48] Y. Ran, Y. Zhang, and A. Vishwanath. One-dimensional topologically protected modes in topological insulators with lattice dislocations. *Nat. Phys.*, 5:298, 2009.

[49] R. Jackiw and P. Rossi. Zero modes of the vortex-fermion system. *Nuclear Physics B*, 190:681, 1981.

[50] E. Fradkin. Critical behavior of disordered degenerate semiconductors. I. Models, symmetries, and formalism. *Phys. Rev. B*, 33:3257, 1986.

[51] E. Fradkin. Critical behavior of disordered degenerate semiconductors. II. Spectrum and transport properties in mean-field theory. *Phys. Rev. B*, 33:3263, 1986.

[52] Y. Ominato and M. Koshino. Quantum transport in a three-dimensional Weyl electron system. *Phys. Rev. B*, 89:054202, 2014.

[53] S. V. Syzranov, L. Radzihovsky, and V. Gurarie. Critical Transport in Weakly Disordered Semiconductors and Semimetals. *Phys. Rev. Lett.*, 114:166601, 2015.

[54] K. Kobayashi, T. Ohtsuki, K.-I. Imura, and I. Herbut. Density of States Scaling at the Semimetal to Metal Transition in Three Dimensional Topological Insulators. *Phys. Rev. Lett.*, 112:016402, 2014.

[55] J. Ruan, S. Jian, H. Yao, H. Zhang, S.-C. Zhang, and D. Xing. Symmetry-protected ideal Weyl semimetal in HgTe-class materials. *arXiv*, 1511.08284, 2015.

[56] J. Cardy. *Scaling and Renormalization in Statistical Physics.* Cambridge University Press, Cambridge, 1996.

[57] A. Altland and D. Bagrets. Theory of the strongly disordered Weyl semimetal. *Phys. Rev. B*, 93:075113, 2016.

[58] S. Murakami. Phase transition between the quantum spin Hall and insulator phases in 3D: emergence of a topological gapless phase. *New J. Phys.*, 9:356, 2007.

[59] J. Xiong, S. Kushwaha, T. Liang, J. Krizan, W. Wang, R. Cava, and N. Ong. Signature of the chiral anomaly in a Dirac semimetal. *arXiv*, 1503.08179, 2015.

[60] P. Moll, N. Nair, T. Helm, A. Potter, I. Kimchi, A. Vishwanath, and J. Analytis. Chirality transfer dynamics in quantum orbits in the Dirac semi-metal Cd3As2. *arXiv*, 1505.02817, 2015.

[61] P. Moll, A. Potter, B. Ramshaw, K. Modic, S. Riggs, B. Zeng, N. Ghimire, E. Bauer, R. Kealhofer, N. Nair, F. Ronning, and J. Analytis. Magnetic torque anomaly in the quantum limit of the Weyl semi-metal NbAs. *arXiv*, 1507.06981, 2015.

[62] X. Huang, L. Zhao, Y. Long, P. Wang, D. Chen, Z. Yang, H. Liang, M. Xue, H. Weng, Z. Fang, X. Dai, and G. Chen. Observation of the chiral anomaly induced negative magneto-resistance in 3D Weyl semi-metal TaAs. *Phys. Rev. X*, 5:031023, 2015.

Curriculum Vitae

Der Lebenslauf ist in der Online-Version aus Gründen des Datenschutzes nicht enthalten.